UNIVERSITÀ DEGLI STUDI DI PADOVA
DIPARTIMENTO DI INGEGNERIA CIVILE, EDILE E AMBIENTALE
Department Of Civil, Environmental and Architectural Engineering

Corso di Laurea Magistrale in Environmental Engineering,
Land Planning and Management

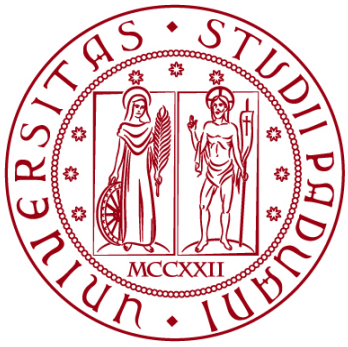

TESI DI LAUREA

ANALYSIS OF GNSS AND INSAR DATA FOR THE MONITORING OF ROVEGLIANA LANDSLIDE (RECOARO TERME, VICENZA)

Relatore:

Chiar.mo PROF. MASSIMO FABRIS

Laureando:

ANITA PIZZAIA

ANNO ACCADEMICO 2021-2022

09-2022

Index

ABSTRACT

The aim of this paper is to analyze, using the open source Qgis, GNSS and SAR data in order to assess the deformations of the Rovegliana landslide (VI). The other purpose is to check whether the two datasets are congruent with each other or not, and whether they can be used together.
In the first part of my thesis, I described all the techniques used, namely SAR, GNSS, TLS and Structure from Motion. I then summarized three previous case studies in order to give the reader a better understanding of the area of interest and its problems.
In the analysis phase I loaded the orthophoto of the Veneto Region into Qgis, inserting the boundary of the landslide area and the coordinates of the GNSS points of 2018, which are the reference for the displacement vectors that I created, first with data from 2021 and then 2022. Six campaigns were in fact carried out, in particular in October 2018, June 2019, October 2019, October 2020, June 2021 and June 2022.
Then I georeferenced an image in order to create polygons representing the various landslide areas. Subsequently I entered the vertical and horizontal SAR data, taken from 2014 to 2019, and calculated the average of these velocities within the various landslide areas and in the circular areas surrounding the GNSS points.
Finally, I analyzed and discussed the results obtained.

1 INTRODUCTION

Italy is one of the most vulnerable European countries from the hydrogeological point of view, due to its lithological and structural characteristics. Landslide phenomena, in fact, are widespread throughout the national territory. The IFFI report (Inventory of Landslide Phenomena in Italy) published in 2017 has surveyed about 620.808 landslides that are equivalent to 7,9% of the national territory [15]. 70.5% of Italian municipalities are affected by landslides and 2% of the population is at risk of them. The total cost of damages due to hydrogeological risk from 1944 to 2012 is 61.5 billion euros.

The study area involved in the landslide monitoring is Rovegliana, a hamlet of the municipality of Recoaro Terme in the province of Vicenza (VI), located on a slope in the north-eastern Italian Pre-Alps (fig.1).

This municipality is located in the initial part of the valley of the Agno River, a typically mountainous area with altitudes ranging from a minimum of 300 to a maximum of 2000 meters above sea level.

The area under investigation is 4.2 km^2 wide, elevation ranges from 800-900 m on top to 400-330 m a.s.l. at the bottom of the slope, in correspondence of the Agno torrent, and slope gradient varies from 40° in the upper part to 20° in the lower, depending on the geological setting. The mean annual temperature and rainfall measured in the period 1994-2019 are 10.7 °C and 230 cm, respectively. There are two main wet seasons, from March to June (Spring) and from September to November (Autumn), but short-duration intense rainfall events can occur in summer (July and August).

This area is not very urbanized, with several small agglomerates of houses and a minor road network present.

The area has been affected for a long period of time by landslides of various types that lead to breakage and deformation of buildings and infrastructure, generally triggered by exceptionally intense rainfall events.

Landslides that cause the collapse of buildings have been monitored using different survey methodologies for several years such as aerial photogrammetry and GNSS (Global Navigation Satellite System) technology.

The locality of Rovegliana is made up of a group of districts which, due to strong latent instabilities that have occurred over the years, are still subject to laser scanner and GNSS surveys, located in the districts with the highest degree of criticality. More specifically, they are: Contrada (district) Fracassi, Contrada Camonda, Contrada Piazza, Contrada Cappellazzi, Contrada Vascellari, Contrada Sigismondi.

Figure 2 shows the orthophoto of the Rovegliana area and a continuous red polygon representing the landslide perimeter. The landslide perimeter was traced thanks to the 3D vision within the Laboratory of Surveying and Geomatics of the University of Padua by tracing the ridges of the mountainous-hilly area passing through the axis of the Agno stream, starting from an aerial photogrammetric survey performed in 2005.

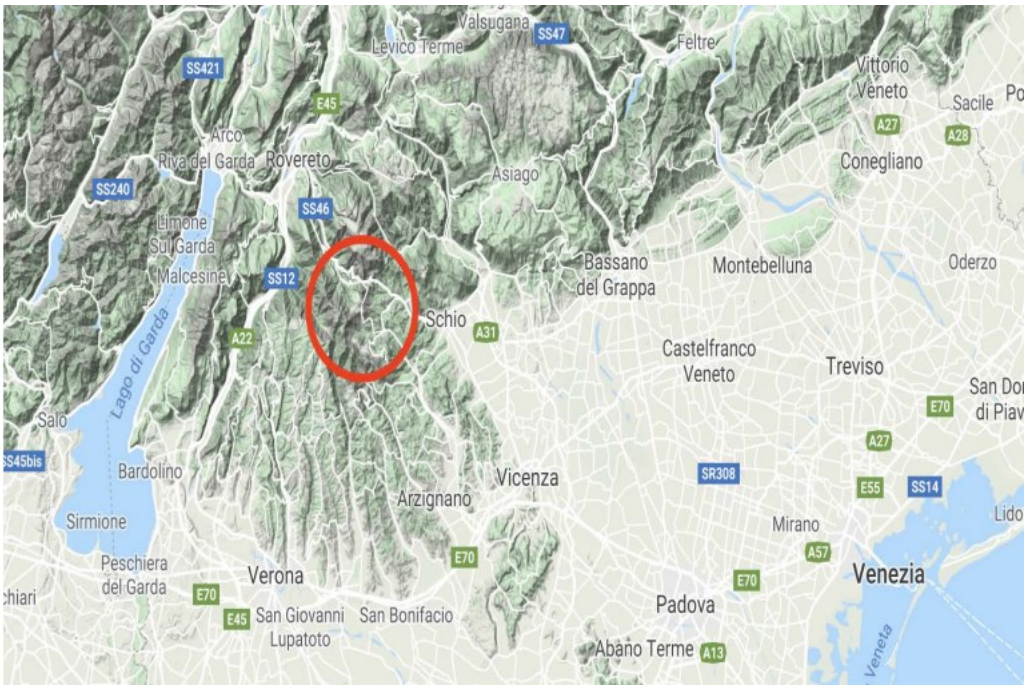

Figure 1: General cartography of the area of interest [2]

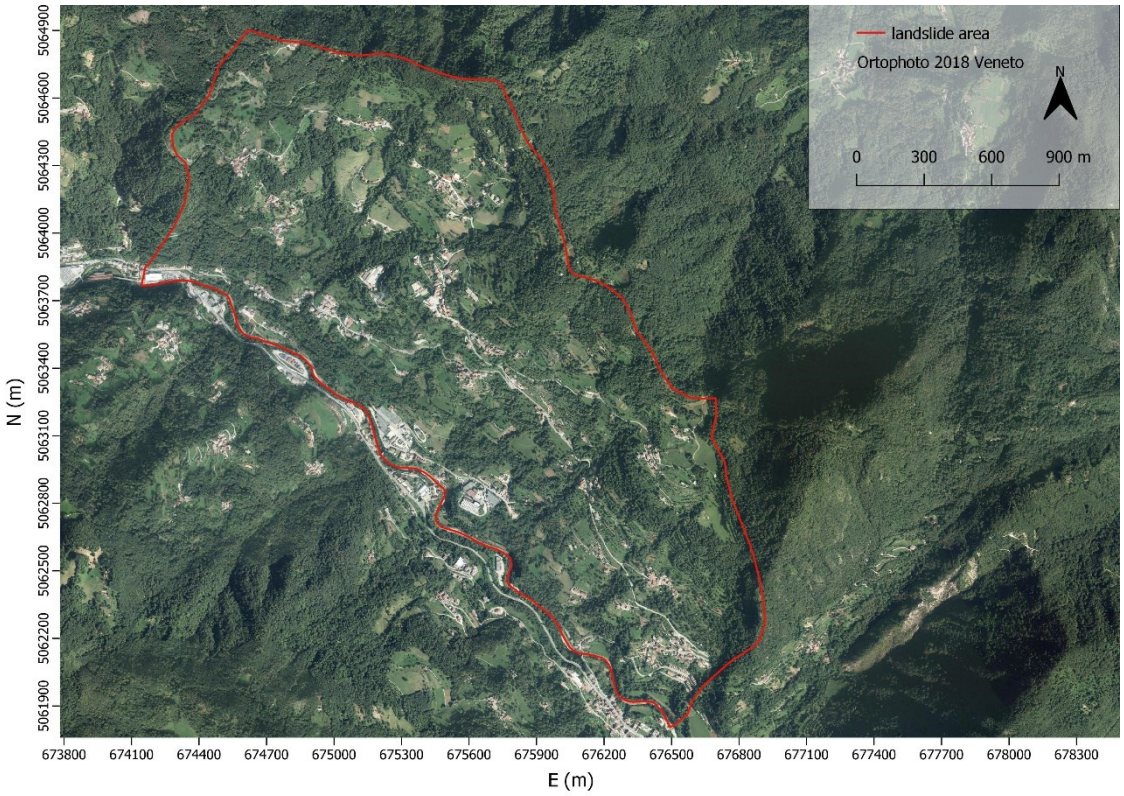

Figure 2: Study area and perimeter of landslide [source: author]

In the Recoaro area, the subalpine crystalline basement (formed in the Palaeozoic) is covered by a sequence of sedimentary formations (period from the Permian to the Miocene), at variance with the basement below. These discordances are the result of the particular position of the area during the Triassic period, which is very different from the present day. In fact, Recoaro was located in tropical and shallow sea conditions, therefore very subject to eustatic variations, which have been recorded in the stratigraphy in the form of erosive discordances. A brief description of the rock formations present in the study area is given below.

The rocky substrate is composed of the pre-Permian phyllites of the Sudalpine crystalline basement and the Permian-Triassic sedimentary succession. The latter is composed of an alternation of mainly terrigenous (Val Gardena sandstones), strongly calcareous and dolomitic formations (Recoaro Limestone, Serla Inferiore Dolomite and Monte Spitz Limestone) and formations with intermediate characteristics. These include both powerful limestone, limestone-marly and dolomitic banks and also thick siltstone, pelitic, marly and arenaceous levels (Bellerophon Formation, Werfen Formation, Gracilis Formation). Intercalated with the sedimentary succession, we find various levels of volcanites, which in this area are mainly latites, latiandesites and rhyodacites. The geological units mostly present a landslide layering which, together with the fracturing of the rock masses and the presence of clay levels, represents the main predisposition factor for the landslides in the area.

The detrital aquifer deposit is represented by clastic material with angular elements of a predominantly carbonate nature and with a sparse silty-sandy matrix. It is found mainly at the base of the limestone walls located at the highest altitudes in the area under examination. The eluvial deposit consists of heterometric clasts, from angular to sub-angular, with an abundant clayey-silt matrix. The colluvial deposit consists mainly of a silty-clayey matrix with rare heterometric clasts of a carbonate and silty-arenaceous nature; it is found in the sub-floor areas and at the base of the slopes. There are also paleo-landslide deposits represented by heterometric carbonate and silty-siltstone clasts in a silty-clay matrix (in Contrada Cappellazzi). The alluvial deposit at the bottom of the valley is mainly made up of gravel and sand with pebbles and sometimes large boulders.

Landslides are phenomena of various types and sizes related to the debris deposition of geological bodies according to the lithostatic nature of the substrate. A situation of unstable equilibrium of the surface soil or subsoil may involve particularly extensive removals of portions of soil. In some cases, these movements may concern both lithostatic layers, i.e., the subsoil and the surface soil. Several types of landslide movements can be characterised according to the type of material involved, the speed of descent of the solid material and the duration of the landslide movement.

Depending on the duration of the landslide movement and on the lithological type of soil, two of the main phenomena of landslide movement can be differentiated: Soil Creep and Soil Flow.

Soil creep is the very slow movement of soil particles, generally imperceptible and not subject to any acceleration. The velocity can be found in few millimeters units per year and can affect slopes with very gentle acclivities. The movement is laminar in nature, as if the ground were divided into layers of infinite thickness and adjacent to each other, animated by different speeds that decrease exponentially in depth. The Soil Creep phenomenon does not generally affect slope layers deeper than 3 to 4 m.

Soil flow, on the other hand, refers to the landslide movement involving incoherent or inconsistent materials due to the high degree of water saturation within the pores of the solid matrix. The flow cannot be assimilated as laminar because more or less intense mixing is generated between the different layers involved. This process is triggered by the sliding of a surface due to a variety of situations, which may be, for example, melting of the snow or interstitial ice in the ground. The characteristic velocities are higher than the soil creep phenomenon and can range from several centimeters per day to a few tens of centimeters per year. The instability of a slope is often due to the interaction of several natural and artificial causes. Natural external forces such as intense precipitation of short duration and high rainfall over a long period of time are the main factors in triggering instability phenomena. In addition, soil type, lithology, slope steepness, temperature ranges and hydrogeology play a fundamental role in the stability of a slope, as do anthropogenic factors. Landslides can occur in the most varied forms and sizes, some of which are listed below: landslides from collapses, overturning, sliding, landslides and debris flows.

The following landslide types were recognized in the study area:

- *Translational landslides*: these imply an almost planar movement from upstream to downstream and generally develop along structural discontinuities (faults, joints, etc.), lithostratigraphic discontinuities or at the rocky substratum-cement cover interface. In the area, these movements are favored by the poor resistance characteristics and the position of the various layers with respect to the slope. The action of water plays a fundamental role, capable of destabilizing even slopes of modest inclination;
- *Rotational landslides*: these are landslides in which the sliding surface, especially in cohesive soils, is approximately a circular arc (seen transversely) but, if the phenomenon involves several layers, this surface takes on even more complex forms (when combined with a translational landslide, we have a roto-translational landslide). The material involved belongs both to the Gracilis Formation and to the slope deposit;
- *Creep movements*: these are slow surface deformations that occur even with modest slopes at a rate of few millimeters per year. Not directly observable, creep produces evident effects only years after its beginning, recognizable through fences and poles inclined towards the valley, bent tree trunks, tension fractures on walls etc... The effect of creep is maximum on the surface and decreases exponentially in depth;
- *Diffuse surface movements*: these are identified in areas where it is clear that there has been movement, evidenced by numerous escarpments, changes in slope, accumulations, but where it is not possible to accurately delimit the individual instability phenomena.

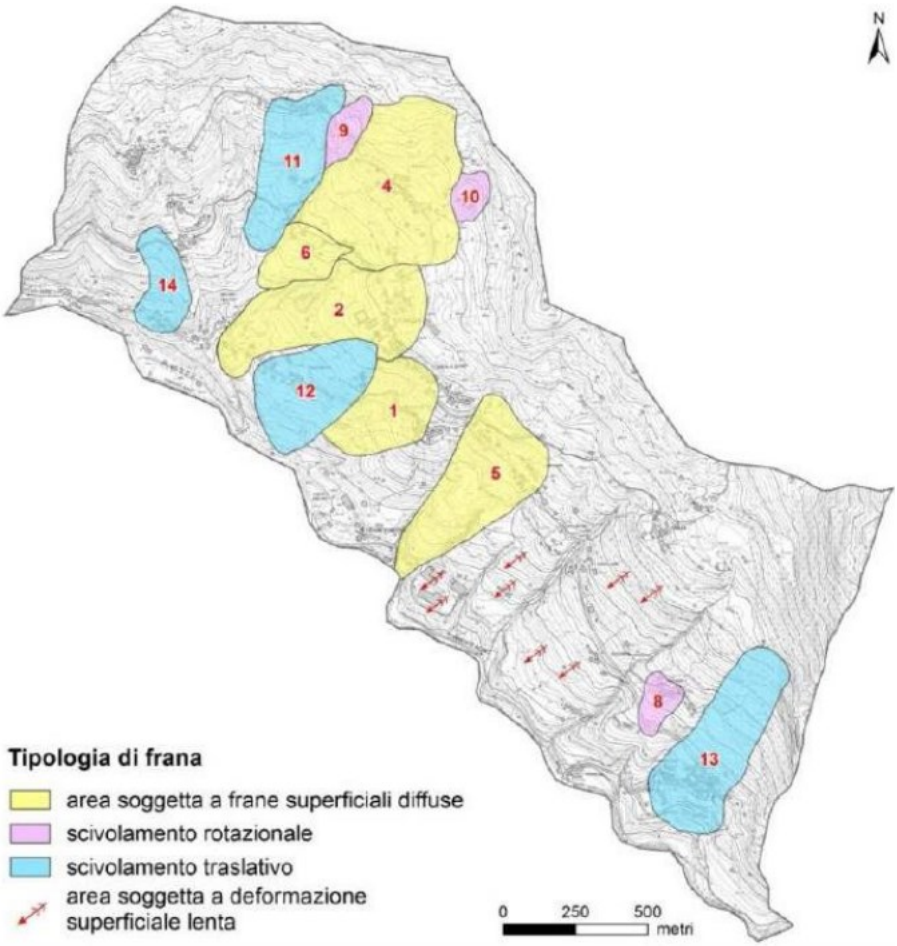

Figure 3: Delimitation of landslide phenomena identified in the Rovegliana area and their classification based on the type of movement, according to the results of PS and SBAS analysis of ERS and ENVISAT data [1]

1.1 LANDSLIDE CAUSES

The factors involved in the process of soil instability are many, often caused by inadequate anthropic actions, but the local lithology is certainly a predisposing element. In the study area there is a detrital cover consisting of material of various sizes contained in a sandy-clay matrix; this factor is fundamental in periods of high rainfall, making this surface cover subject to sliding downwards. The presence of numerous erosion furrows that attract material, especially during periods of flooding, creates situations of instability throughout the slope. The anthropic factor may have had a non-secondary role in destabilizing the area as was evident in the Cappellazzi district. Numerous geological investigations have been carried out in this area in recent years in order to monitor and contain the current situation; there have been numerous reports from residents to the Province of Vicenza due to movements after periods of heavy rainfall. One of the causes was the construction of the village of Rivelunghe, a complex of terraced houses built in the 1990s downstream from the Contrada Cappellazzi. As a result, and as verified by the testimony of residents, the landslides intensified considerably and even subsequent works (such as the widening of the road leading to the district) required careful investigation in order to keep the situation within limits. Another cause is the large amount of surface and sub-surface water present, due to the

high rainfall in the area. A high level of soil imbibition can trigger landslide phenomena where portions of slopes, due to the weight of excess water within the solid soil matrix, slide downhill. This occurs especially when the slopes involved are particularly steep. Another reason is the poor regulation of superficial meteoric water, which is poorly maintained and, in some cases, undersized, compared to the entity of the precipitation events that affect the area considered, causing major hydrogeological instability. In fact, the poor maintenance and carelessness of the collection, derivation and storage structures can induce uncontrolled surface and subsurface flows, water dispersion in the subsoil, resulting in the overloading of deposits. Often the instability of a slope is due to the interaction of several concomitant causes.

The situation throughout the study area is still alarming and monitoring studies and targeted interventions are still underway to stabilize an area that the inhabitants themselves consider dangerous; the numerous cracks in walls and roads that periodically increase are clear evidence of this instability.

2 METHODOLOGIES APPLIED

2.1 SAR

SAR (Synthetic Aperture Radar) interferometry consists of analyzing the phase difference between two SAR images, obtained by recording backscattered signals from corresponding areas, thus relating to the same scene, although observed from different viewpoints. RADAR sensors acting as transmitters and receivers consist of antennas installed on satellites that rotate around the earth with a specific revisit time. The two main uses of SAR interferometry relate to the study of the displacement of a target or an extended area, or to the definition of topographic maps and digital terrain elevation models (DEM). Deviation between satellite positions during two separate acquisitions results in phase mismatch of the backscattered signals, as illustrated in Figure 4.
The movements measured by the satellites are the projection of the point's displacements along the sensor-target junction, with the satellites acquiring data along a direction inclined at an angle θ (about 23° from the vertical), called the line of sight (Fig. 5).

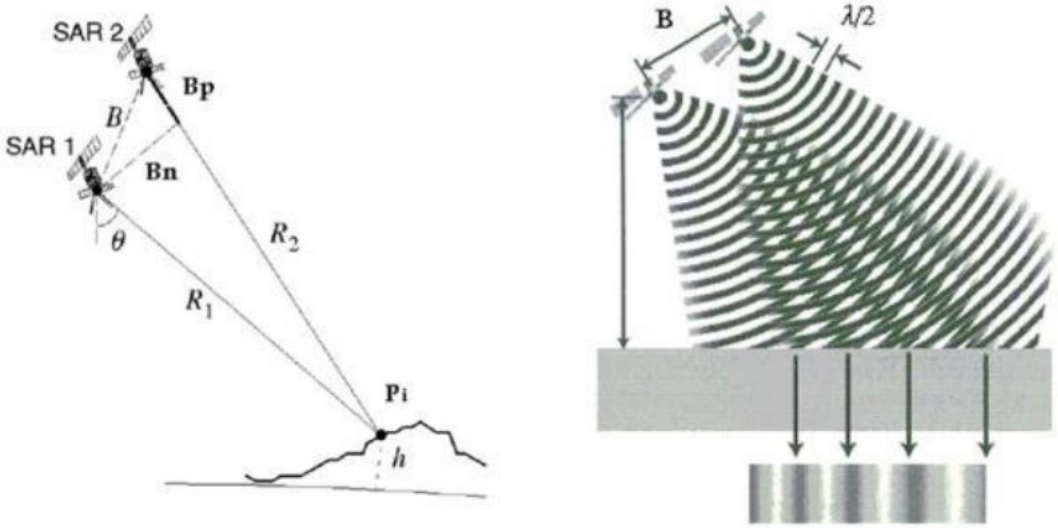

Figure 4: Left: Schematization of two different acquisitions of satellite RADAR data, of the normal baseline (Bn) i.e. the distance between the two acquisition positions. Right: effect of the phase difference between the two acquisitions due to the different satellite [1]

The phase difference between two acquisitions of the same area may be due not only to differences in acquisition geometry, but also to changes in the ground target hit by the electromagnetic wave. Surface subsidence or otherwise changes in surface morphology cause a phase difference, which is detected in the generation of an interferogram.

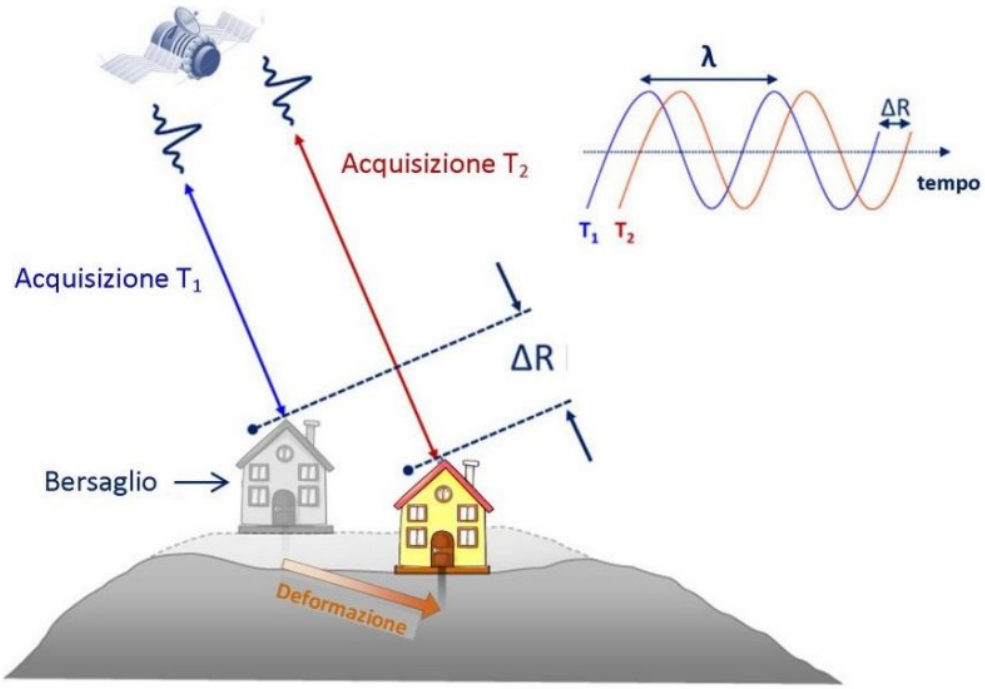

Figure 5: Simplified diagram of the phase difference between two acquisitions due to deformation of the target surface [1]

Previous works have used data acquired by the ERS-1 and ERS-2 (Earth Resources Satellite), ENVISAT (ENVIronmental SATellite) satellites, COSMO-SkyMed constellation and Sentinel-1A/1B.

ERS-1 acquired data from July 1991 to March 2000, while ERS-2 has been operational since the summer of 1995. The ERS satellites follow heliosynchronous orbits that are slightly inclined to the meridians, illuminating, from an altitude of about 780 km, a strip of land about 100 km wide with a SAR radar system that can identify even millimetric movements. The same nominal orbit is retraced every 35 days (revisiting time), thus allowing data from the same ground scene to be acquired at different times. The ENVISAT satellite, launched in November 2002, replaced and extended the functions of the ERS-1 and ERS-2 satellites. It is equipped with an ASAR (Advanced Synthetic Aperture Radar) sensor, which represents an evolution of SAR with an improvement in the size of the observed scene in a single image. The satellite has a revisit time equal to that of ERS (35 days), but with a delay of 30 minutes.

The COSMO-SkyMed satellite constellation consists of four units equipped with microwave Synthetic Aperture Radar operating in the X-band (3.1 cm wavelength). The first of the constellation's four satellites was launched in June 2007 and the last in 2010. Its heliosynchronous orbit is about 620 km above the Earth's surface. The revisit time varies from 16 days for the single satellite to 4 days for the complete constellation.

The Sentinel-1 mission comprises a constellation of two polar-orbiting satellites, 1A and 1B, operating day and night performing C-band synthetic aperture radar imaging, enabling them to acquire imagery regardless of the weather. In this paper, the SAR acquired data from 2014 to 2019. The observation of the earth's surface is achieved by combining the orbital movement of the satellite along the meridians (quasi-polar orbit) with the rotation of the earth in the equatorial plane.

Satellites acquire data along ascending orbits, transition from South to North, and along descending orbits, transition from N to S. The use of these two modes is necessary because the displacements can be both vertical and horizontal; the measurement is therefore a combination of the two phenomena and, using a single measurement, it is not possible to distinguish the two contributions.
The output of both ascending and descending datasets measured the projected component of actual deformation in the direction of the line of sight (LoS). To characterize the long-term behavior of the buildings and landslides, LoS velocity should be analyzed according to the actual ground surface motion. The availability of two different viewing geometries (ascending and descending) allowed to get the horizontal (east–west) and vertical components of the actual motion from the LoS velocity.
After having chosen the most suitable image dataset for the area of interest, we move on to the identification of the master, i.e. the temporal and geometric reference for all the other images (called slaves).
The interferometric analyses carried out saw the application of the two main techniques of differential interferometry[1], (DInSAR): The Persistent Scatterers (PS) technique and the Small BAseline Subset (SBAS) technique.
PS and SBAS, mainly aim at eliminating atmospheric phase contributions, which are spatially correlated within a single SAR scene and temporally uncorrelated. However, above all, these techniques estimate surface motion considering the usually strong temporal correlation of deformation phenomena. The PS technique generates differential interferograms referred to one common master identifying persistent point-wise reflectors, such as manmade structures and rocks. In general, PS SAR performs better in urban and nearby areas, where the number of persistent scatters is higher than in natural terrain. The SBAS technique relies on an appropriate combination of image pairs with small spatial and temporal baseline (meaning orbits close together and small revisiting time), overcoming some of the limitations of atmospheric effects and detecting the temporal evolution of the surface deformations.
The products obtained with this method are, therefore, characterised by a high spatial density of monitorable points, with a precision that can reach 1 mm/y. This approach is more effective in the case of spatially correlated deformations. Moreover, it increases the spatial coverage, especially in non-urban areas.

2.2 GPS

Global Positioning System is a real time 3-D positioning system that use satellites to determine the ground position of an object with a maximum precision in the order of 1 cm. It was developed by the Department of Defense of the United States.
The system can be separated into three segments: the Space, the Control and the Users.
The space segment is made up of a variable number of satellites ranging from a minimum of 24 to a maximum of 32. They are approximately 20,200 km far from the Earth's surface and are placed on six orbital planes spaced 60° apart in longitude and inclined 55° to the equatorial plane. This satellite configuration makes it possible to

[1] Differential interferometry is made possible by the availability of several compatible images of the same area, generating a true historical data set. Such images, acquired from slightly different satellite positions, or small orbital variations and at different time instants, have greatly extended the possibilities of using InSAR data compared to simply using a pair of images.

observe, at anytime, anywhere on the globe, simultaneously, between four and ten satellites with an elevation of at least 15° above the horizon.
The period of rotation is 11 hours and 58 minutes.
Each Satellite transmits navigation signals in phase modulation on two carrier waves named L1 and L2, both multiples of the fundamental frequency f0 (f0 = 10.23 MHz) of the atomic oscillators.
In addition to the GPS signal, these satellites also transmit a low-frequency signal containing information about their position (ephemeris) and various parameters relating to the quality of the signal sent.
The control segment is composed by five main Stations on physical Earth's surface, placed along the equatorial plane: Hawaii, Colorado Springs, Ascension, Diego Garcia, Kwajalein.
The stations are needed to monitor the ephemerides (Satellite coordinates along their orbits) and predict the next orbit (for a limited time).
Colorado Springs is the Master Station: collects the data from the other stations and, processing these data, estimates the ephemerides of the Satellites as well as other parameters of the Space segment. The other Stations transmit the data processed by the Master's one to the Satellites (ephemerides update, correction of orbital parameters, information on the effects of the atmosphere on the waves propagation, etc.)

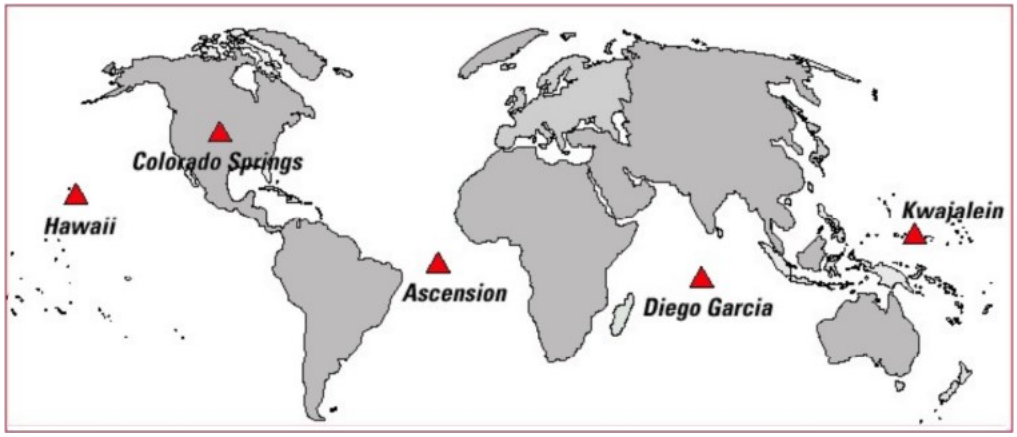

Figure 6: The control segment with the 6 different stations [7]

The ephemerides determination procedure consists of several steps. The first one consists in analyzing the data collected by the control stations during the last week in order to have a first estimate of the trajectories that the satellites will follow the following week. These trajectories are referred to as 'reference ephemerides' with an accuracy in the order of 50 m, and these are then compared with data collected over the last 12 to 24 hours. In this way, the reference ephemerides are recalculated and adapted to a more recent configuration, leading to the determination of the predicted ephemerides. The predicted ephemerides are then sent to the satellites which, in turn, will send them to the users via the low frequency signal. A user with a GPS receiver receives simultaneously at all times the signals on the two L1 and L2 carrier waves and the ephemerides of each "visible" satellite. This information is sufficient to make a fairly precise positioning in real time. The errors associated with the determination of the predicted ephemerides are as follows:
- Approximately 1 m for the radial component (satellite - receiver direction)
- Approximately 7 m for the tangential component
- Approximately 3 m for the normal component

Higher accuracies are obtained with the processing of the GPS data on the basis of the real trajectory followed by the Satellites. These data are available with a delay of 10-15 days from the time of acquisition of the GPS signals, so in this case the positioning will be postponed. (Precise ephemerides can be downloaded from several sites, e.g. NASA).
The user segment is composed by Users equipped with GPS Receiver to obtain the three-dimensional positioning in real time (Predicted ephemerides) or postponed (Precise ephemerides).
A GPS Receiver is composed by an Antenna, a controller with microprocessor, a data recording system and a power system (Battery). Measurements are carried out in phase center of Antenna: its detection is known in a more or less precise way, depending on the instrument model used.

THE GPS REFERNCE SYSTEM
Is named WGS84 (World Geodetic System 1984): the origin of the coordinates is coincident with the Earth's center mass and the cartesian system is fixed to the Earth.
The Z axis is chosen in the direction of the Conventional Terrestrial North Pole (CTP); the X axis passes for the intersection between the Meridian reference plane passing for Greenwich with the equatorial plane connected to the CTP; the Y axis complete the orthogonal system and belong to the equatorial plane, 90° East of the X axis.
The GPS measures ellipsoidal elevations with respect to the WGS84 Ellipsoid and not orthometric or geoidic ones (i.e. referred to the Geoid). Unfortunately, the ellipsoidal elevations provided by a GPS survey are not of particular interest for many environmental and civil engineering applications.
Ellipsoidal and orthometric elevations are connected by the relation: $h = H + N$
h: ellipsoidal elevation provided by the GPS;
H: geoidic or orthometric elevation measured with the leveling;
N: Geoid ondulation.

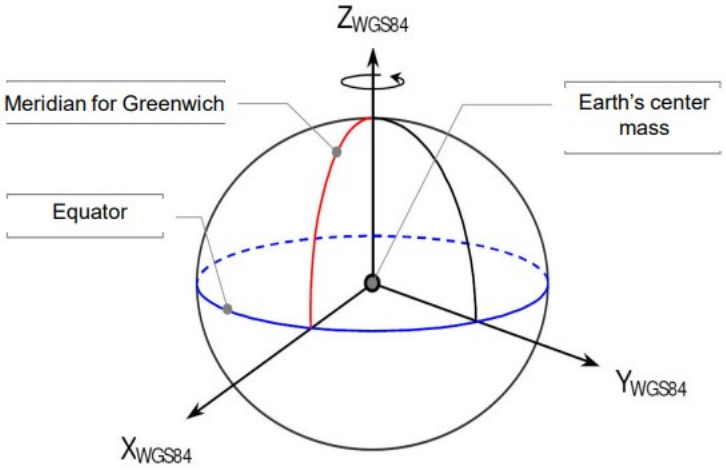

Figure 7: WGS84 [7]

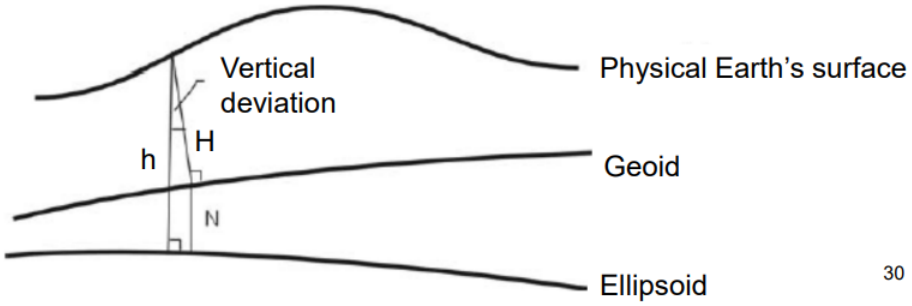

Figure 8: Ellipsoidal and geoidic elevation [7]

THE GPS SIGNAL

Each Satellite transmits a signal composed by several components generated from the same frequency $f_0 = 10.23$ MHz typical of the on-board oscillator.

The signal components are:

- carriers L1 and L2: are the two waves with frequency of 154 and 120 times f_0 respectively, and wavelengths resulting of 19.05 cm and 24.45 cm;
- codes C/A, P and W (square waves): are pseudorandom codes, i.e. sequence of +1 and -1, that are repeated after a time interval. In the C/A code (Coarse/Acquisition or Clear/Access) the sequence is emitted at a frequency equal to $0.1f_0$ and is repeated every millisecond. For each Satellite a C/A code is assigned for the identification. The P code (Precision or Protected) is repeated every week and is a more accurate signal.
  The W code is known only to authorized users that emit at a frequency equal to $0.2f_0$, used to encrypt the P code;
  The C/A code is modulated only on L1, while the P code is modulated both on L1 and L2 carriers. The instruments that receive the P code are characterized by high precisions;
- message D: with this message the User is informed about the operating status of the Satellite, about the clock, and, especially, about the orbit through its ephemerides.

Codes are modulated on the phase signal: in correspondence of the transition between opposite status of the pseudorandom binary code (from +1 to -1 and viceversa) the carrier wave has phase shift of 180°.

The generated code from the Satellite, and sent to the Receiver on the ground, arrives with a delay due to the distance travelled. Inside to the Receiver the same code is generated: the phase difference between these two codes (Satellite and Receiver) depends by the Satellite-Receiver distance, and by the clock's synchronization errors involved (offset error of the clocks).

The delay (in time) between the arrived signal and the replication generated by the Receiver is obtained from subsequent comparisons between these signals until the correlation is maximum.

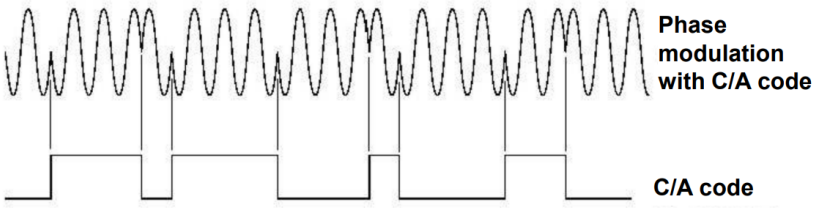

Figure 9: phase modulation of the code [7]

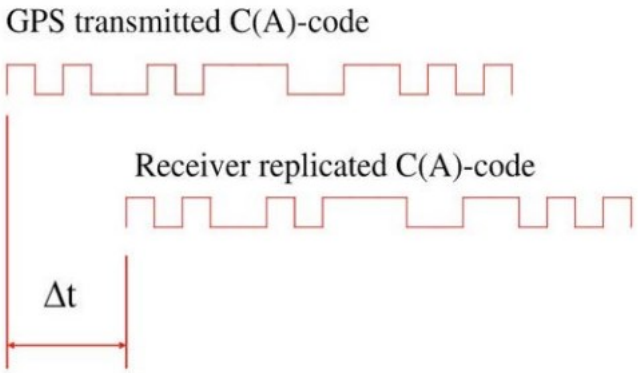

Figure 10: Delay of signal [2]

In this way, it is possible to know the time needed to the signal for the Satellite-Receiver path. This time is function of the Satellite-Receiver distance (range) if both Satellite and Receiver clocks errors are not present.

EQUATION OF THE GPS PSEUDO-RANGE

GPS positioning is based on the estimation of Satellite-Receiver distance.

The positioning can be obtained with methods which depend by the type of survey and data processing:

- Absolute positioning: in this case, only a Receiver is used and absolute position in the global reference system of the GPS is computed;
- Differential positioning: similar to the absolute positioning, but the errors Satellite-Receiver distances are corrected using information provided from a second Station located on a known point;
- Relative positioning: using two Receivers simultaneously allow the processing of the vector (baseline) connecting the two points. Allows the maximum accuracy due to the eliminations of many errors of the system;

Absolute positioning

It is the simplest method and does not require expensive instruments. Is used for navigation because it gives us the coordinates in real time with precision ranging from 1 m to 10 m, depending by the used code (C/A or P) and the type of Receiver.

If the Receiver can acquire only the C/A code, the accuracy of the horizontal positioning is in the order of 10 m, while is worse in the elevation; using the P code the accuracy of horizontal positioning is in the order of few meters (2-3 m).

Assuming a perfect synchronization between the emitted code by the Satellite and the reproduced code by the Receiver, the signal send from the Satellite at t_0 time, comes to the Receiver at t_1 time, with a delay due to the time needed to perform the Satellite-Receiver distance. On the other hand, assuming the non-perfect synchronization between the Satellite and Receiver codes (the real case) an offset will be present, affecting the Satellite-Receiver distance (introducing an error).
For this reason, the Satellite-Receiver distance is named "pseudorange":

$$\rho_i{}^j = c \cdot \Delta t = \sqrt{(Xj - Xi)^2 + (Yj - Yi)^2 + (Zj - Zi)^2} \pm c \cdot \delta ti\ j$$

c: light speed in the space;
Δt: time of flight of GPS signal;
Xj, Yj, Zj: Satellite ephemerides;
Xi, Yi, Zi: coordinates of the point on the Earth's surface;
δti^j: error of non-synchronization clocks;

The coordinates of the point on the Earth's surface are the unknowns of the problem.
The Satellite coordinates are known (Precise or Predicted ephemerides)
The error of non-synchronization clocks (δti^j) is a further unknown.
Thus, to solve the problem we need a system of at least 4 equations in the 4 unknowns. Each observed Satellite provides a new equation, then, we need the observation of at least 4 Satellites.

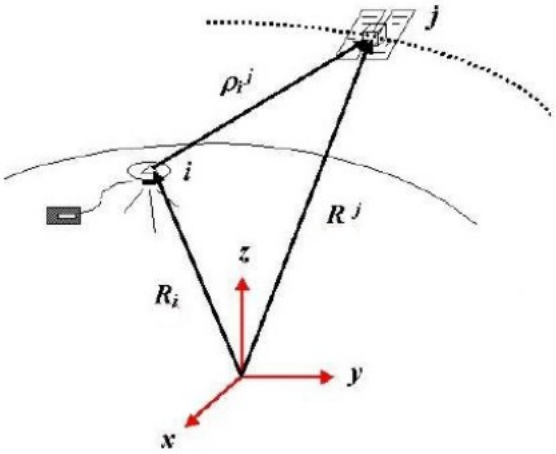

Figure 11: GPS configuration [7]

Differential GPS (or DGPS) is a method that uses the Absolute positioning and allows to improve the positioning using two receivers in the Earth in order to reduce drastically the errors. A precision of few cm can be obtained.
It allows to measure the position of the antenna phase center of a Receiver located on an unknown point compared to a second Receiver placed on a point with known coordinates.
With this technique the corrections to the pseudorange and their changes over time are computed compared with a reference Station (Master) of known coordinates; subsequently, these corrections are sent to the second Receiver (Rover) for the correction of the errors, that are similar between the Stations (because, normally, the distance between Master and Rover Receivers, in the order maximum of 10 km, is very small compared with the Satellite-Receiver distance). In the real time applications, the

communication of these corrections requires a radio-modem connection or telephonic connection (SMS).
Applications are in the field of Cartography (update), terrain surveys, road surveys, buildings surveys, etc…

Relative positioning
Also in this case, two Receivers are used: a Receiver is placed on a known point while the other is placed on the unknown point (the goal of the survey is the measurement of the coordinates of unknown point).
The element at the basis of the coordinates computation is the "baseline" vector that connect the two points: this vector is oriented in the Cartesian reference system adopted for the Satellite positioning, and the distance between the two points has to be less than 20 km. If a generic point P is defined in a Cartesian reference system and is known, the union vector with a second point Q, oriented in the same reference system, allow to compute the Cartesian coordinates of point Q.
It can be carried out either with a static method (the receivers are kept in position for a measurement session lasting from a few minutes to a few hours depending on the length of the baseline) or kinematic method (one receiver remains fixed, the other or the others move, successively occupying the points to be measured or following a continuous path).
Processing is carried out in post-processing (i.e. not in real time) from the raw data acquired by the receivers. The static mode can achieve a relative positioning accuracy of the order of 1 cm (or less) and is used to determine networks of baselines for framing or deformation control purposes. The kinematic mode is mainly used for the reconstruction of tracks and vehicle kinematics.
The accuracy of positioning will be influenced by several errors that always affect the Absolute positioning, but are drastically reduced in the Relative and the Differential positioning.
The main types of errors are:

- *errors due to the Satellites orbit*: for the positioning in real time the predicted ephemerides are used, with a precision in the order of 10-20 m;
- *errors of non-synchronization clocks*: this is because the clock in the satellite is a hydrogen clock, with a precision of 10^{-14} seconds, while in the receiver is used a quartz clock that has a precision of 10^{-6} s;
- *errors due to the signal propagation*: it is assumed that the signal propagates in the void, but it actually propagates in the atmosphere, where it is slowed down, especially in the troposphere. We can reduce this error, but not remove it;
- *errors due to multiple reflections (multipath)*: in addition to the signal coming directly from the Satellite, other signals could arrive to the GPS Antenna of the Receiver after the reflection on reflective surfaces, like rocky walls, lakes, buildings ecc…these signals, introducing noise in the data, complicate the reception and the analysis procedures of the correct signal by the Receiver;
- *cycle slip*: is a temporary interruption of the Satellite visibility and this effect creates big problems, especially in the kinematic surveys;
- *errors due to receiving Station*: derive from the Receiver electronics, the instability of the oscillator which generate the standard frequency and then the signal replications, the instability of the Antenna phase center;

- *errors due to the operator*: are errors during the stationing/positioning like the measurement of the height of the antenna.

GNSS
Global Navigation Satellite System (GNSS) refers to a constellation of satellites providing signals from space that transmit positioning and timing data to GNSS receivers. The receivers then use this data to determine location.
By definition, GNSS provides global coverage. Examples of it include:

- Europe's GALILEO, consisting of 26 satellites, designed to eventually contain 30 satellites in orbit;
- The USA's Global Positioning System (GPS), consisting of 30 satellites;
- Russia's Global'naya Navigatsionnaya Sputnikovaya Sistema (GLONASS), consisting of 24 satellites;
- China's BeiDou Navigation Satellite System (BDS), consisting of 28 satellites;
- Others like RNSS for India and QZSS for Japan.

This linking of constellations allows us to always receive a large number of signals, an element of considerable importance because more satellites visible are needed to increase the accuracy of the data to an acceptable level for the topographic field.

2.3 LIDAR AND TLS

Lidar is an acronym for "light detection and ranging." It is sometimes called "laser scanning" or "3D scanning" and is an efficient instrument for surveys at high resolution and precision that allows to acquired and stored many 3-D points uniformly distributed on a generic surface (high sampling rate).
It is a remote sensing method that uses light in the form of a pulsed laser to measure ranges (variable distances) to the Earth. These light pulses, combined with other data, generate precise, three-dimensional information about the shape of the Earth and its surface characteristics.
The instrument can be aerial-transported (airplane, helicopter, UAV – Unmanned Aerial Vehicle) or terrestrial (ALS – Airborne Laser Scanning, TLS – Terrestrial Laser Scanning).
The TLS is used in the building surveys, while for land surveying the ALS is used. The working principles are the same for both.
A lidar instrument principally consists of a laser, a scanner, and a specialized GPS receiver. Airplanes and helicopters are the most commonly used platforms for acquiring lidar data over broad areas.
TLS is a ground-based technique that automatically collects the 3D spatial coordinates of a large number of points of objects, with a spatial resolution that ranges from millimeters to centimeters.
The instruments can be classified into 2 categories, depending on the distance measurement technics:
▪ Time of Flight (TOF): resolve the distance between the instrument and the object for each point, by measuring the round-trip time of an artificial light signal provided by a laser;
▪ Phase Shift: instruments that use the comparison between the modulated emitted signal with the phase of the returning signal in order to resolve the distance.

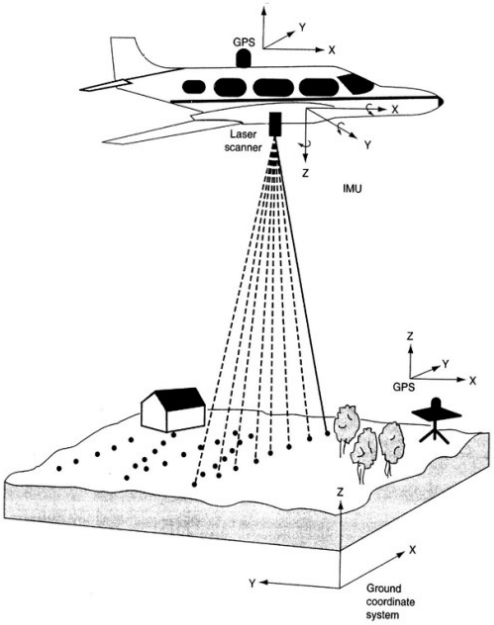

Figure 12: Lidar methodology [7]

The data provided by the instrument, for each point measured, is composed of:
▪ Cartesian coordinates (X, Y, Z) calculated from the measured spherical coordinates (δ, α, β) and referred to a reference system relative to the single scan;
▪ reflectance value (between 0 and 1) i.e., the ratio between the energy of the signal emitted by the scanner and that of the return signal received: it provides information on the type and characteristics of the material;
▪ 3 R-G-B values (between 0 and 255): each point is associated with color information, thanks to the integrated camera (present in the most up-to-date models), coaxial to the laser, which allows the acquisition of images at the same time as scanning, thus providing a mosaic that is used to create a texture in the representation of a photorealistic model.
The tool provides a point cloud, spatially oriented according to its own reference system. If the 3D model is to be referenced to a particular reference system, or if several scans are to be merged into a single model, an alignment (or registration) operation must be performed: this means correctly placing the points of the clouds in a global reference system. To do this, references that act as constraints on the roto translation are indispensable. These references can be found by the software through the superimposition of common portions between two scans with surface matching algorithms, they can be represented by natural points identified manually within the cloud or by special targets positioned ad hoc in the surveyed environment. The first phase of data processing consists of "cleaning" the clouds of spurious data and portions of the scan that do not affect the object to be detected. Targets are identified and scans are aligned until a global 3D model is obtained. It is then possible to geo-reference the 3D model in a local topographic reference system, such as that defined by a survey network measured with traditional methods, or in the national cartographic system through measurements conducted with GPS satellite methodology. In the subsequent phases, triangular mesh surfaces can be created, which continuously represent the

discretized geometries of the point cloud. The operations of comparison between data sets acquired at different times allows the identification of any deformations that have occurred, with the estimation of their entity and the areas involved.

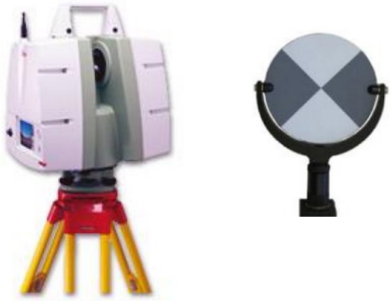

Figure 13: Laser scanner Leica Scan station P20 and Leica HDS target [1]

2.4 STRUCTURE FROM MOTION

Structure from motion (SfM) is a photogrammetric range imaging technique for estimating the 3-D structure of a scene from a set of 2-D images taken at different point of view. SfM is used in many applications, such as 3-D scanning, augmented reality, visual simultaneous localization and mapping.

SfM has been used to generate large point clouds for scene structure reconstructions and geosciences applications. This technique exploits an automatic pixel-by-pixel correlation approach, reconstructing the 3D model in a local or global reference system. The general workflow consists of an initial analysis of the imagery dataset with the feature extraction and matching through an object recognition algorithm (scale invariant feature transform, SIFT). It allows to reconstruct the position of the camera using the coordinates of the measured targets and generate a sparse points cloud, which is composed by the homologue points (tie points) identified in different images. Then, the full-resolution images are used to increase the sparse point cloud, generating the dense cloud through the multi-view stereo (MVS) algorithm. The obtained 3D model can be used for the production of the mesh model, DEM and orthomosaic.

Here are the main steps of SfM:

- Step 1
  Match the corresponding feature and measure distances between them on the camera image plane. The Scale Invariant Feature Transform is the key to matching corresponding features.
- Step 2
  We can calculate individual camera positions (x,y,z), orientations, focal length, and the relative position of the corresponding features in a single step known as “bundle adjustment”. This is because when we have the matching locations of multiple points on two or more photos, there is usually just one mathematical solution for where the photos were taken. In this step, tie points are used.
- Step 3
  A dense point cloud and 3D surface is determined using the known camera parameters and using the SfM points as “ground control”.
  This step is called Multiview stereo matching.
- Step 4

In this step we have the georectification, meaning that we convert the point cloud from an internal, arbitrary coordinate system into a geographical coordinate system. This can be achieved directly (if I know the position of cameras and the focal lengths) or indirectly (by incorporating ground control points with known coordinates).

- Step 5
  Generation of different products, like Digital Surface Model or orthophoto.

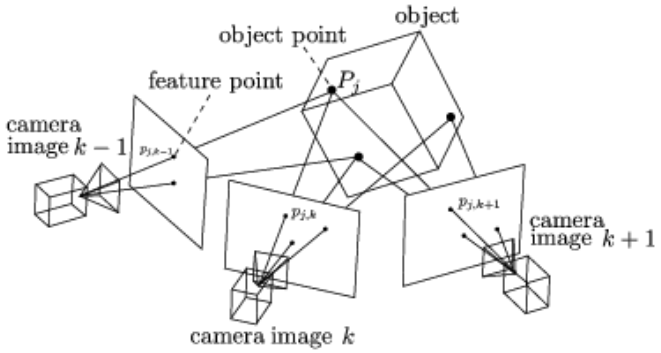

Figure 14: Structure from motion [16]

3 PREVIOUS STUDIES

3.1 Geomatic methodologies for deformations analysis: application to the Rovegliana landslide (Recoaro Terme, Vicenza) [2]

In this thesis the photogrammetric flights of 2005 and 1982 are analysed, since the interpretation of aerial photographs still represents the fastest tool for carrying out systematic geomorphological surveys over vast areas. The most significant advantages derive fundamentally from an overview of the physical territorial elements, such as morphological, structural and geological characteristics that are sometimes difficult to detect in field surveys. However, this survey method has limitations in identifying small and medium-sized landslides in forested or highly built-up areas. On the contrary, the survey carried out through the geolocation and terrestrial navigation system is the most reliable in terms of accuracy as it is not affected by limitations such as large vegetation and high slope gradients. Therefore, GNSS satellite analysis is also carried out in this paper.

Returning to photogrammetry, the problem is that, in this case, the photographic support points (PFA) are not known a priori, i.e., those points with known coordinates that allow the translation of the images to be georeferenced compatible with our reference system. The chosen number of PFA were 21, which were measured with GNSS instrumentation. The high-precision geodetic point measurement campaign for the Rovegliana area took place on the 8th of October 2020.

In the 2005 project the inclusion of all 21 measured photographic support points produced non-negligible residuals. In the analysis of the results, some points were appropriately repositioned and others completely removed if the error was too high. However, it was observed that no significant improvement was obtained by repositioning.

The study highlights the intrinsic limits of the aero-photogrammetric analysis technique which, to a small extent, reduces the applicability of such techniques to the study of slope instabilities. It was observed that, although the precision of the photogrammetric processing was accurate and precise, the results associated with it did not reflect the precision followed at all. The study of the photogrammetric projects from 2005 first, and then from 1982, did not provide the precision required for the study of deformations. For example, in the 2005 aerial photogrammetric project, the deviations associated with this model are approximately 40 centimetres in the planimetric directions (x,y), which is too high to accurately assess deformations that, as will be subsequently observed, are of the order of magnitude of a few centimetres per year. The same reasoning is valid for the 1982 project, as deviations in planimetric direction of more than 30 centimetres are observed. For both photogrammetric models, the Digital Elevation Model (DEM) was subsequently created so that a digital discretization of the terrain could be obtained and, perhaps, the two DEMs could be compared for a detailed analysis of the morphological variation of the terrain. This was also not possible because the flight altitude was too high for the required precision.

On the 14th of October 2020, the fourth measurement of the GPS network by the Laboratory of Surveying and Geomatics of the University of Padua began. The other three measurement campaigns date back to 23 October 2018, 05 June 2019 and 05 October 2019.

The fourth measurement involved 11 points of a static GNSS network implemented for the monitoring of ground deformations. The network, in its entirety, can be characterized by "sub - networks" such as the "inner network" and the "outer network". The external network is composed of 3 different points: the static points 1000 and 2000 and the permanent point "Schio".
It is of fundamental importance that the points constituting the external network maintain the same coordinates in time, or better, that they are not affected by kinematics. If this were to happen, the entire GNSS processing would be invalid as it would not estimate the true results of the deformations of the points in the inner network.
On that day and the following day, the various points were connected to each other in order to construct baselines, i.e., 3D vectors that travel through the space between two user segments connecting the centres of the receiving antennas.
The procedure for analysing the measurements was then divided into four distinct phases that can be summarised as follows:
- First processing: Baseline calculation;
- Second processing: Free Grid Compensation or Intrinsic Compensation;
- Third processing: External Network Compensation;
- Fourth processing: Constrained Compensation of the internal network.

1st processing

The first processing for the analysis of GNSS data concerns the calculation of the bases, that are those spatial vectors that make up the network.
The first stage of the process for processing the bases, to be carried out through the Laica Infinity Software, is the assignment, within the program, of the "Master" station and the "Rover" station. Point 2000 in San Quirico was chosen as the Master station, while point 1000 in Recoaro Terme was chosen as the Rover station. Subsequently, the precise ephemerides were downloaded from the IGS (International GNSS Service) website and imported into the software. The first base created by the program is "SCHI - 1000", i.e. the connection between the permanent station of Schio and the "Rover" station. The program then created the second base, i.e. the space segment "2000 - 1000". Figure 15 shows a picture of the complete construction of the network through all the baselines.

2nd processing

The main purpose of Free (or Intrinsic) Grid Compensation is to assess what result is obtained without any compensation constraints. This process is carried out to ensure that no external forces have disturbed the point survey such as tampering with the instrument due to vandalism or generally any movement of the tripod. This process is necessary because, if the data do not conform, it is useless to proceed with subsequent processing.
Again, through the Laica Infinity software, the result of the compensation of the indirect observations, obtained through a least squares compensation technique, provides the final results of the measurement and their deviations.
The output results are expressed in latitude, longitude and ellipsoid coordinates in the WGS 84 reference system (World Geodetic System 1984). The actual accuracies are the standard deviations, i.e., the actual accuracies to be evaluated for monitoring. The

calculated standard deviations are not the accuracies of the bases but geometric accuracies, due to compensation, from the geometric constraints provided by the bases.
Very low standard deviations are observed, representing a very high quality of the received data. The highest value, in fact, does not even reach 5 millimetres.

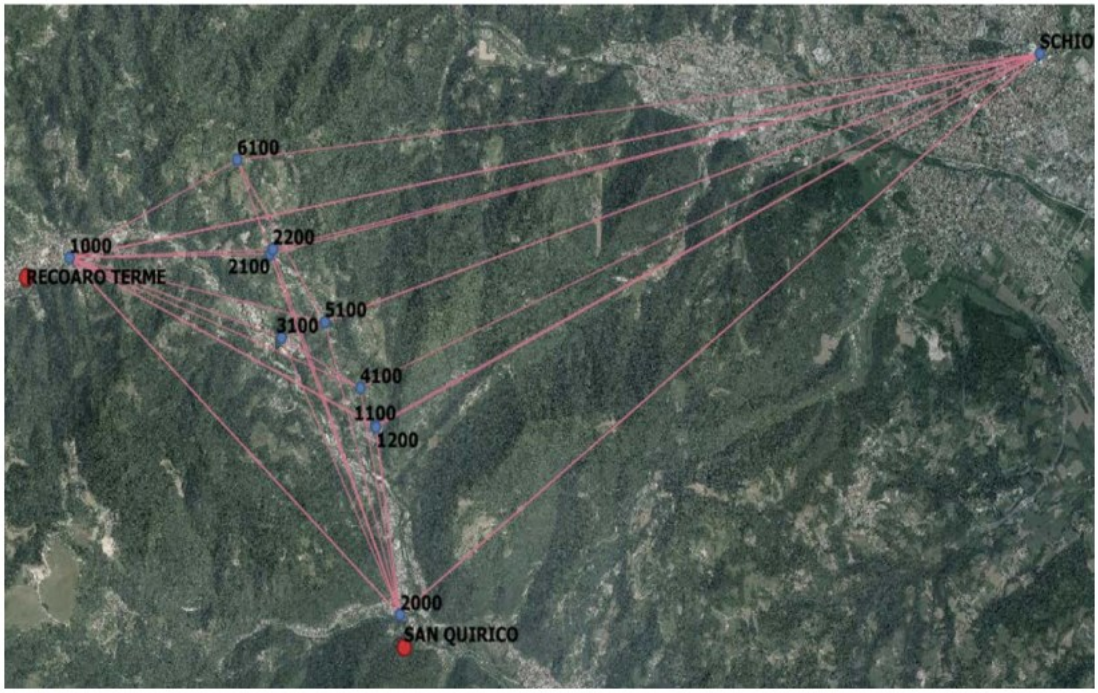

Figure 15: Construction of the network through all the baselines [2]

3rd processing

The network outside the landslide, used for monitoring, is composed of the 1000, 2000 and SCHI points.
The latter is a permanent network and the Veneto GPS Network performs weekly recalculation of the coordinates of the permanent stations.
The main purpose of the External Network Compensation is to assess that the external points, measured with high precision instrumentation, are not subject to displacement and deformation over time. These points must have the same coordinates as in the first measurement campaign, i.e., the complete absence of kinematics is required in the time frame of the measurement acquisition. If indeed the points of the external network are stationary, the deformations of the points within the landslide area can be correctly evaluated. In the calculation, only the baselines of the three external points on the three survey days are taken into account, resulting in 9 baselines. At this stage of the compensation, the point "SCHI" is fixed with known coordinates. The unknowns of the reference system rototranslation problem are 7. This operation is also a least squares compensation.

Risultati della compensazione			
Stazione	Corr. Lat. WGS 84	Corr. Long. WGS 84	Corr. Quota
1000	-0.0001	0.0000	0.0005
2000	-0.0002	0.0000	0.0005
SCHI	0.0000	0.0000	0.0000

Table 1: Compensated Coordinate Corrections - External Network Compensation [2]

These residuals therefore indicate that points 1000 and 2000 have remained unchanged over time since the first measurement campaign.
It is evident that there can be no corrections or standard deviations in the Schio receiver as it is the only fixed point of known coordinates.

4th processing
This analysis is carried out without the permanent station of Schio (SCHI), but all the points of the internal network are fixed with the two points 1000 and 2000 of the external network.
At the end of this compensation all the coordinates of the points of the internal network, i.e. the points within the landslide perimeter, can be compared with the coordinates of the other measurements of the past years. This makes it possible to check whether there has been any deformation of the measured points in the form of a change in coordinates. If the delta between coordinates of the same point, measured at different times, is less than the accuracy of the measurements, it must not be referred to a deformation. Basically, all points whose delta is less than the accuracy can be considered free of kinematics.

MONITORING AND DEFORMATION ANALYSIS
The tables below represent the ellipsoidal heights obtained at the end of the compensation process.
In the delta values, the measurements of the least recent elevations (Measurement 1 in October 2018, Measurement 2 in June 2019 and Measurement 3 in October 2019) are subtracted from the most recent measurement (Measurement 4 in October 2020). A negative delta will therefore represent a lowering of the quota point.

	Misura 1 - Ottobre 2018	Misura 4 - Ottobre 2020	
ID	H elliss.[m]	H elliss.[m]	Delta [m]
1000	489.616	489.616	0.000
2000	381.676	381.676	0.000
1100	464.754	464.749	-0.005
1200	466.513	466.510	-0.003
2100	639.922	639.914	-0.008
2200	642.137	642.130	-0.006
3100	452.601	452.604	0.004
4100	545.076	545.085	0.010
5100	573.481	573.492	0.011
6100	707.672	707.697	0.025

Table 2: Delta H between measures of October 2018 and October 2020 [2]

	Misura 2 - Giugno 2019	Misura 4 - Ottobre 2020	
ID	H elliss.[m]	H elliss.[m]	Delta [m]
1000	489.616	489.616	0.000
2000	381.676	381.676	0.000
1100	464.737	464.749	0.011
1200	466.511	466.510	0.000
2100	639.905	639.914	0.008
2200	642.113	642.130	0.018
3100	452.566	452.604	0.038
4100	545.046	545.085	0.040
5100	573.484	573.492	0.008
6100	707.666	707.697	0.031

Table 3: Delta H between measures of June 2019 and October 2020 [2]

	Misura 3 - Ottobre 2019	Misura 4 - Ottobre 2020	
ID	H elliss.[m]	H elliss.[m]	Delta [m]
1000	489.616	489.616	0.000
2000	381.676	381.676	0.000
1100	464.755	464.749	-0.007
1200	466.515	466.510	-0.005
2100	639.904	639.914	0.010
2200	642.117	642.130	0.014
3100	452.601	452.604	0.003
4100	545.082	545.085	0.003
5100	573.481	573.492	0.011
6100	707.687	707.697	0.010

Table 4: Delta H between measures of October 2019 and October 2020 [2]

	Delta Misura 1 - Ottobre 2018 e Misura 4 - Ottobre 2020		
ID	Delta EST [m]	Delta NORD [m]	Delta H geo. [m]
1000	0.000	0.000	0.000
2000	0.000	0.000	0.000
SCHI	0.000	0.000	0.000
1100	-0.005	-0.006	-0.006
1200	-0.007	-0.003	-0.003
2100	-0.015	-0.006	-0.008
2200	-0.020	-0.010	-0.006
3100	-0.002	-0.009	0.003
4100	-0.002	-0.013	0.010
5100	-0.005	-0.006	0.011
6100	-0.013	-0.009	0.025

Table 5: Delta of planar coordinates between measures of October 2018 and October 2020 [2]

An important concept is to establish how points inside the landslide move with respect to flat coordinates in an EAST - NORTH reference system. In order to construct vectors that indicate the deviation in time within a map system, it is necessary to transform the geocentric coordinates (ϕ, λ), provided by the GPS, into plane coordinates projected onto a map. The operation of projecting ellipsoidal coordinates into the map plane produces deformations. In this paper two different cartographic systems will be used. The first is the "Fuso 12" cartographic plane, which is a system that allows us to limit deformations in the Veneto Region. The second cartographic system used is UTM32 (Universal Transvers Mercator), although it provides higher deformations.

The planimetric deformation modulus is defined as that two-dimensional vector with origin in the coordinate point of the first measurement campaign and vertex in the new planimetric arrangement following slope deformation.
The maximum planimetric deformation vector created concerns point 2200 inside the landslide perimeter located in 'Contrada Piazza' in the 'Fuso 12' cartographic system. The intensity of the planimetric deformation modulus is 2.2 linear centimetres. This type of sliding occurred over a period of only two years, i.e. between the first measurement campaign in October 2018 and the last one in October 2020.

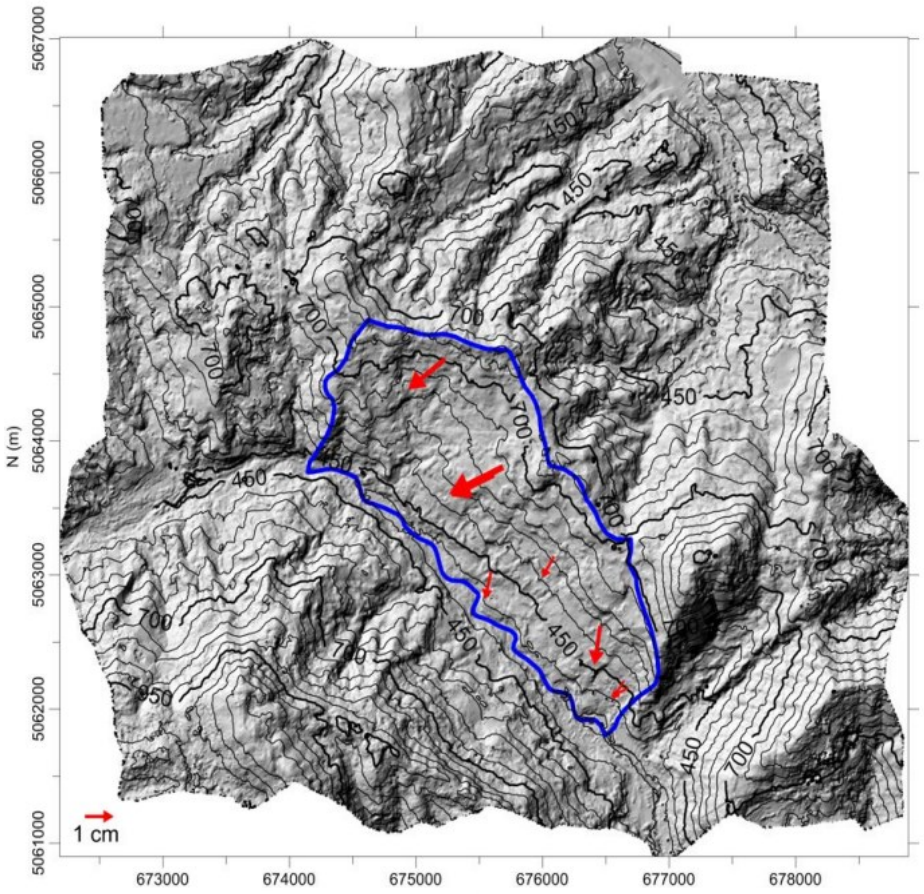

Figure 16: Planimetric Deformation Modulus 2018 - 2020 on Shaded Relief [2]

The analyses carried out on the behaviour of the Rovegliana slope by means of GNSS satellite analysis made it possible to identify the most unstable zones in the area analysed. The use of data acquired with high-precision measurements lasting more than three hours of continuous acquisition made it possible to analyse a long time series of information. It was therefore possible to identify the areas characterised by stable deformation dynamics over time and those that have undergone acceleration. In particular, it emerged that the areas that underwent the greatest acceleration were those located in the northern portion of the slope, in contrada Piazza and Sigismondi. The deformations determined in the GNSS monitoring were clearly of small entity, since the total period of measurement was only two years with four associated campaigns. However, deformations were observed in all the sampled points of the network inside the landslide perimeter, with displacements of the order of a few centimetres. Most of the deformation vectors have a direction compatible with the displacements expected along the line of maximum slope gradient. The direction of deformation is orthogonal to

the contour lines of the CTR (Carta Tecnica Regionale - Regional Technical Map) which, in the figure, is superimposed on the Shaded Relief which was obtained thanks to the 2005 photogrammetric model. The deformations have expected directions and lead the system towards the condition of minimum potential energy. More specifically, the northern part of the slope has large planimetric displacements, up to a maximum of 2.2 cm at point 2200 located in Contrada Piazza. Another planimetric deviation of great intensity can be found in the locality Sigismondi at point 6100 and equal to 1.6 cm. The same intensity of the latter is at point 2100, also in the Piazza locality. In conclusion, it is possible to state that the Rovegliana area is affected by widespread instability in the entire domain.

3.2 Studio generale delle condizioni geostatiche dell'abitato di Rovegliana in comune di Recoaro Terme (VI) [1]

In the first part of the report, the data from satellite RADAR interferometry are analysed by integrating existing products (ERS, Envisat) with those recently acquired by the University of Padua (COSMO-SkyMed).
In particular, the time series of ERS and Envisat data for the period 1995-2000 and 2003-2010 respectively will be compared. These data will be integrated with the information on the displacements between 2010 and 2012 obtained with the SBAS processing of the COSMO-SkyMed images.

ERS AND ENVISAT DATA
Due to the large number of data available, processing was carried out using both the PS and SBAS techniques. The DInSAR analysis made it possible to identify the landslide movements affecting the slope, many of which are not identified in the IFFI catalogue. Moreover, thanks to the availability of the historical series of ERS and ENVISAT data, it was possible to identify the state of activity of the present landslides, identifying any acceleration phases in the historical series of displacements from 1995 to 2010.
In the northern part of the slope under study, both ERS and ENVISAT data show a continuous movement of the contrada Piazza (landslide n. 2 in Figure 3) and contrada Branchi (landslide n. 4, Figure 3) from 1995 to 2010. The instability located in contrada Cappellazzi, at the southern borders of the study area, already identified in the IFFI database, confirms the validity of the PS and SBAS analysis also in relation to the available displacement data, obtained by a topographic survey, which confirm the movement. Differential interferometric analyses have made it possible to identify areas subjected to movement as they identify objects that have undergone displacement during the observed period (1995- 2010).
Examples of the displacement series of some PS and descending SBAS points are given below.
Landslide n. 2 is located in the contrada Piazza and shows continuous displacements from 1995 to 2010, so it is defined as an active landslide. The graphs in the Figure show the complete displacement series for three descending ERS PS points and the corresponding descending ENVISAT PS points.

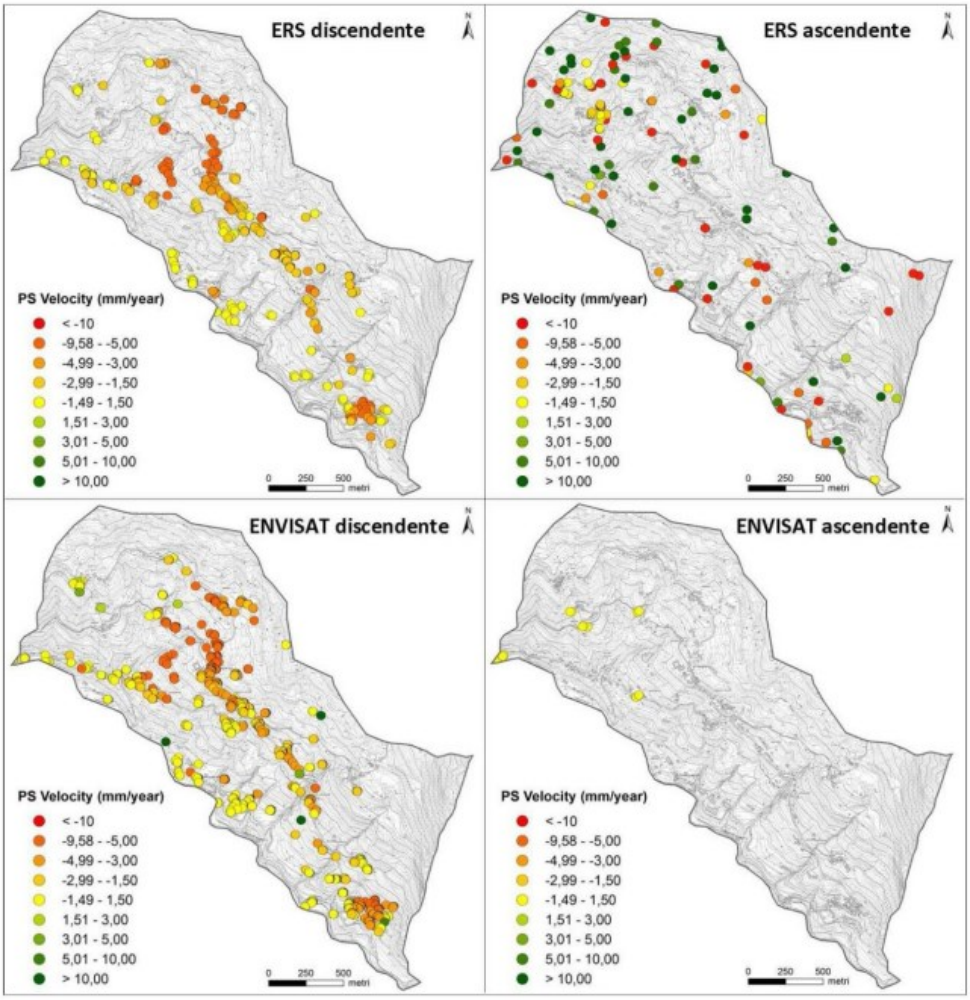

Figure 17: Interferometric results using Persistent Scatterers methods for descending and ascending images from ERS1 - ERS2 satellites [1]

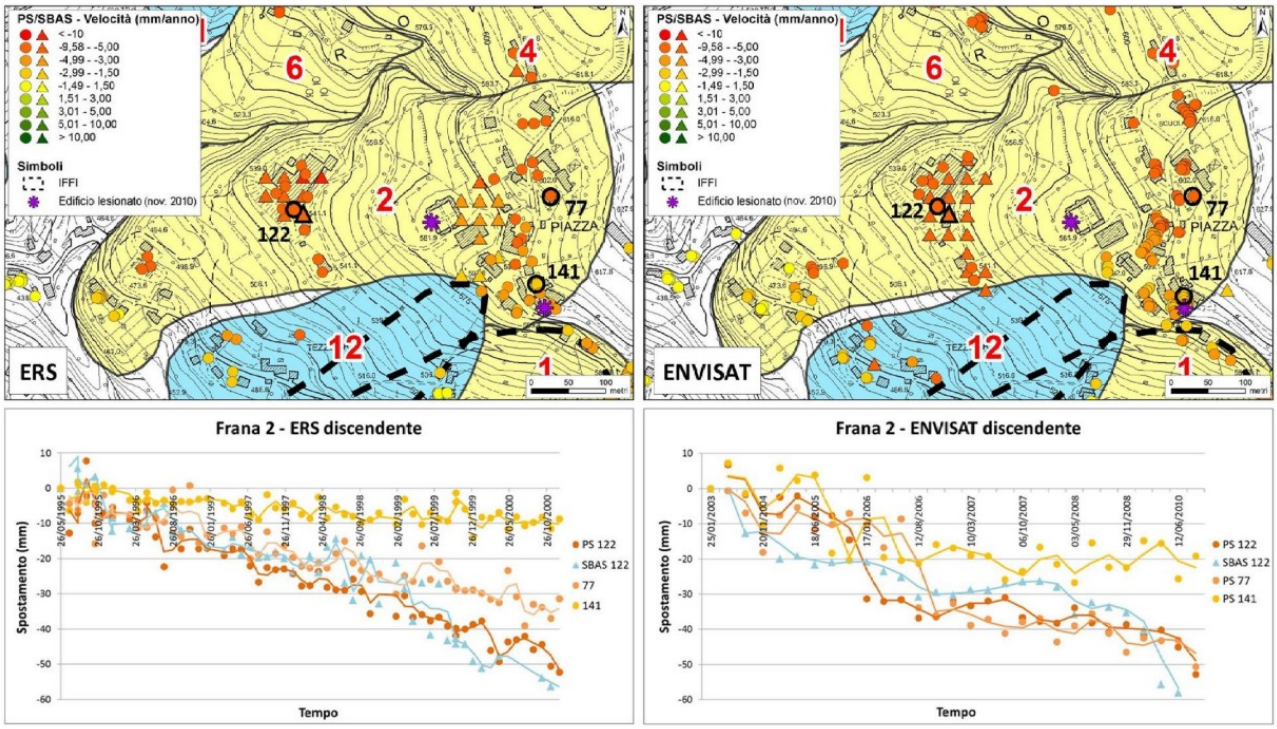

Figure 18: Landslide n. 2 Development of PS and SBAS points ERS and Envisat descending from 1995 to 2010 [1]

The graphs of landslide n. 4 describe temporal displacements of targets with higher and lower rates of movement, (ERS velocity: PS 10 = -6.50 mm/year; PS 17 = -5.85 mm/year; PS 24 = -5.05 mm/year - ENVISAT velocity: PS 10 = -4.89 mm/year; PS 17 = -5.45 mm/year; PS 24 = -3.66 mm/year). Even in this case the landslide was defined as active, since over twenty years, it shows continuous displacements.
Landslide n. 1, classified as an area subjected to slow surface movements, is already present in the IFFI database but, thanks to the integration of satellite interferometric data, it was possible to redefine the upper and lower limits. In Figure 20, in fact, the graphs show that the buildings at the base of the landslide (PS 392, ERS1-2) underwent completely negligible movements (-0.83 mm/year), at least until December 2000, and therefore were not included within the landslide perimeter.
The PS and SBAS analyses identify very well the areas of movement, as they are able to quantify movements in the order of millimetres per year. As a result, areas with different annual velocity rates are identified almost perfectly if targets are present (in the case of PS) or spatial coherence is medium to high (in the case of SBAS points).

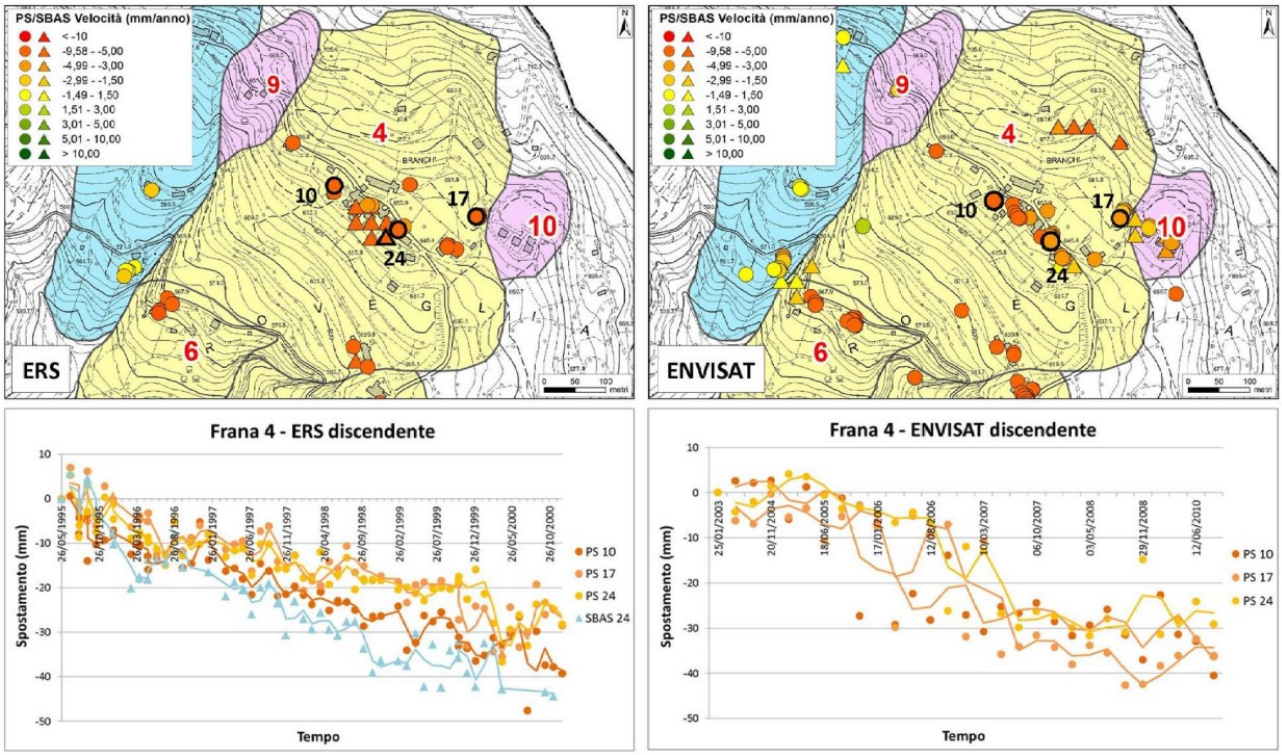

Figure 19: Landslide n. 4 Development of PS and SBAS points ERS and Envisat descending from 1995 to 2010 [1]

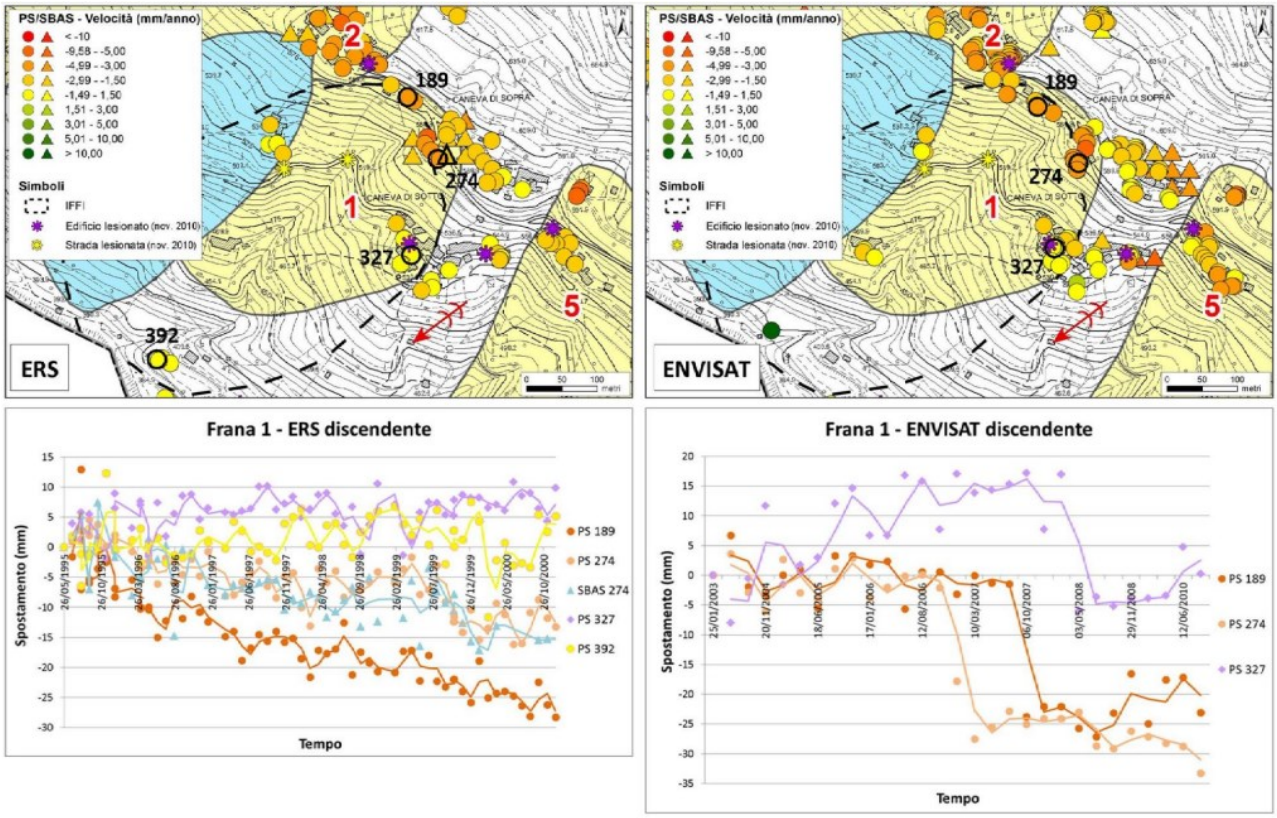

Figure 20: Landslide n. 1 Development of PS and SBAS points ERS and Envisat descending from 1995 to 2010 [1]

In order to assess the magnitude of surface displacements of the slope, following the exceptional rainfall event that hit the area of the Vicentine Prealps in November 2010, a series of COSMO-SkyMed (CSK) images were acquired for a temporal interval straddling the exceptional rainfall, in correspondence with the affected area. However, the CSK data are more sensitive to vegetation and its seasonal changes, due to the shorter wavelength of the electromagnetic radiation. Therefore, the analysis of such data in the Rovegliana area, characterised by the presence of small clusters of houses scattered in a densely vegetated slope, does not facilitate the obtaining of results with good spatial coverage, both with the PS and SBAS techniques.

The figure 21 shows the map of the velocities in the entire area of Rovegliana, the result of processing the CSK data. These velocities actually correspond to a component of the displacement velocity, i.e. the projection of the velocity along the direction of the satellite's line of sight (line that connects the satellite with the monitored object), therefore already in itself an underestimation of the real velocity, which can only be defined by knowing the real direction of displacement of the surface, or by having available results obtained with data acquired with both an ascending and a descending orbit.

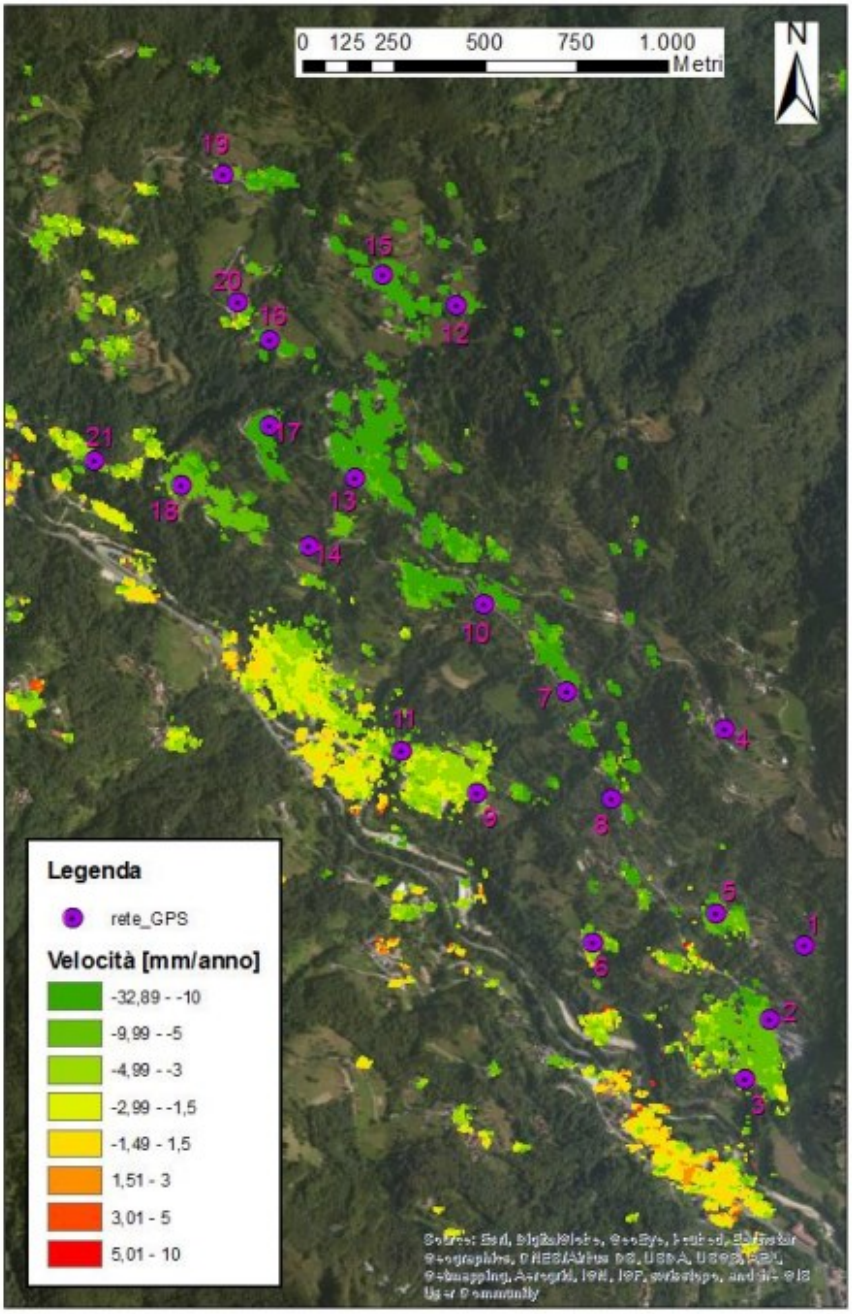

Figure 21: Velocity map, covering the period April 2010 - September 2012, obtained by processing COSMO-SkyMed data using the SBAS technique [1]

The same figure also shows the positioning of the GPS points of the monitoring carried out between October and December 2015. In order to get an idea of the state of activity of the areas subject to GPS monitoring, diagrams of the displacements at some of these points have been plotted.
I report here only those that are considered the most critical:

- Point 10, located in the Contrada Piazza, near the church square, which reaches a velocity of about 13 mm/year (Figure 22);
- Point 15, located in Contrada Branchi, which reaches a velocity of approximately 16 mm/year (Figure 23);
- Point 17, located in a barycentric position between the localities Piazza, Branchi and Angrimani, which reaches a speed of about 12 mm/year (Figure 24).

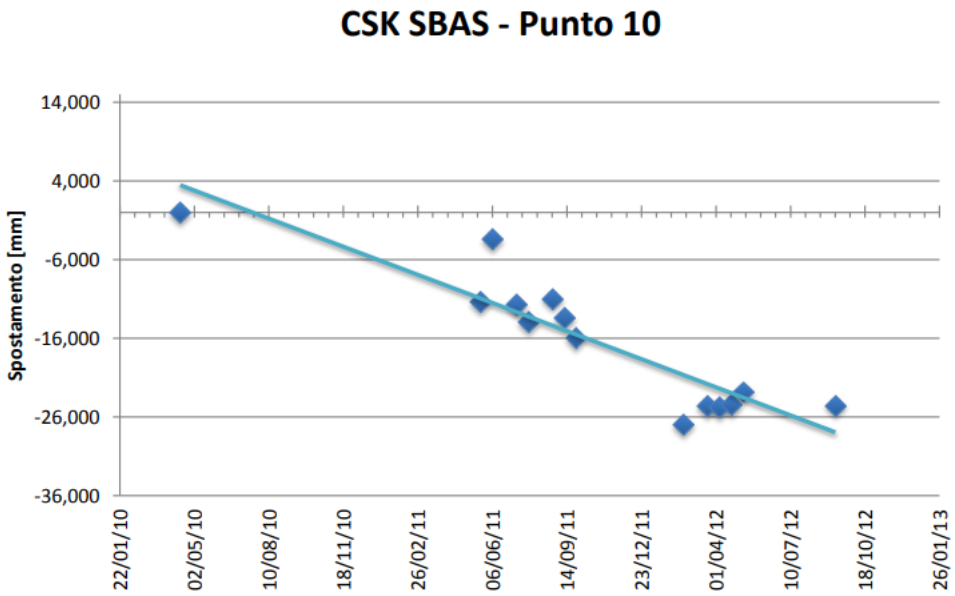

Figure 22: Displacement of point 10 during time [1]

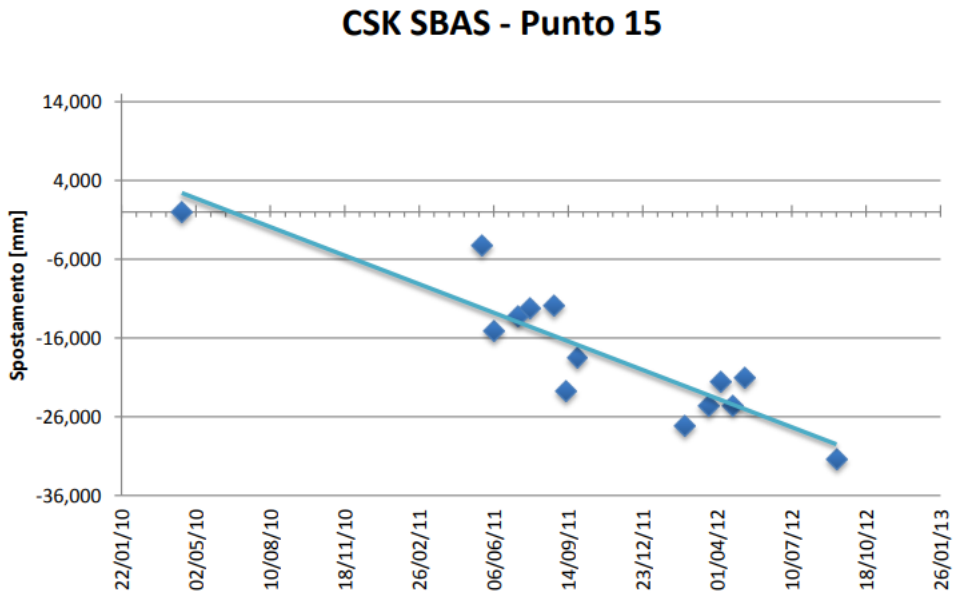

Figure 23: Displacement of point 15 during time [1]

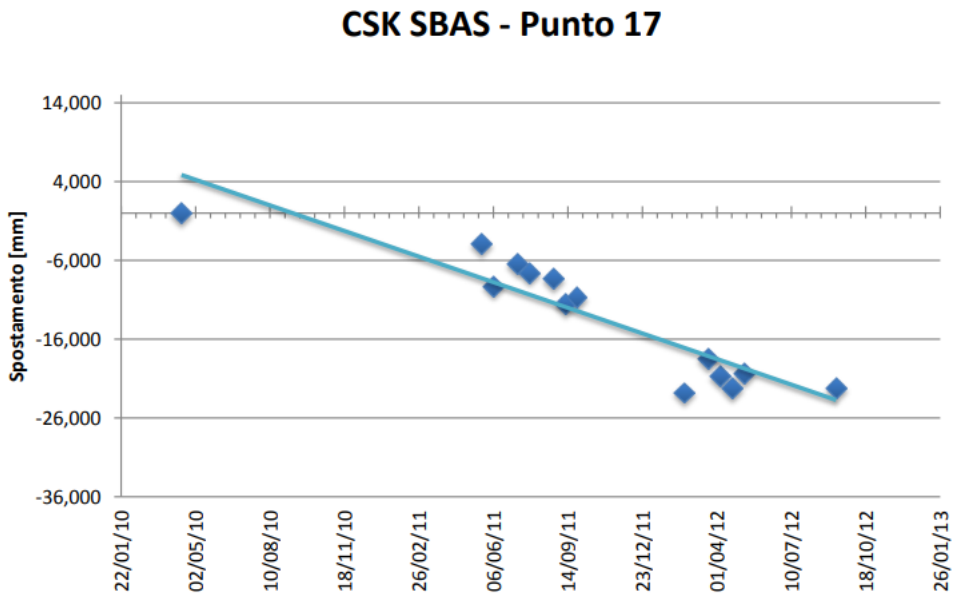

Figure 24: Displacement of point 17 during time [1]

In order to facilitate the comparison throughout the time interval of available data, the ERS, Envisat and COSMO-SkyMed data have been plotted in a single map, extracted from the webgis project, with the same classification scale, so as to easily identify the areas that have slowed down over time, those subject to acceleration and those with stable behaviour over time (Figure 25). By carefully observing the results shown in the figure, it can be seen that the areas subject to deformation in the three time periods 1992 - 2000, 2002-2010, 2010- 2012, corresponding respectively to the results obtained with ERS, Envisat and COSMO-SkyMed data, present an almost constant behaviour over time. It is noted that some areas are subject to a slight acceleration at the turn of the period 2010 - 2012, a period in which the intense rains that affected the entire Vicentino occurred.

In particular, it has emerged that the areas that have undergone a greater acceleration in the period 2010 - 2012 are those located in the central portion of the slope, between the localities Piazza and Fracassi, which have accelerated from speed ranges between -1.5 ÷ 1.5 mm/year, -1.5 ÷ -3 mm/year, -3 ÷ -5 mm/year, up to speeds even higher than -10 mm/year.

The information obtained from the interferometric data was also the starting point for defining the location of the points belonging to the GPS network of the monitoring carried out between October and December 2015, in order to analyse in greater detail, the behaviour of particularly fragile areas.

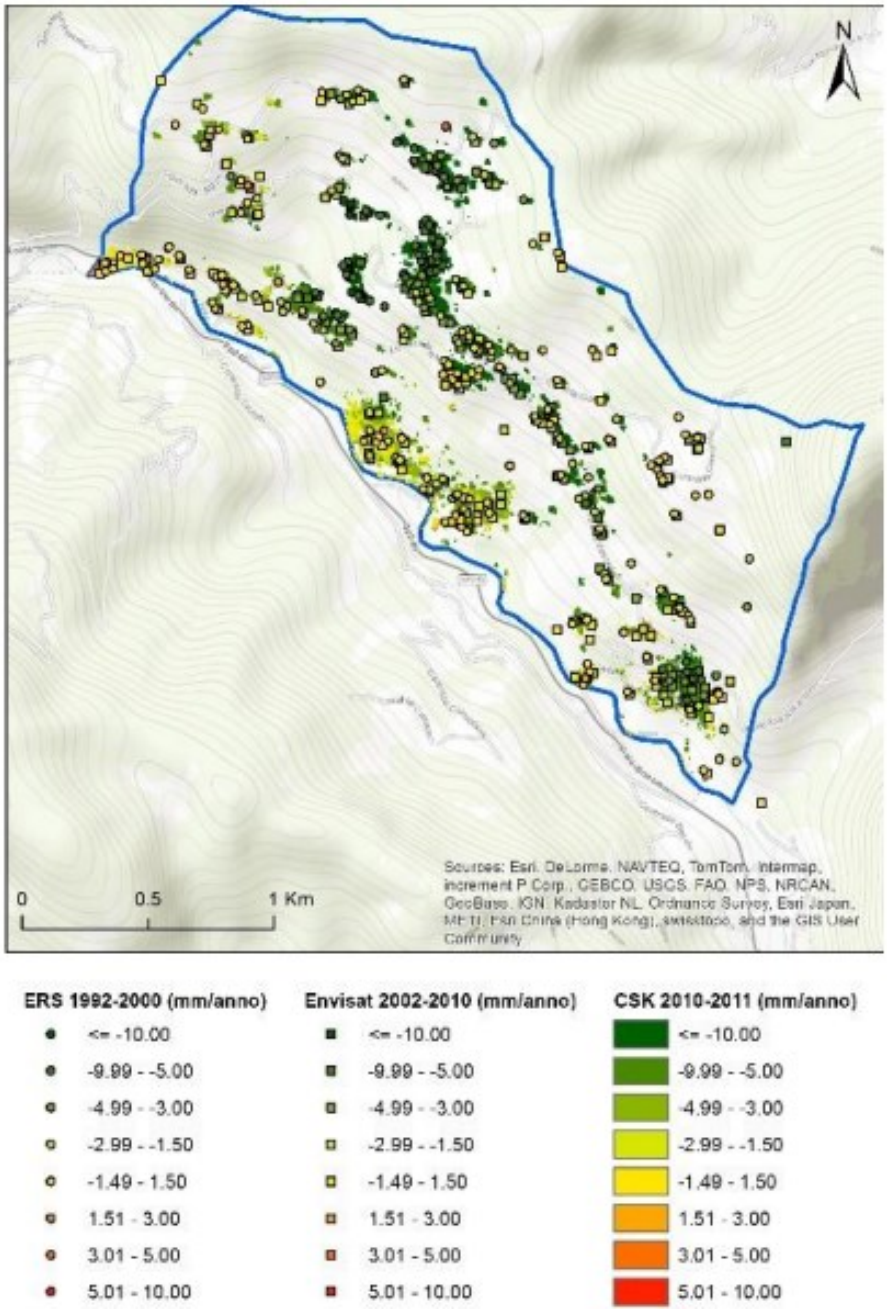

Figure 25: Map of the deformation rates of the Rovegliana slope, in mm/year, obtained from ERS (period 1992 - 2000), Envisat (period 2002 - 2010) and COSMO-SkyMed (period 2010-2012) data [1]

MONITORING WITH GNSS SATELLITE METHODOLOGY

The Laboratory of Surveying and Geomatics of the University of Padua has undertaken a series of high-precision geodetic measurement campaigns for the Rovegliana area. The initial measurement took place on days 26-27 of October 2015 with repetition on days 26-27 of November 2015. The measurements involved 22 points of a GNSS static network implemented for the monitoring of ground deformations. The 22 network points were intrinsically connected by 49 baselines in the first measurement, and by 57 baselines in the second measurement.

The 22 points of the Rovegliana network are the following: one point (100) was materialized in Recoaro Terme and constitutes the reference point and the other 21 benchmarks were permanently materialized in the Rovegliana area as shown in figure 26.

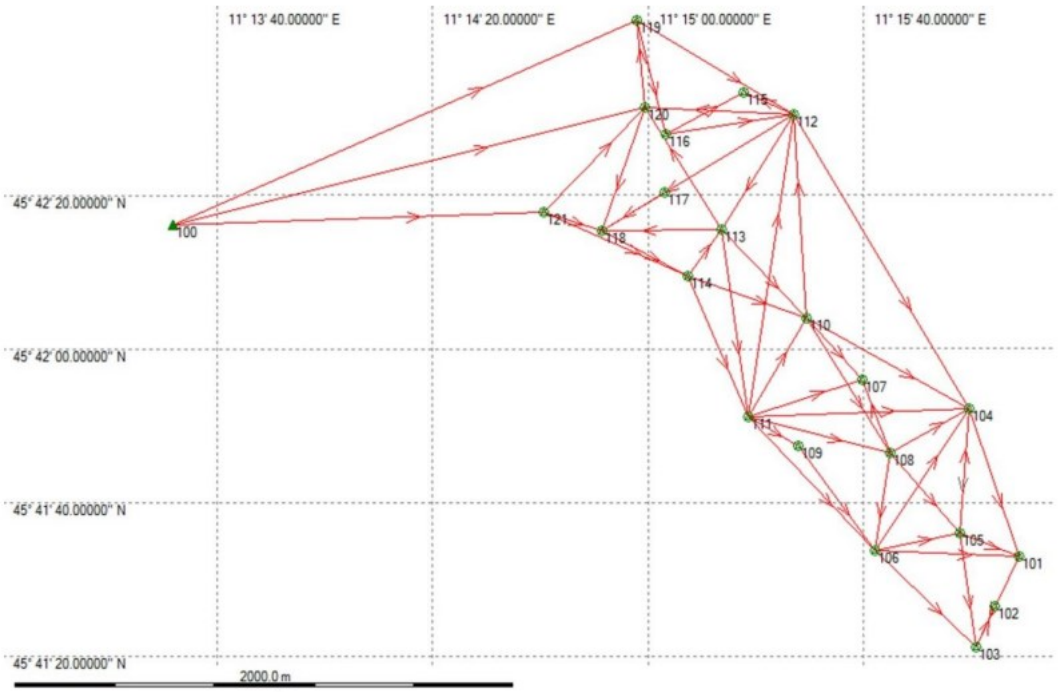

Figure 26: Network and connections made in the first measurement campaign in October 2015 [1]

Initially, the compensation of the constrained type was carried out by calculating the compensated coordinates of only point 100 by connecting it to the permanent stations. Subsequently, the overall compensation of the two measurements was carried out in an intrinsic way by binding only point 100 with the coordinates determined in the first compensation. This type of calculation allows to evaluate the presence of possible gross errors on the observations.

Following the report of the compensation of the first measurement, it is evident that the maximum value of the mean square deviation of the vertex coordinates is equal to 1.2 cm in height with a mean value equal to 4 mm.

For the second measurement, on the other hand, the maximum value of the mean square deviation of the vertex coordinates is equal to 1.6 cm in height with a mean value of 8 mm.

Using the ConVE software of the Veneto Region, the initial coordinates of the network points were transformed into the ETRF2000 reference system.

The geocentric Cartesian coordinates in the ETRF2000 reference system determined in the two measurements were then compared and the comparisons were reported both monodimensionally along the three Cartesian directions X Y Z and three-dimensionally with the modulus of the 3D displacement vector.

For the evaluation of the planimetric displacements, the plane coordinates in the UTM32 plane reference system are compared both one-dimensionally along East, along North and 2D.

The 2D displacement vectors, geo-referenced in the TM32 map system, were plotted in the GIS environment. The result is shown in Figure 27. The deformations determined in this monitoring, with a short duration of one month, are clearly of small magnitude and comparable, in the average value, with the sensitivity attainable with the GNSS methodology and therefore of little significance. It can be noted, however, that most of the deformation vectors are of a direction compatible with the displacements expected along the line of maximum slope gradient.
The GPS network created constitutes, however, an important starting point for any future monitoring of the evolution of the unstable slopes of Rovegliana.

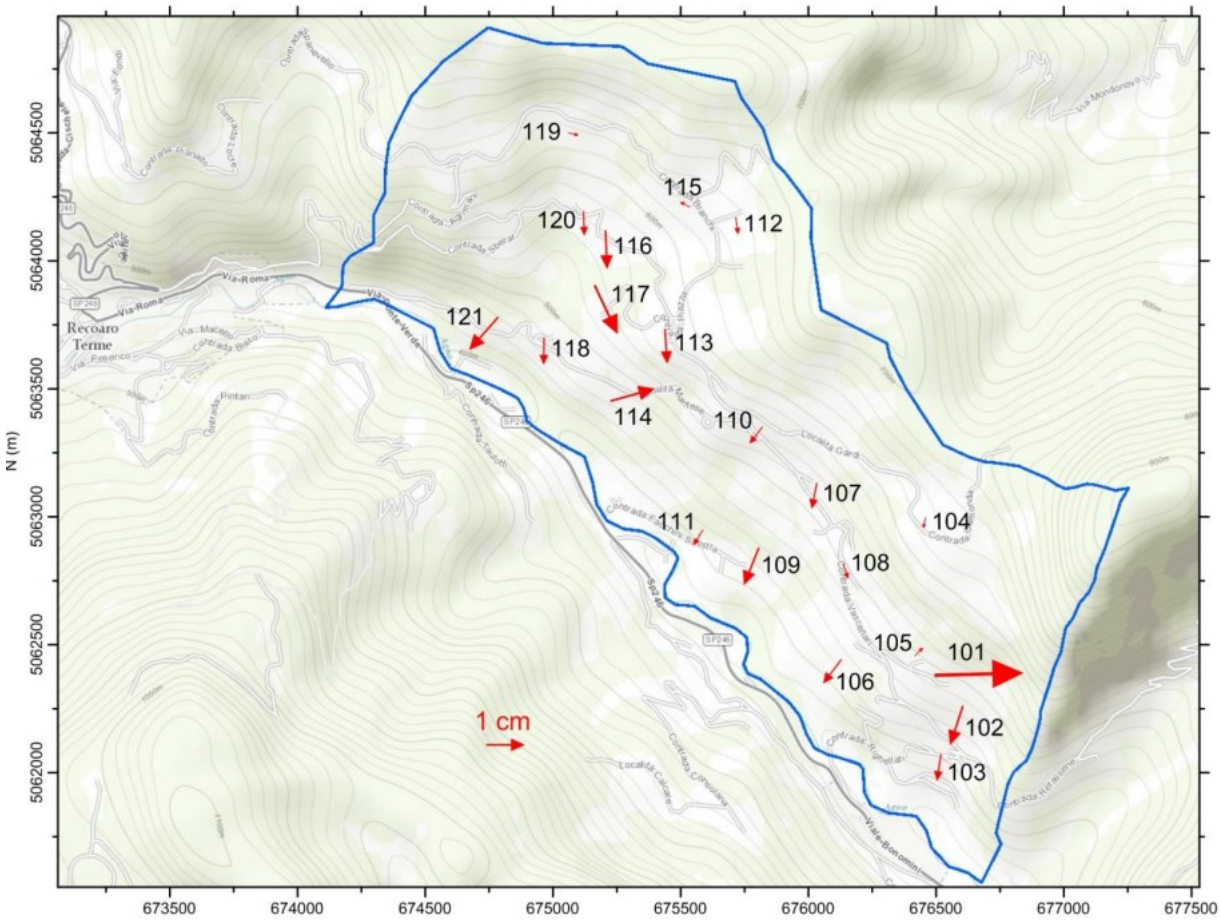

Figure 27: Planimetric deformation vectors in the Gaussian plane [1]

SURVEY WITH LASER SCANNER METHODOLODY

The Laboratory of Surveying and Geomatics used the TLS -Terrestrial Laser Scanning- methodology to survey two buildings located in particularly critical areas. In particular, it was decided to investigate possible short-term displacements in the Fracassi and Vascellari quarters where, as in other contexts on the Rovegliana slope, damage to buildings and various infrastructures was found.
The instrument used for the survey is the Leica ScanStation P20, with high precision and high scanning speed. The accuracy of distance measurements is ±1 mm, while angular measurements are accurate to 8". The measurement range is from 0.4 to approximately 120 m.
The measurement campaigns took place in October and November and the data obtained were processed with the intention of identifying any deformations that may have occurred in the period between the two surveys. Two different approaches were

tested, comparing the surface model (mesh) with the point cloud (with JRC Reconstructor software), and between two-point clouds (with Cloud Compare software). The two methods provided consistent results, and both did not show any deformation events at the two sites under study or, in any case, of such an entity (≤ 5 mm) as to be reliably detected with the laser scanning technique. The acquisitions were carried out with a very close repetition period, 13 days for Fracassi and 30 days for Vascellari. In view of the fact that it is highly unlikely that there was any movement of the slope of an entity detectable with the aforementioned methodology, the results of the elaborations are to be considered reliable, also with regard to the verification using two different methods of comparison. The data sets acquired to date will therefore provide the basis for subsequent analyses of new surveys that may be carried out following exceptional events or for standard monitoring of deformations in the areas under investigation.

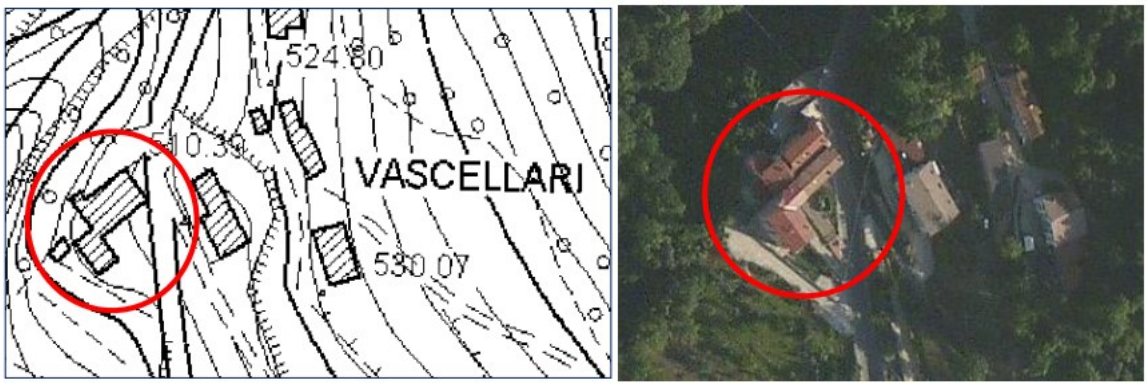

Figure 28: Location of the site in the contrada Vascellari [1]

Figure 29: Location of the site in the contrada Fracassi [1]

Figure 30: Detail of the contact strip between buildings in the contrada Vascellari (IRC Reconstructor) [1]

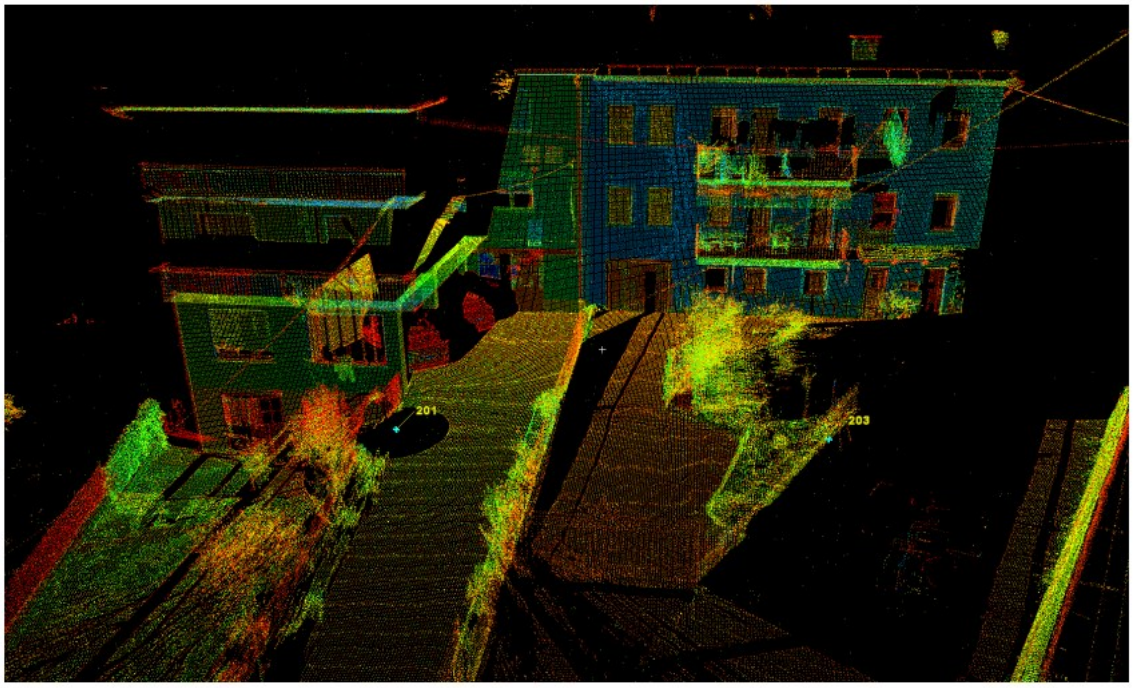

Figure 31: Detail view of the building in contrada Vascellari (Cyclone) [1]

RAINFALL-INSTABILITY RELATIONS

In order to assess the state of activity of landslide phenomena in the Rovegliana area, the amount of rainfall in a given time span was compared with the ground displacements acquired by SAR (Synthetic Aperture Radar). The numbering of phenomena to be referred to is shown in Figure 32.

Specifically, the amount of rainfall was related to the displacement data provided by the ERS satellite, which collected data, with some interruptions in acquisitions, from 1992 to 2003. Comparing the displacement graph with the rainfall, it is evident that the time intervals in which a greater intensity of precipitation occurred coincide with those characterised by significant displacements of the points acquired by the satellites. In

particular, in the period between October 1992 and June 1993, the ERS satellite detected displacements in more than one landslide described in the Landslide Map following an exceptional precipitation event (October 1992) during which 750 mm of rain fell.
Figure 33 shows that landslide 15, a diffuse surface landslide (creep movement) west of Contrada Piazza, shifted significantly from August 1992 to June 1993 (0.24 mm to -12.39 mm).

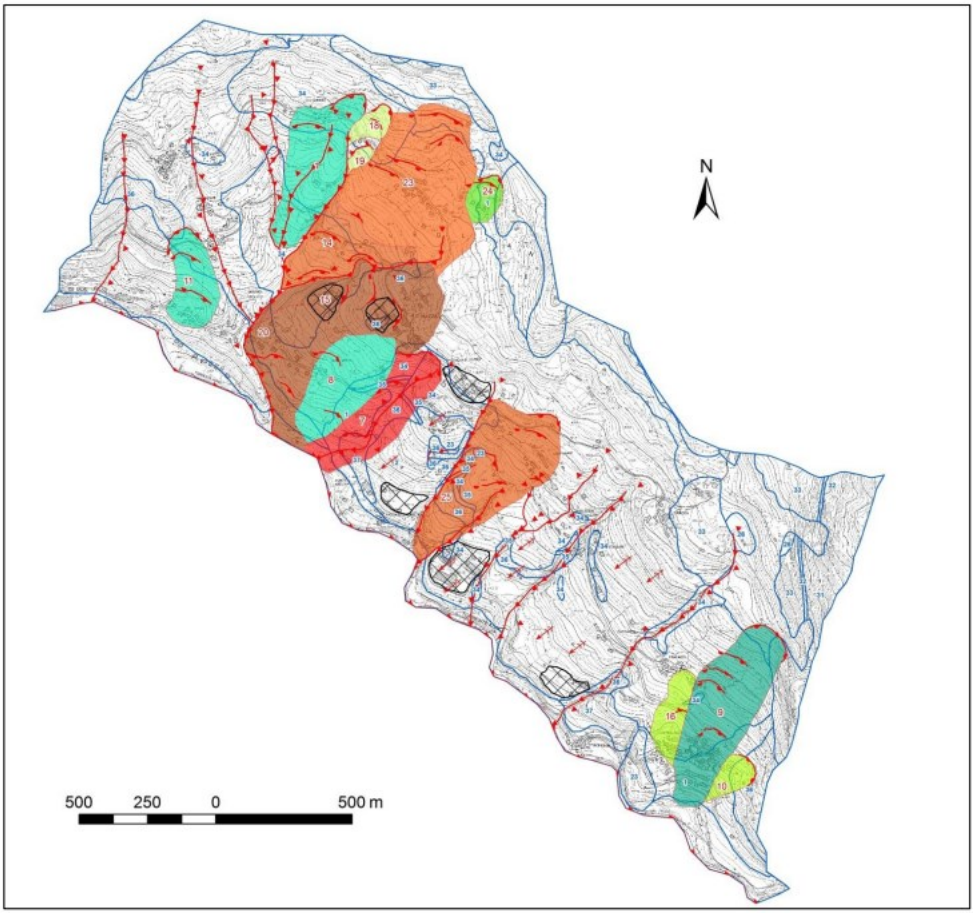

Figure 32: Map of landslide phenomena as a reference to the numbering of landslides referred to in the rainfall analysis [1]

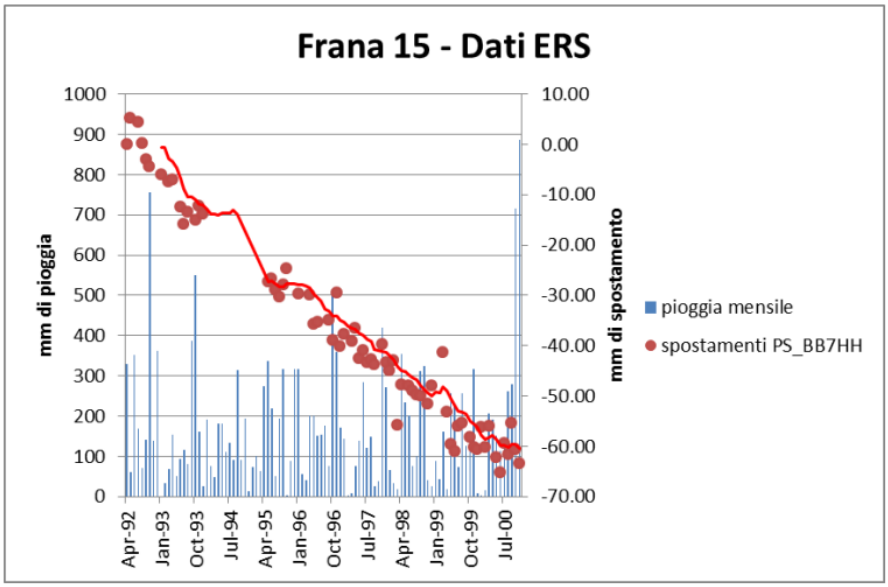

Figure 33: Precipitation-displacement graph of landslide 15 (ERS data) [1]

Figure 34 shows the rainfall-displacement graph of landslide 8, in correspondence with a translational phenomenon south of Contrada Piazza. From October 1992 to June 1993, the landslide moved a total of 20.23 mm

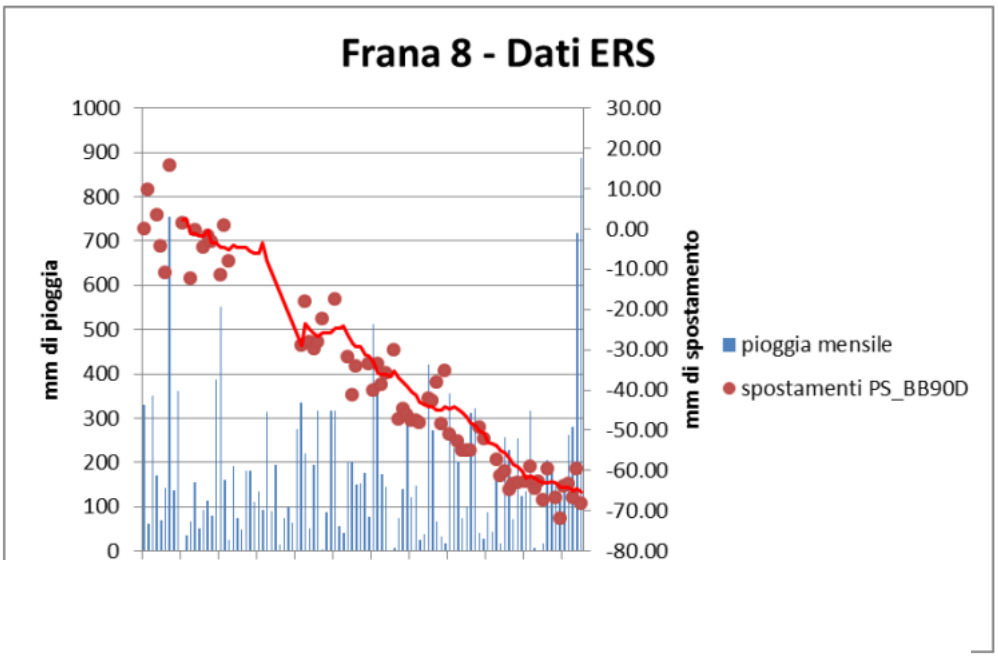

Figure 34: Precipitation-displacement graph of landslide 8 (ERS data) [1]

The figure 35 shows the trend of displacements of landslide 16, a rotational slip phenomenon to the west of Contrada Cappellazzi, specifically a total movement of about 20 mm.

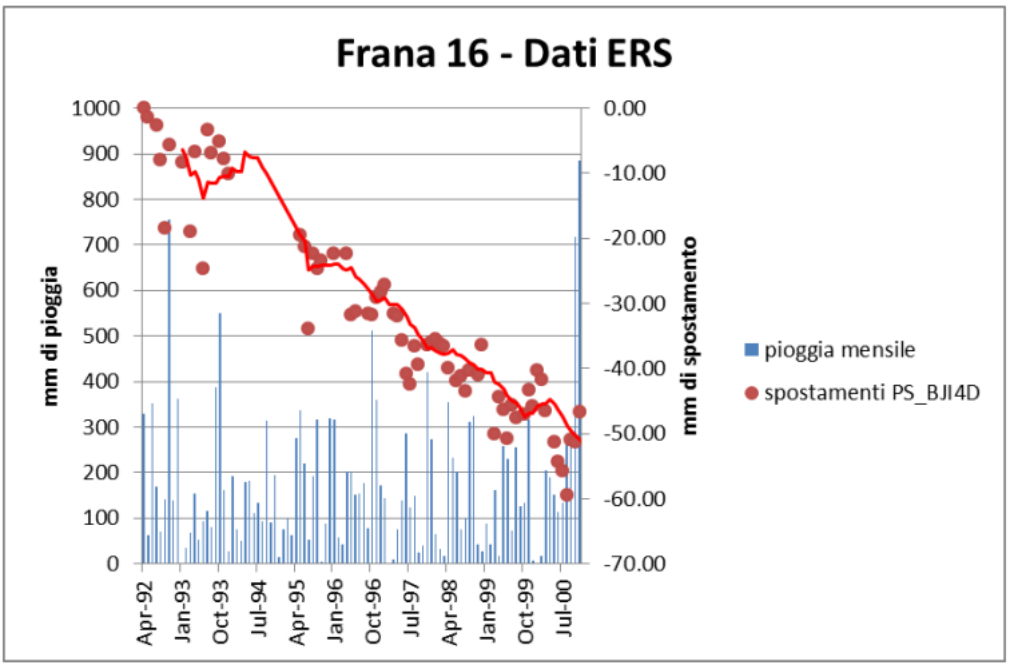

Figure 35: Precipitation-displacement graph of landslide 16 (ERS data) [1]

In the case of landslide 24, a rotational slide to the east of Contrada Branchi, there is a displacement of approximately 17.30 mm (Figure 36).

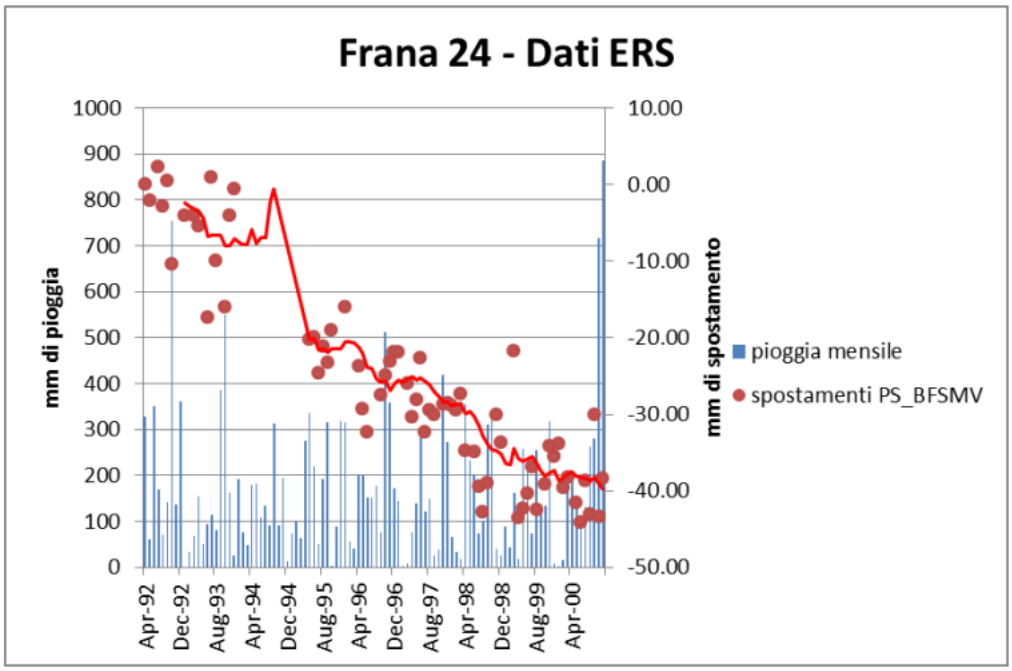

Figure 36: Precipitation-displacement graph of landslide 24 (ERS data) [1]

The landslide phenomena that underwent the greatest displacement (18-20 mm in less than a year) were landslides 8, 24 and 16, of which 16 and 24 are landslides characterised by a rotational kinematic type, while landslide 8 has a translational kinematic type.

3.3 Combining Sentinel-1 Interferometry and Ground-Based Geomatics Techniques for Monitoring Buildings Affected by Mass Movements [6]

In this paper, it was proposed a methodology to investigate the relationships between mass movements and damages to two masonry structures affected by relevant crack patterns: Rovegliana Church and a building located in Cappellazzi district (Figure 37).
The methodology is based on an effective integration of Sentinel-1 interferometry and ground-based geomatics techniques, such as global navigation satellite system (GNSS), terrestrial laser scanning (TLS) and structure from motion (SfM), supported by classical topographic measurements.
GNSS allows verifying the ground deformation estimated by MT-InSAR and provides a reference system for the TLS and SfM measurements, while TLS and SfM allow the behavior of buildings located in the investigated slope to be monitored in great detail.

Figure 37: Pictures of Rovegliana Church (a) and one of the most damaged buildings in Cappellazzi district (c–g). In (b), a large crack in the portico of the church is shown [6]

Sentinel-1 SAR data from 2014 to 2019 were processed through the SBAS technique to identify and monitor both the deformation of the two buildings and the evolution of the mass movements. In the first step, a network of reference and secondary image pairs is defined using temporal and perpendicular baseline constraints; the second step consists of images co-registration and interferograms generation (with the subtraction of topographic low frequencies), filtering and unwrapping for each pair. Inaccuracies due to satellites orbits and phase ramps are removed in the third step while in the fourth step mean heights and velocities are estimated and used to re-flatten each interferogram in the first inversion. Atmospheric corrections are performed in the second inversion (step

5), then displacements and heights (correction values and new elevation) related products are generated; finally, all processing results are geocoded in the selected cartographic system.
Three GNSS surveys were carried out to measure ground displacement both in urban and non-urban areas. In the same period, three TLS and SfM surveys were performed to monitor two cracked buildings. Finally, MT-InSAR results integrated with GNSS, topographic, TLS and SfM measurements allowed the relationships between the kinematic evolution of the landslides and damage to the buildings to be investigated.
In detail, the study area was monitored using multi-temporal GNSS data acquired during three different survey campaigns performed in October 2018, June 2019, and October 2019. Measurements were planned identifying 11 points: a GNSS permanent station (SCHI) and two non-permanent stations (NPS) positioned outside, in presumably stable areas, to check the co-registration of the reference system for each survey, and eight NPS are located on stable foundations inside the unstable slope to check and monitor instability phenomena. These points are useful not only for the georeferencing of terrestrial measurements, but also as a source of data for the comparison and validation of interferometry results.
It was adopted the static mode approach at a sampling rate of 15 s in order to carry out the survey of the network foreseeing the minimum acquisition time of 3 h for each baseline. Acquired data were processed using the Infinity software provided by Leica Geosystems, taking into account precise orbits of satellites downloaded from the International GPS Service for Geodynamics (IGS). The network related to the three points outside the unstable area was used to check the stability of the NPS stations in the multi-temporal analysis and to constrain the common reference system for each survey. Subsequently, the adjustment of the network related to the points inside the unstable slope and transformed in the stable reference system, provided the coordinates of the NPS points for each measurement. Finally, the differences in the 3D coordinates provided the displacements of the points along north, east, and elevation directions.
TLS acquisitions were performed using the Leica ScanStation P20. In the surrounding area of the two analyzed buildings, two local topographic networks were defined and measured using the total station Leica TCR1201 for the survey of the targets necessary to align the TLS scans. The local networks are composed by five points in Cappellazzi district and six points in the Rovegliana Church area. Each network includes two GNSS NPS points (1100 and 1200, 2100 and 2200, Figure 38) which were used for georeferencing the point clouds in the UTM32 cartographic reference system.
The total station was used for the measurement of the topographic reference network and the targets and for the survey of natural and artificial points homogeneously distributed on both sides of the main cracks affecting the buildings, performing distances and angular triangulations measurements from the points of the network to evaluate any differential displacement. In addition to the TLS surveys, terrestrial photogrammetric acquisitions were performed for the application of the SfM technique.
The images of the damaged buildings were acquired by the digital single-lens reflex (SLR) camera Canon EOS 5DS. To monitor the evolution of the crack pattern affecting the walls of the buildings, 96 images in Cappellazzi district and 127 images in Rovegliana Church were acquired.

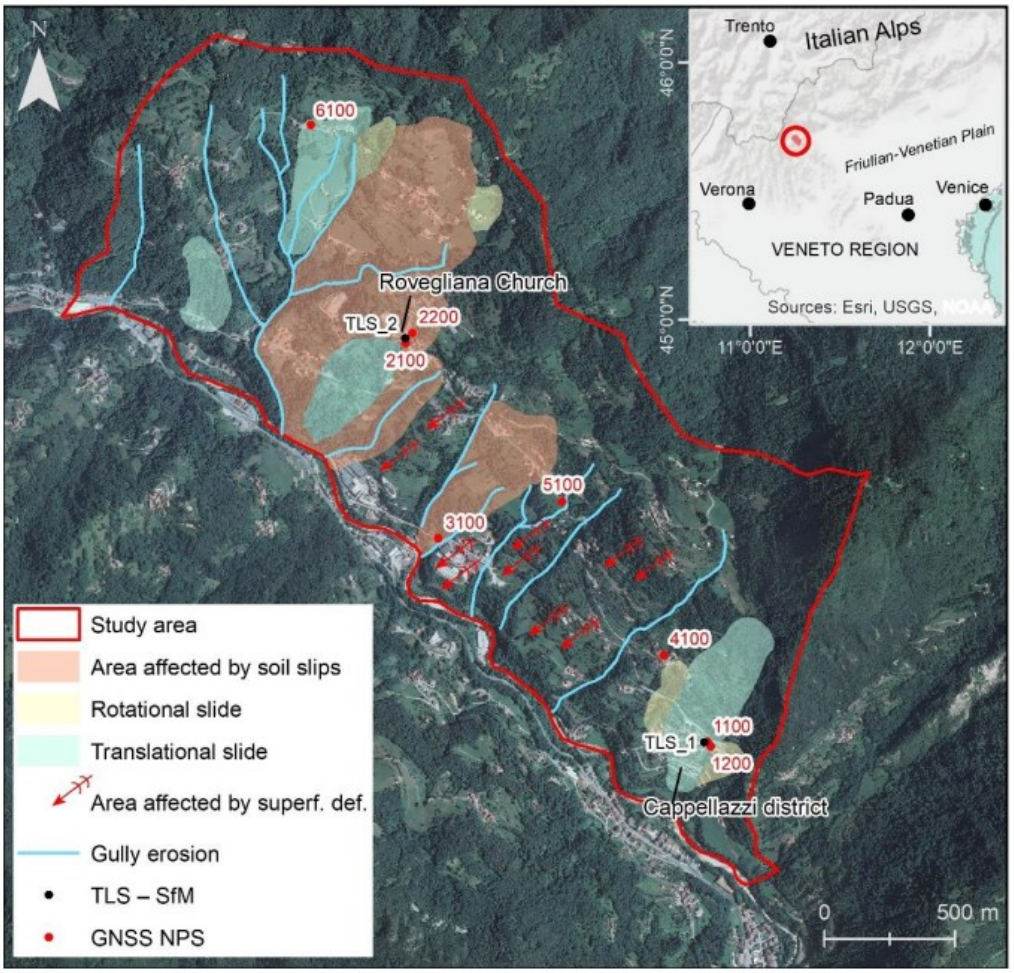

Figure 38: Location of the study area (inset) and map of the instability phenomena. Global navigation satellite system (GNSS), non-permanent stations (NPS) and the location of terrestrial laser scanning and structure for motion surveys (TLS– SfM) are shown [6]

The SfM processing of the images was executed with the purpose to trace the evolution of the fractures in the observation period, thanks to the high-resolution imagery acquired by SLR camera. The reconstruction of a reliable 3D model and the extraction of the orthophotos can be validly used for identifying and tracking the discontinuities.
It was decided to use orthophotos from SfM rather than from TLS textured model because of the far better resolution of the images acquired by SLR camera and the impossibility to distinguish millimetric details in TLS point cloud. By superimposing the traces of the cracks detected in 2018 (red polylines in Figure 39) on the 2019 orthophoto, it shows that the damage on the walls did not increase in the observation period.

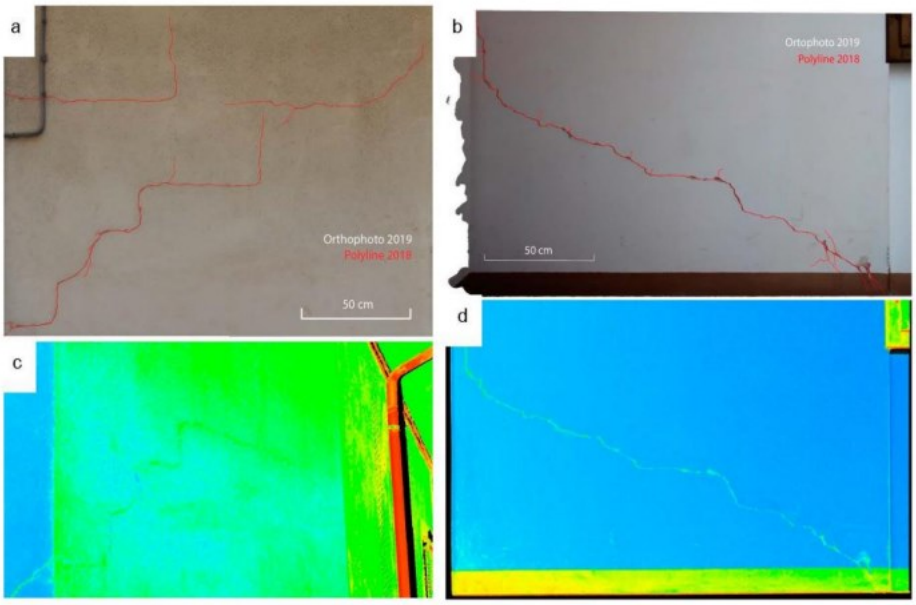

Figure 39: Orthophotos showing the wall of the building in Cappellazzi (a) and the portico of Rovegliana Church (b) in 2019, with superimposed the traces (red polylines) of the cracks detected in 2018. (c,d) are the point clouds derived by TLS for the building and the portico, respectively [6]

RESULTS

LoS, horizontal and vertical displacements affecting the two structures monitored by TLS and SfM were compared to those estimated in the surrounding non-urban areas. The trend of the time series in Cappellazzi is very similar with a total displacement between −8 and −20 mm in the LoS direction (Figure 40b). Total displacement along the horizontal and vertical directions is almost the same and it is between −5 and −10 mm. These results show that the entire sector is moving to SW at the same rate along the maximum slope which is consistent with the kinematic of the translational slide affecting this area. In the case of the Rovegliana Church area, the trend of the time series is similar, but points 2103 and 2104, located at north of the church, have a total displacement higher than points 2101 and 2102. These differences show that this area is affected by two different instability phenomena which have been activated in the same periods but with different intensity as occurred after July 2017 and July 2018 (Figure 40f). The negative trend of horizontal and vertical components (Figure 40g, 40h) suggests that points 2103 and 2104 are moving to west along the maximum slope due to the soil slips occurring in this sector, while points 2101 and 2102 are moving to south–west, according to the local morphology, along the same direction of the translational slide affecting the southern area of Rovegliana Church (Figure 38). Both in Cappellazzi and the Rovegliana Church area, the time series clearly show that displacements occur during the wet seasons, from March to June (Spring) and from September to November (Autumn) (Figure 40b–d,f–h), rainfall being the main triggering factor. Figure 41 shows a clear relationship between rainfall and vertical displacement affecting the area of Rovegliana Church. It has to be noted that after dry winter periods, spring rainfall events cause an upward displacement.

The GNSS processing and the adjustment of the external network composed by 3 points provided the coordinates of the 10 NPS points in the UTM32 cartographic reference system. The three external points showed differences in the coordinates ranging from 0 to 1.0 mm (October 2018–June 2019) and from 0.1 to 1.2 mm (June 2019–October

2019), thus they can be considered stables during the observation period. The network of the NPS located inside the unstable area was adjusted by constraining the coordinates of the 3 stable external points. The results of the adjustment provided coordinates standard deviations ranging from 2 to 6 mm in planimetry and up to 9 mm in elevation. The differences of the coordinates of the 8 inside NPS points generated the 3D displacement vectors.

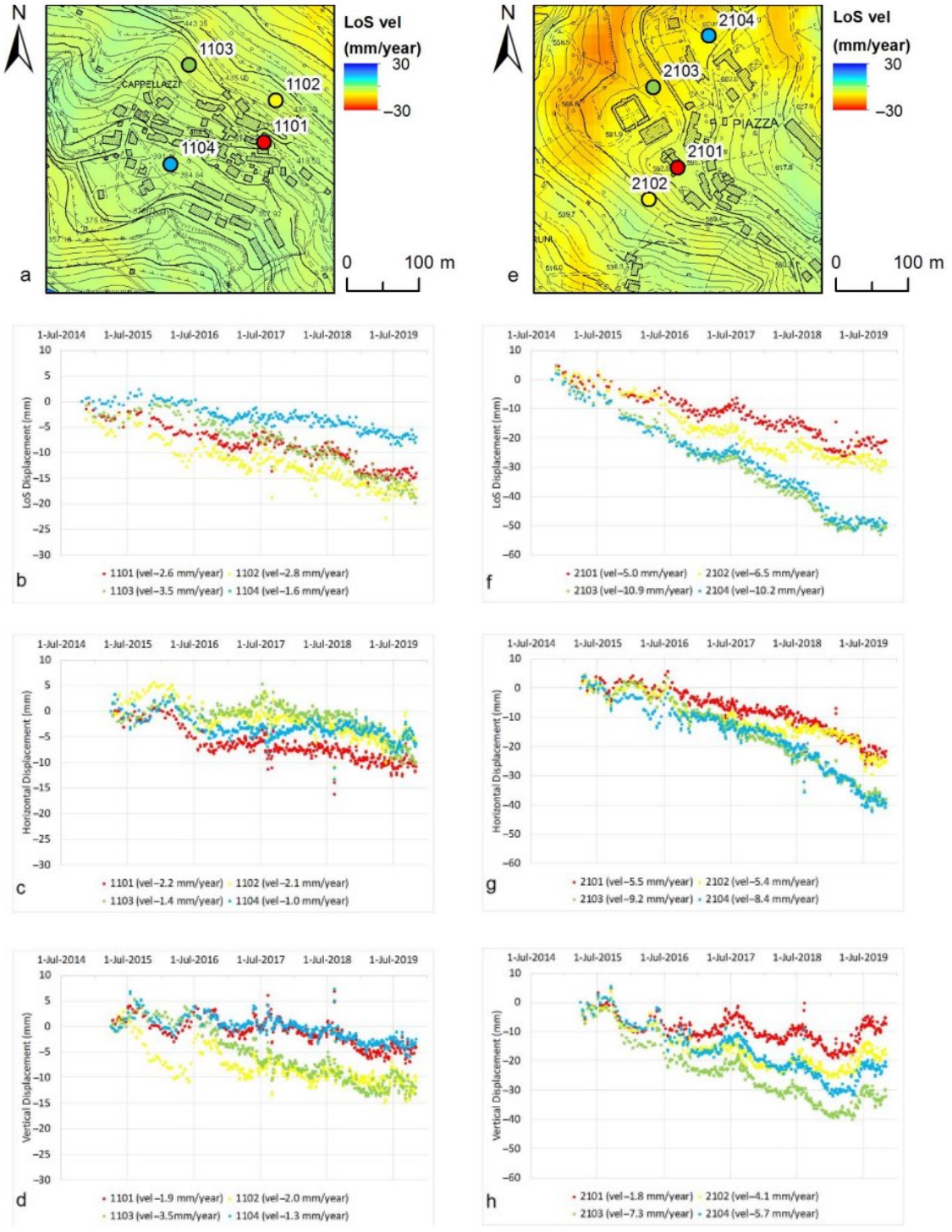

Figure 40: Descending LoS, horizontal and vertical displacement time series of points located at Cappellazzi district (b–d) and Rovegliana Church and its surrounding area (f–h). In (a) and (e) the location of points is shown on the descending LoS velocity maps [6]

Points 1101 and 2101 are located at the damaged building in Cappellazzi and at Rovegliana Church, respectively.

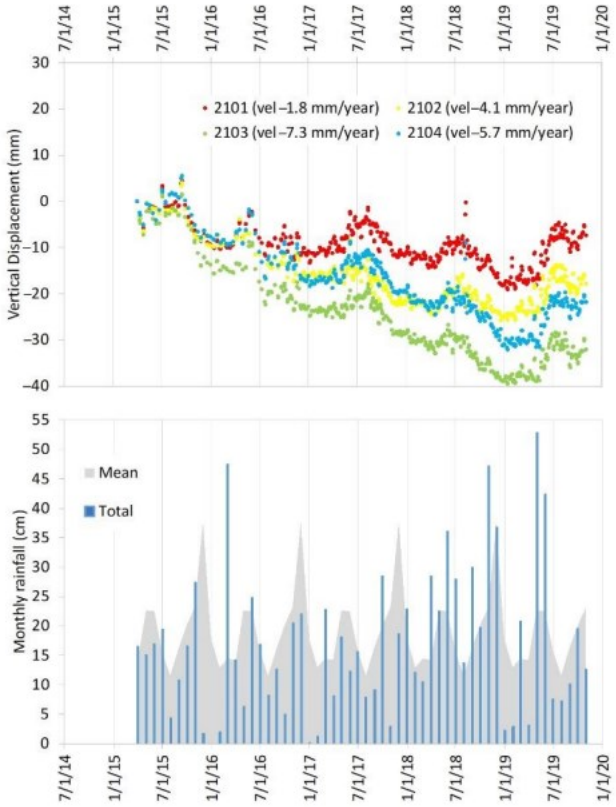

Figure 41: Comparison between vertical displacements estimated in the area of Rovegliana Church (Figure 40h) and monthly rainfall (blue bars). In grey, mean monthly rainfall calculated over the period 1994–2019 is shown [6]

GNSS data provided the 3D deformation vector at each GNSS point, with an accuracy in the order of 10 mm. The GNSS measurements, in agreement with the MT-InSAR results, provide horizontal displacement vectors directed toward the maximum slope.
The 2 NPS points used for monitoring deformations in Cappellazzi district and for georeferencing the topographic, TLS and photogrammetric acquisitions did not show any relative displacements each other.
The comparison between the coordinates of the artificial and natural topographic points located in different portions of the two buildings and separated by significant cracks, do not show relative displacements, indicating that the movements detected by GNSS and InSAR surveys involved the whole structures rigidly. This is confirmed by the multi-temporal TLS scans which did not detect any significant change in the crack pattern. Even the comparison between the images acquired in the first and last SfM surveys do not show any progression of the damages affecting the two structures.
The findings of this study show that the mass movements observed by interferometry during the period October 2018–October 2019 (Figure 40) have caused a rigid movement of the monitored buildings, because no differential deformations of the structures were detected by topographic, TLS and SfM surveys. Therefore, it can be argued that slope instabilities cause the displacement of block of buildings.

4 ANALYSIS

In this chapter I describe step by step what I did with the Qgis programme, with the final aim of analyzing GNSS and SAR data, in order to make comparisons and then draw conclusions about the movement of the landslide area.
Qgis is an open-source GIS (geographic information system) desktop application that allows you to visualize, organize, analyze and represent spatial data. It allows users to analyze and edit spatial information, in addition to composing and exporting graphical maps. Qgis supports raster, vector and mesh layers.
The very first thing done was to upload into Qgis the orthophoto[2] of the Veneto Region (dating back to 2018), obtained by entering the site of the 'Geoportale della Regione Veneto', which provides a series of standard OCG services[3] (in this case a WMTS service).
A very important thing to keep in mind is to work always with the same reference system, when I have to upload maps, coordinates or other data.
A coordinate reference system (CRS) defines how the two-dimensional projected map in your GIS relates to real places on the earth. The decision of which map projection and CRS to use depends on the regional extent of the area you want to work in, on the analysis you want to do, and often on the availability of data.
The reference system used was the WGS84 / UTM32 (EPSG:32632).
To determine the area of the landslide, inside the orthophoto, I uploaded points with EAST and NORTH coordinates (taken from a photogrammetric flight of 2005) into Qgis using the command *Layer-aggiungi layer- aggiungi layer testo delimitato* (*fig. 42*)
Then, to obtain a line, that delimits the area in question, I went to *Processing-Strumenti-Da punti a linea (fig. 43).*

[2] An orthophoto is an aerial image that has been geometrically corrected (ortho rectified) so that the image is uniform from edge to edge. The goal of ortho rectification is to create an image where distance measurements are the same across the entire image. Orthophotos are corrected to remove terrain effects and distortions that result from the camera's lens and from the angle of the photo taken from the plane.
[3] OGC (Open Geospatial Consortium) web service defines several types of services for serving different kinds of data and maps.

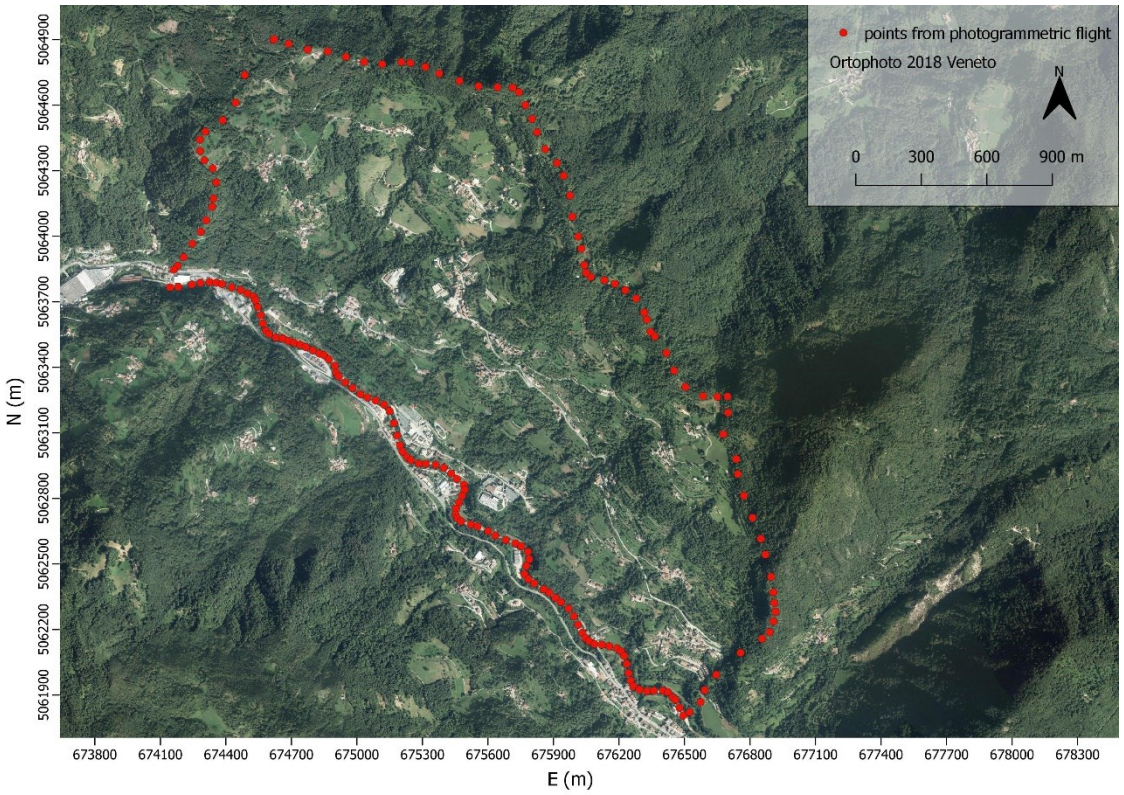

Figure 42: Landslide area delimited by points [author]

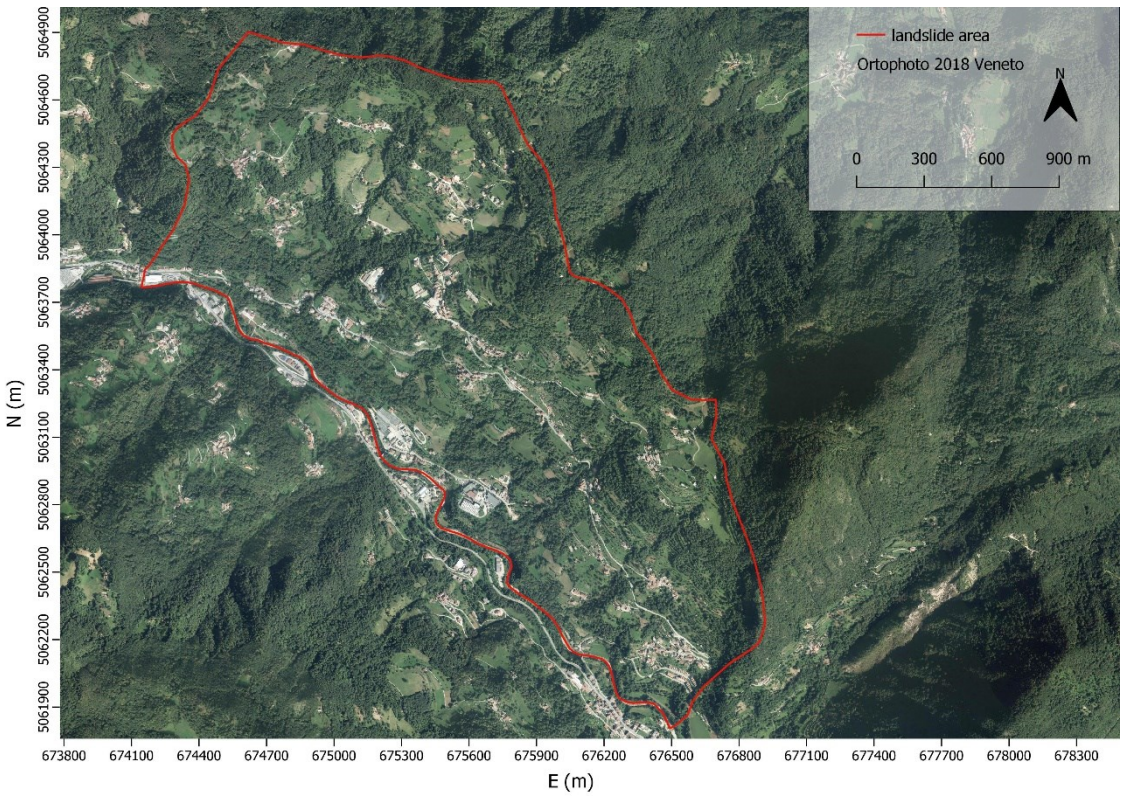

Figure 43: Landslide area delimited by a continuous line [author]

As written in chapter 4.3, the first of the several campaigns was carried out the 23th October 2018. The area was studied using GNSS and identifying 10 reliable non-permanent stations, among which 2 are positioned in a presumably stable area outside the landslide, and 8 NPS are located inside the unstable slope.
The eight points have the coordinates presents in table 6.
I then entered the coordinates of these 8 points, which I first copied into an Excel file, inside the landslide area, using the command *Layer-Aggiungi layer- Aggiugi layer testo delimitato.*
The results of this step are shown in figure 44.

ID	EST [m]	NORD [m]	H geo. [m]
1000	673241.271	5063625.394	441.143
2000	676868.605	5060459.273	333.691
1100	676597.375	5062141.131	416.621
1200	676609.853	5062125.402	418.382
2100	675442.713	5063664.481	591.594
2200	675468.155	5063701.565	593.807
3100	675568.359	5062918.721	404.338
4100	676432.232	5062472.327	496.906
5100	676042.509	5063058.517	525.240
6100	675080.534	5064495.675	659.256

Table 6: planar coordinates measured in 2018 [2]

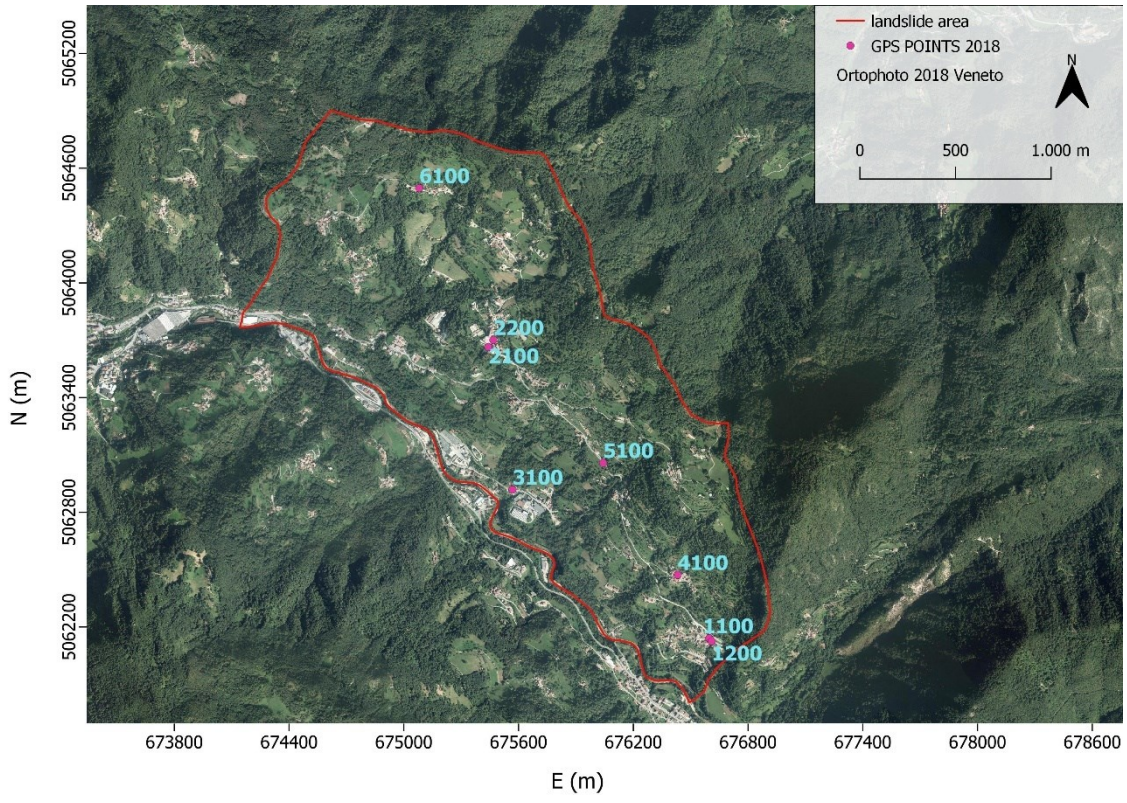

Figure 44: GNSS points [author]

In the next step, I georeferenced an orthophoto i.e., a raster image. Georeferencing is crucial to make aerial and satellite imagery useful to calculate distances and areas and for mapping, as it explains how other data, such as the above GNSS points, relate to the imagery. A georeferenced orthophoto is scaled correctly and is also oriented (so the North of the photo correspond to the real North).
To georeference the image I went to the *toolbar-raster-georeferencer* and insert the jpg image, shown in figure 38.
The minimum number of points to georeference is 4, but for greater precision I used all 8 GNSS points. In general, to reduce the error, it is better that the chosen points are well distributed among them, e.g., not all close together.
You can georeference in two ways: by entering the coordinates of known points or by choosing the points visible in the image and associating them with the actual points in the orthophoto of the landslide (fig 44), e.g., by choosing house edges visible in both images.
Given the low quality of the source image to be georeferenced, it was difficult to clearly distinguish the edges once the image was zoomed in, so I opted for the first of the two methods.
I clicked on the various GNSS points in the loaded image and entered the actual coordinates of those GNSS points, i.e., those in table n.6
Qgis materializes red dots with which are associated position information within a two-dimensional Cartesian reference system, where the unit of measurement is the pixel.
Now I have to set the parameters and manage the computational environment. I went to *impostazioni di trasformazione* (yellow gear) and chose a first-degree polynomial transformation, then as a resampling method I used the nearest neighbor method and finally entered the reference system EPSG:32632[4].
The software recalculates the pixel positions according to the coordinates of the points and for each point calculates the residual error in terms of pixels.
Now I launch the georeference and then load the image into Qgis by clicking *on layer-add layer-add raster layer.*
The result of this georeferentiation is shown in Figure 45.
This last step was done in order to be able to extract the different landslide areas (those with different colors) in the figure 38 and report them in the orthophoto of Veneto.
To create these polygons, I clicked on *nuovo layer shape file* and set polygon as the geometry type and WGS84-32N as reference system.
I then clicked on the yellow pencil symbol and on *add polygon element*, and so plotted the various polygons, obtaining the result shown in the figure 46.
The reason for this will be explained later.

[4] EPSG Geodetic Parameter Dataset is a public registry of geodetic datums, spatial reference systems, Earth ellipsoids, coordinate transformations and related units of measurement. Originally created by European Petroleum Survey Group (EPSG). Most geographic information systems (GIS) and GIS libraries use EPSG codes as Spatial Reference System Identifiers (SRIDs) and EPSG definition data for identifying coordinate reference systems, projections, and performing transformations between these systems. EPSG: 32632 refers to WGS 84 / UTM32.

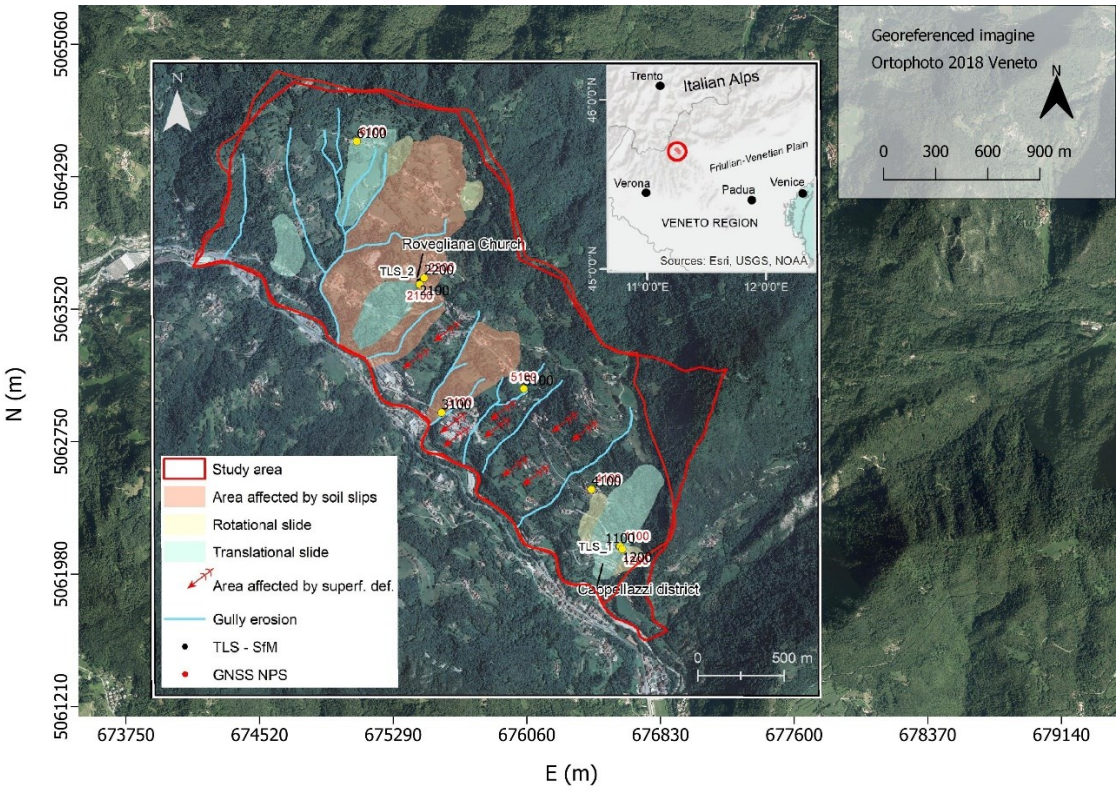

Figure 45: georeferentiation of the orthophoto [author]

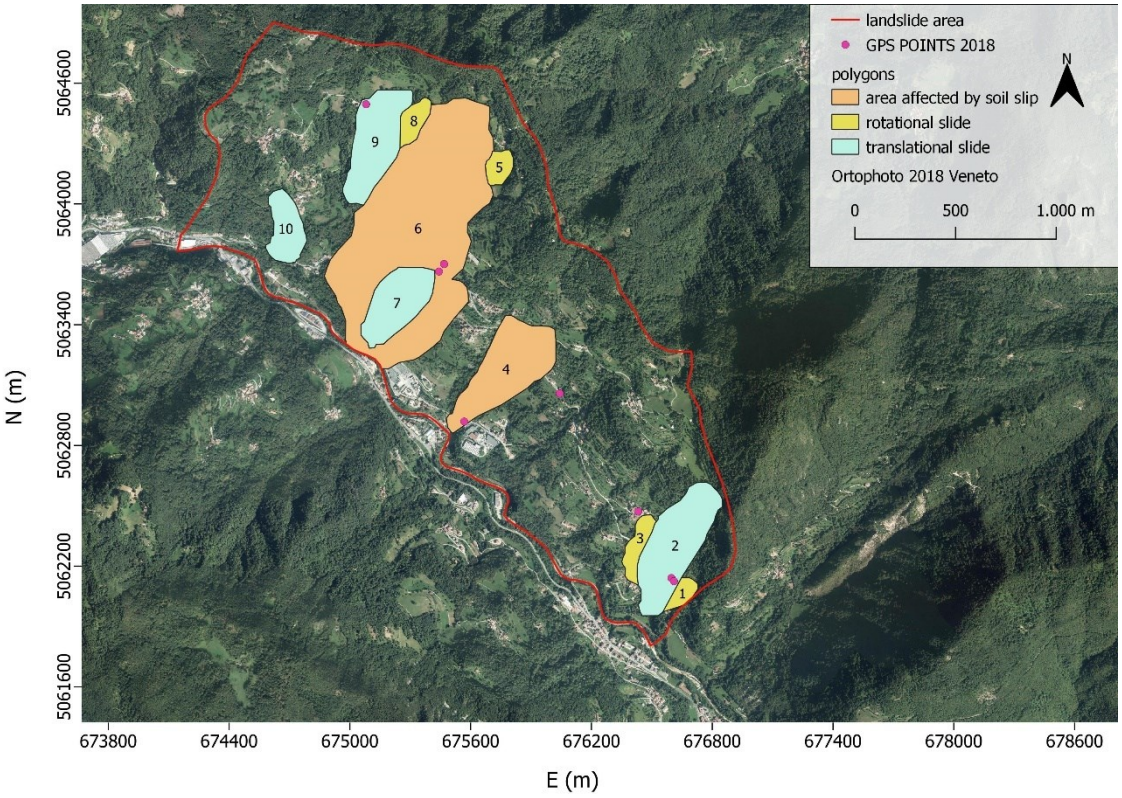

Figure 46: polygons representing different landslide areas [author]

To get an idea of how the landslide moved at the eight monitored points, a fifth measurement campaign was carried out in June 2021, and the differences in coordinates E, N, H are shown in table n.7.

	JUN/21 - OCT/18 [m]		
ID	N5-N1	E5-E1	H5-H1
1100	-0,019	-0,014	-0,013
1200	-0,009	-0,007	-0,004
2100	-0,016	-0,020	-0,015
2200	-0,019	-0,026	-0,004
3100	-0,009	-0,006	0,008
4100	-0,022	-0,006	-0,010
5100	-0,009	-0,013	0,007
6100	-0,018	-0,013	0,006

Table n. 7: differences in coordinates from October 18 to June 21 [author]

As mentioned earlier, since the purpose is to compare the validity of SAR points with respect to points measured with GNSS, I need to have the displacements in mm/year.
I therefore transformed the differences from meters to millimeters and then divided them by the years elapsed between the two measurements i.e., 2.67 years. The result is shown in table n.8.

	VELOCITY JUN/21 - OCT/18 [mm/year]		
ID	N5-N1	E5-E1	H5-H1
1100	-6,909	-5,091	-4,727
1200	-3,273	-2,545	-1,455
2100	-5,818	-7,273	-5,455
2200	-6,909	-9,455	-1,455
3100	-3,273	-2,182	2,909
4100	-8,000	-2,182	-3,636
5100	-3,273	-4,727	2,545
6100	-6,545	-4,727	2,182

Table n. 8: differences in mm/year from October 2018 to June 2021 [author]

These data are used to create velocity vectors in each of the 8 points of the landslide. In order to create these vectors, I used a command already present in Qgis, called *edit vector field settings for current layer.* The result is shown in the figure below.
The aim is now to check if these vectors are perpendicular to the contour lines of the area. Contour lines are imaginary line that connects points of equal elevation (fig. 48). The contour interval is the distance between different lines and the interval depend on terrain and purpose of the survey map. Contour lines close together indicate a steep slope, while contour far apart indicate gentle slope. They are always perpendicular to the direction of the maximum slope; that is why soil movement (as well as water flow) is always perpendicular to contour lines.
From figure 49 to figure 54 we can actually check and confirm that the deformation vectors created are correct, since they have expected directions and lead the system towards the condition of minimum potential energy.

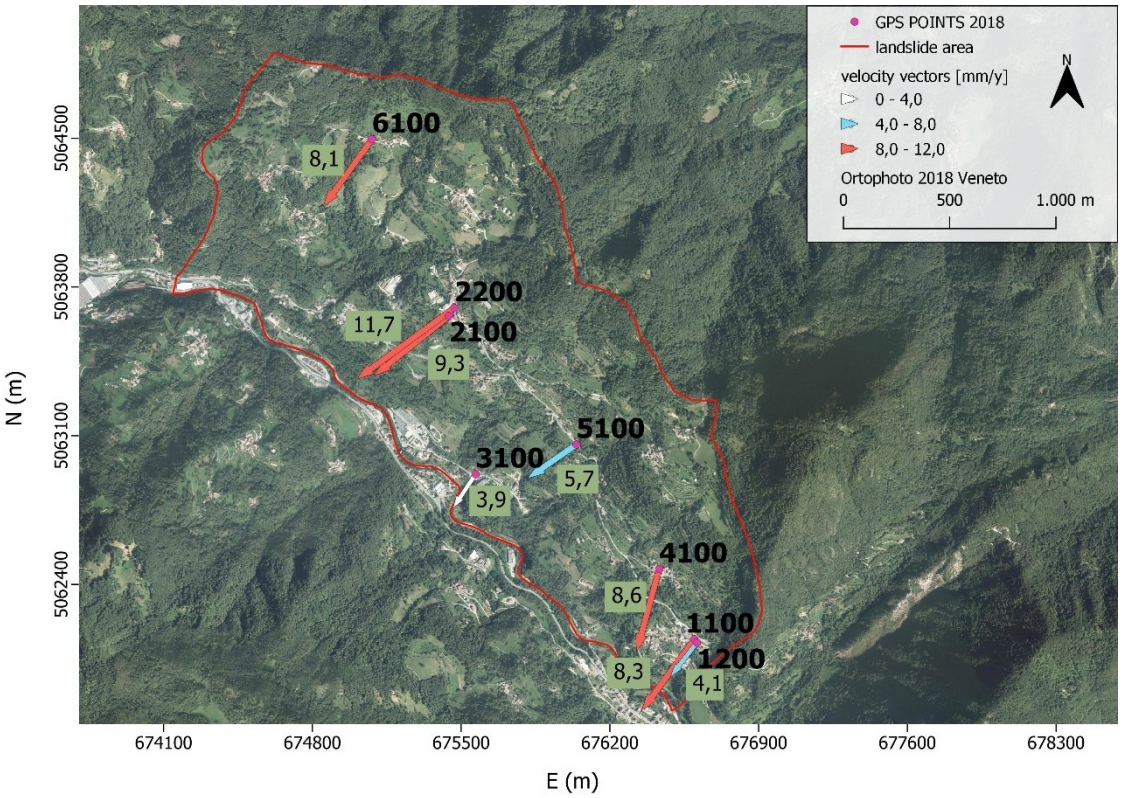

Figure 47: velocity vectors [author]

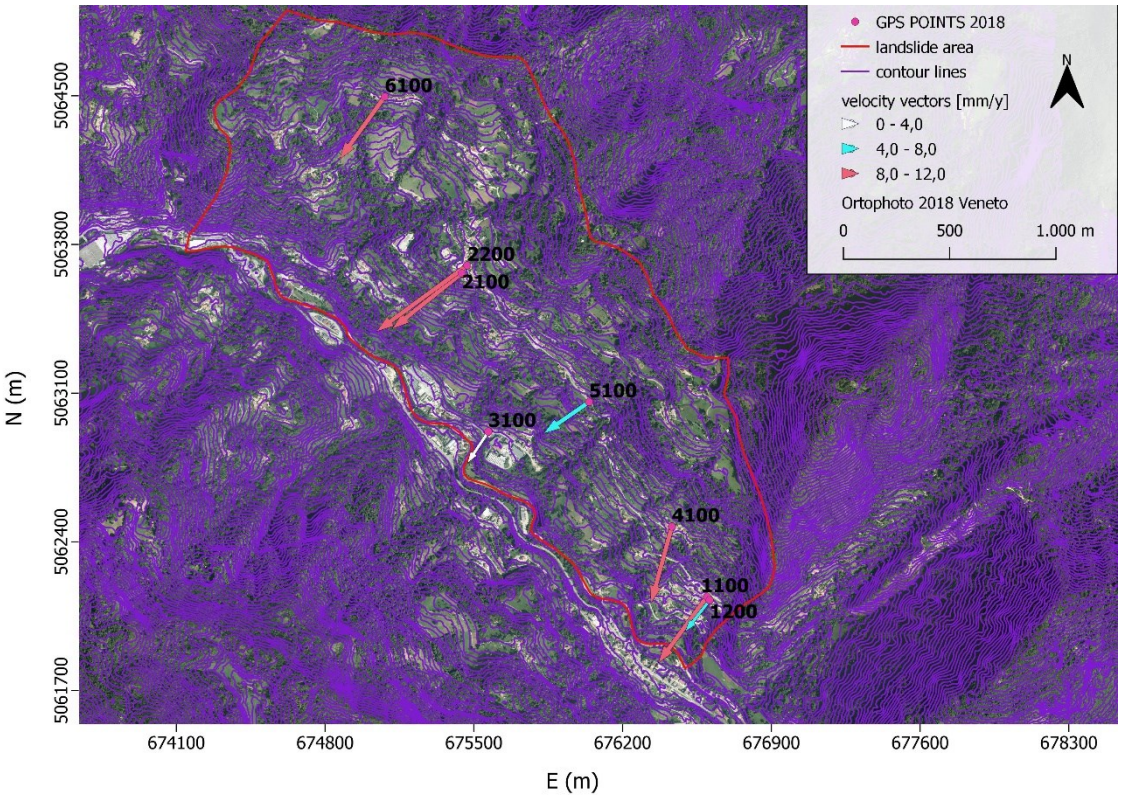

Figure 48: contour lines [author]

For the points 6100, 5100, 3100, 1100 and 1200 it is easy to verify the orthogonality, while for points 3100, 4100, 2100 and 2200 is not so immediate. This is because the contour lines were extracted from a DSM of 2005. A DSM is a digital surface model, that capture both environment's natural and artificial features and what we see is the top visible surface. For this reason, if the contours have to represent lines that connect point of equal elevation, they take into account also the height of trees and buildings, distorting the true elevation of the terrain.
For example, for point 3100 in figure 50, the presence of those buildings distorts the contour lines.

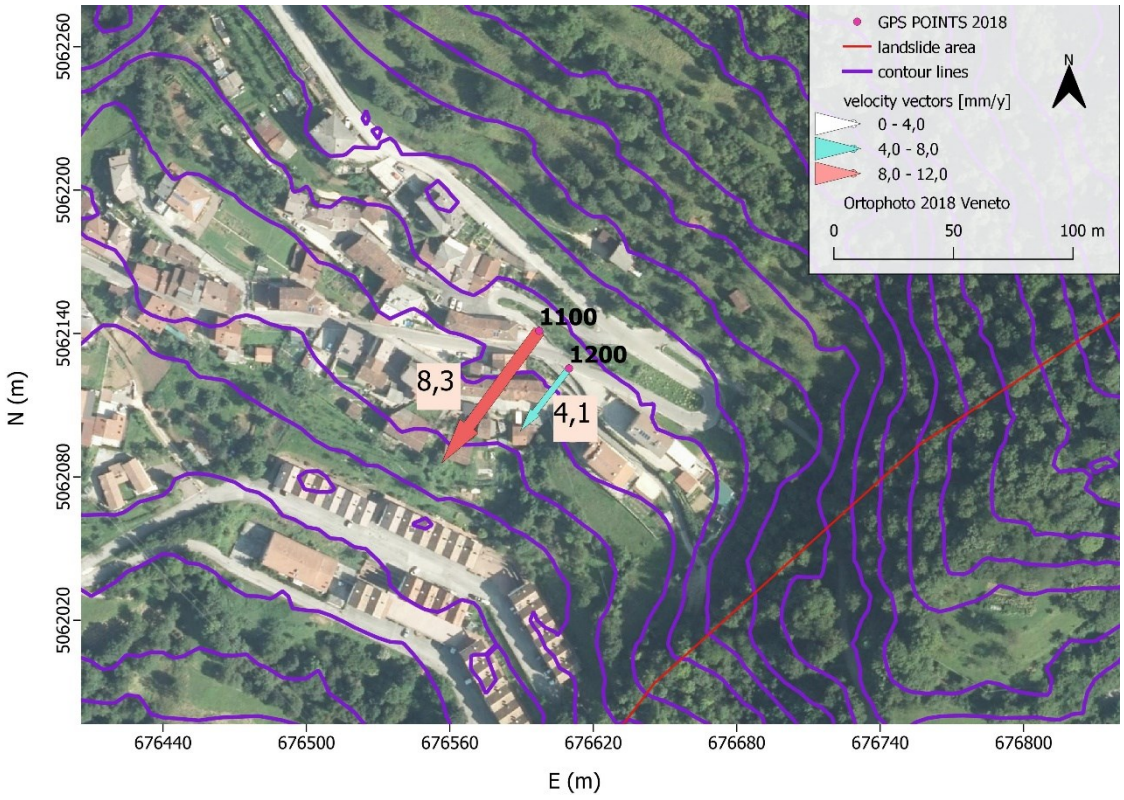

Figure 49: contour lines and velocity vectors in points 1100 and 1200 [author]

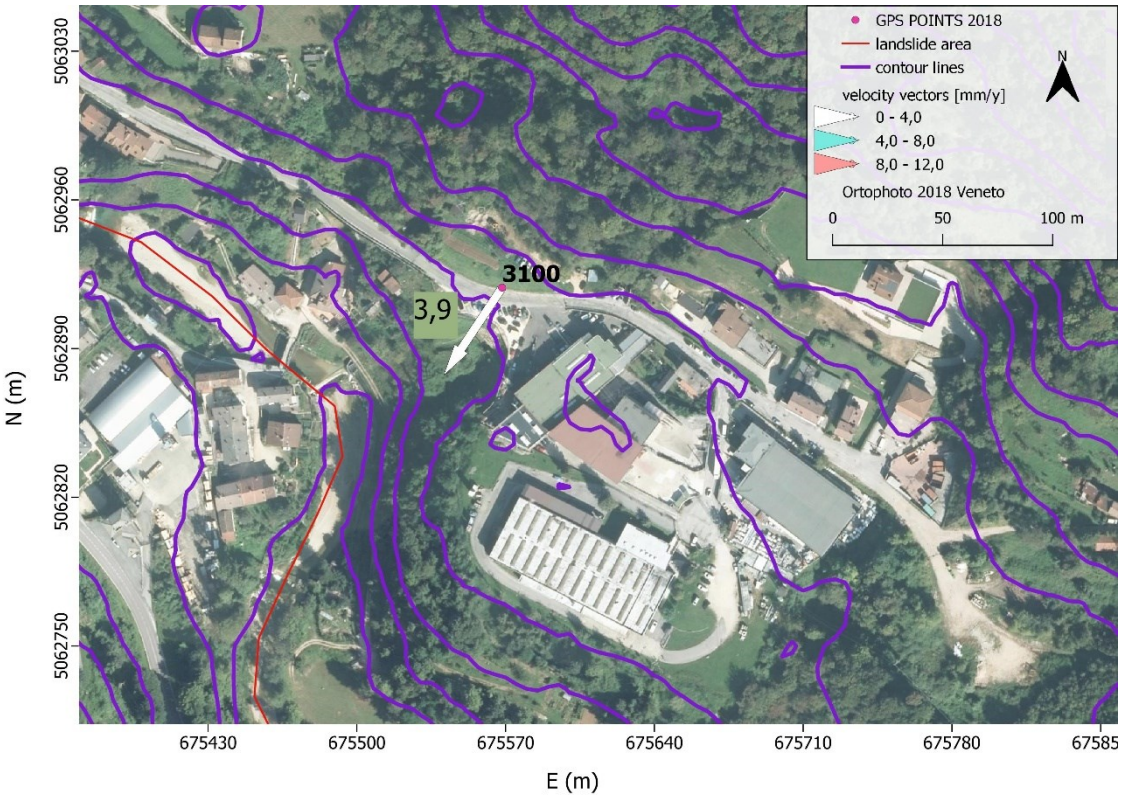

Figure 50: contour lines and velocity vector in point 3100 [author]

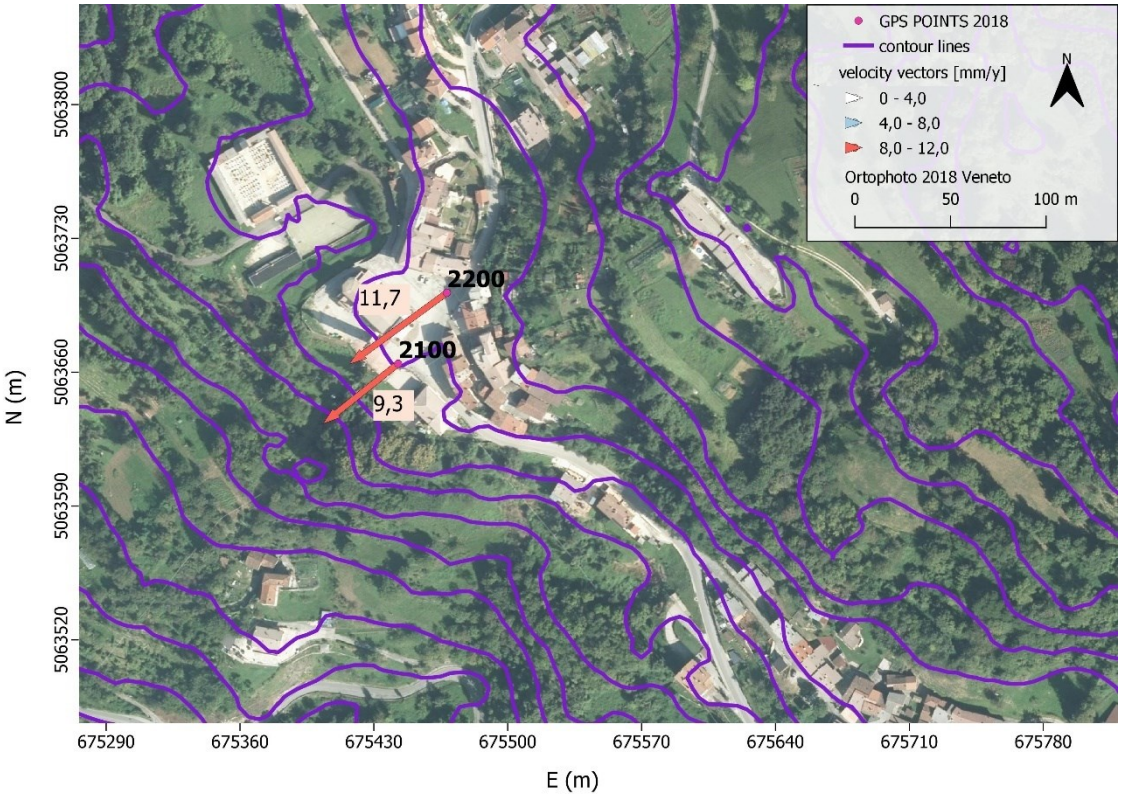

Figure 51: contour lines and velocity vectors in points 2100 and 2200 [author]

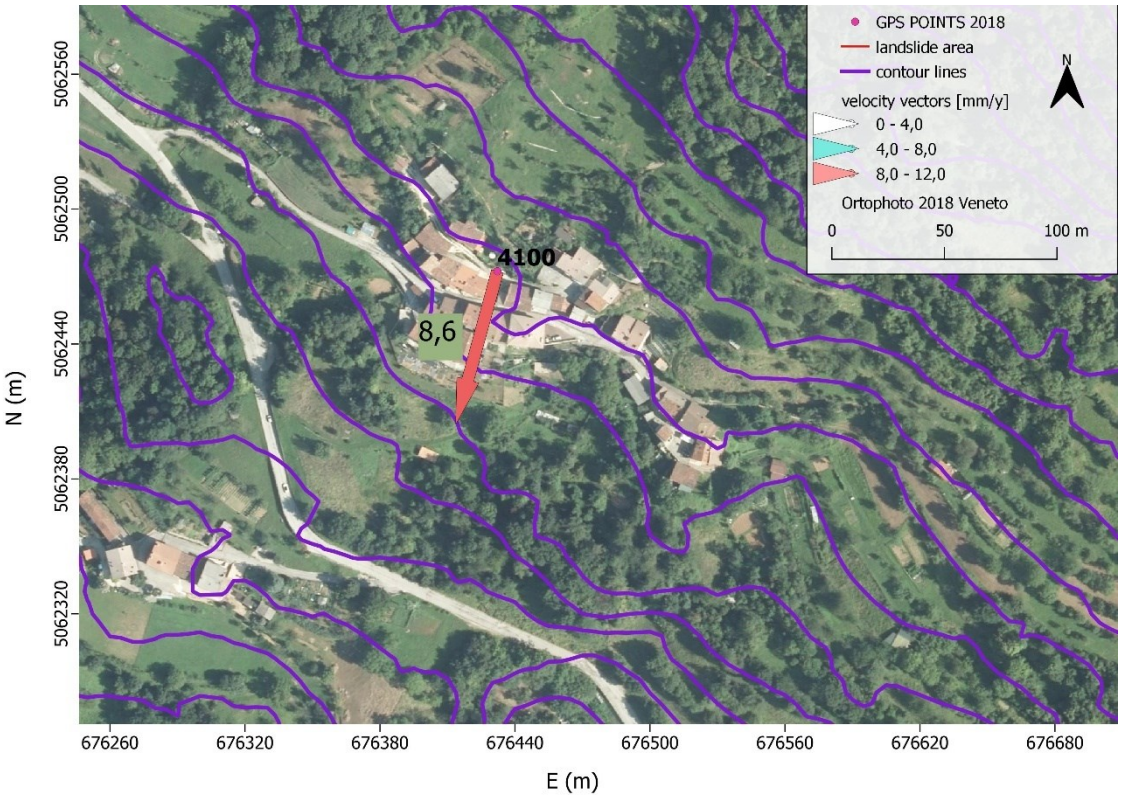

Figure 52: contour lines and velocity vector in point 4100 [author]

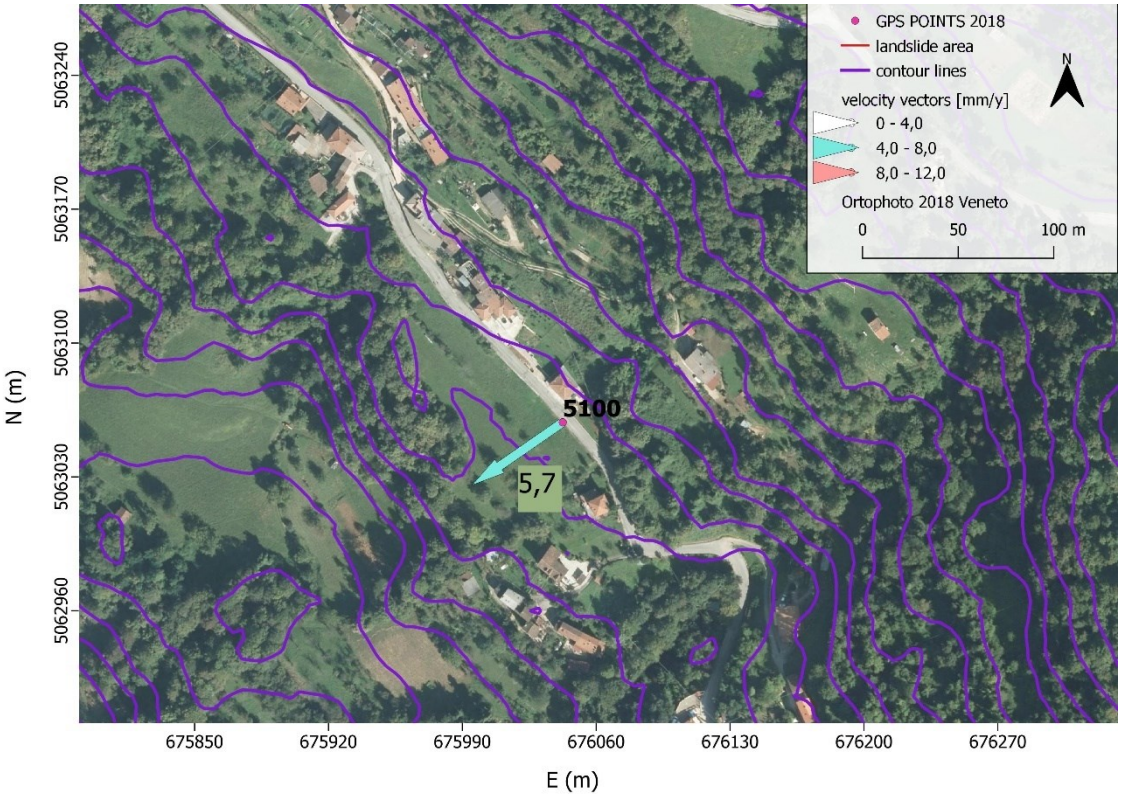

Figure 53: contour lines and velocity vector in point 5100 [author]

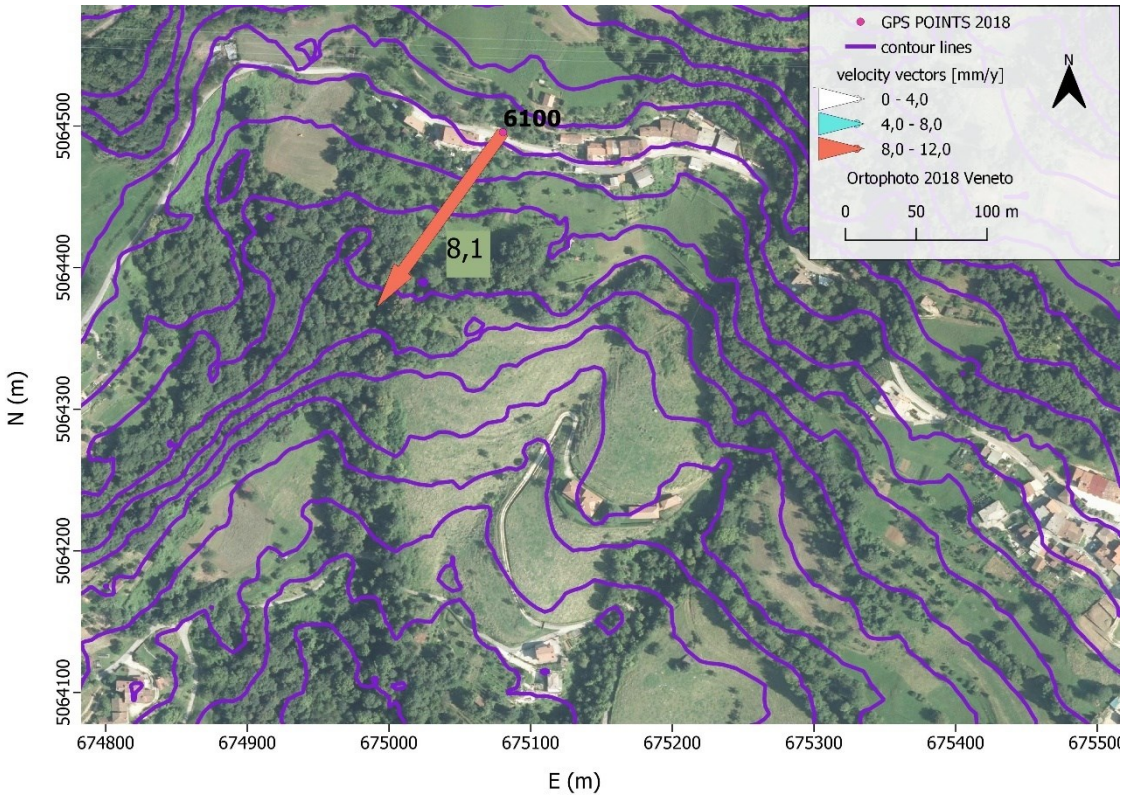

Figure 54: contour lines and velocity vector in point 6100 [author]

The following operation was the input in Qgis of the SAR data, both horizontal and vertical.
These data were obtained using the Sentinel 1A-B with SBAS technique (view chapter 2.1) from 2014 to 2019. This time coverage is different from the GNSS, that acquired data from 2018 to 2022. I can use in any case the SAR to do the comparison with GNSS because previous studies have shown that deformations in Rovegliana area are linear in time and therefore I can also use past SAR data.
The file that I used contains information regarding the latitude and longitude of the points, respect to the ellipsoid WGS84, and the horizontal and vertical velocities of the points, expressed in mm/year.
To enter this file into the open source, I clicked on *layer - aggiungi layer testo delimitato.*
Qgis automatically project the geographic coordinates (latitude and longitude) into cartographic coordinates, using a transformation in 7 parameters. My reference system is always UTM32.
After this operation, I just see a lot of points inside my landslide area. Each point is associated with coordinates and velocity values.
To have a better understanding of how the landslide move, in which direction and with which intensity, I categorized the different speeds with different colors.
In figure 55 are shown horizontal velocities. Positive values mean that the landslide is moving from west to east, while negative values mean from east to west. Darker colors, like dark blue or red, indicate that the movements of the points are high.

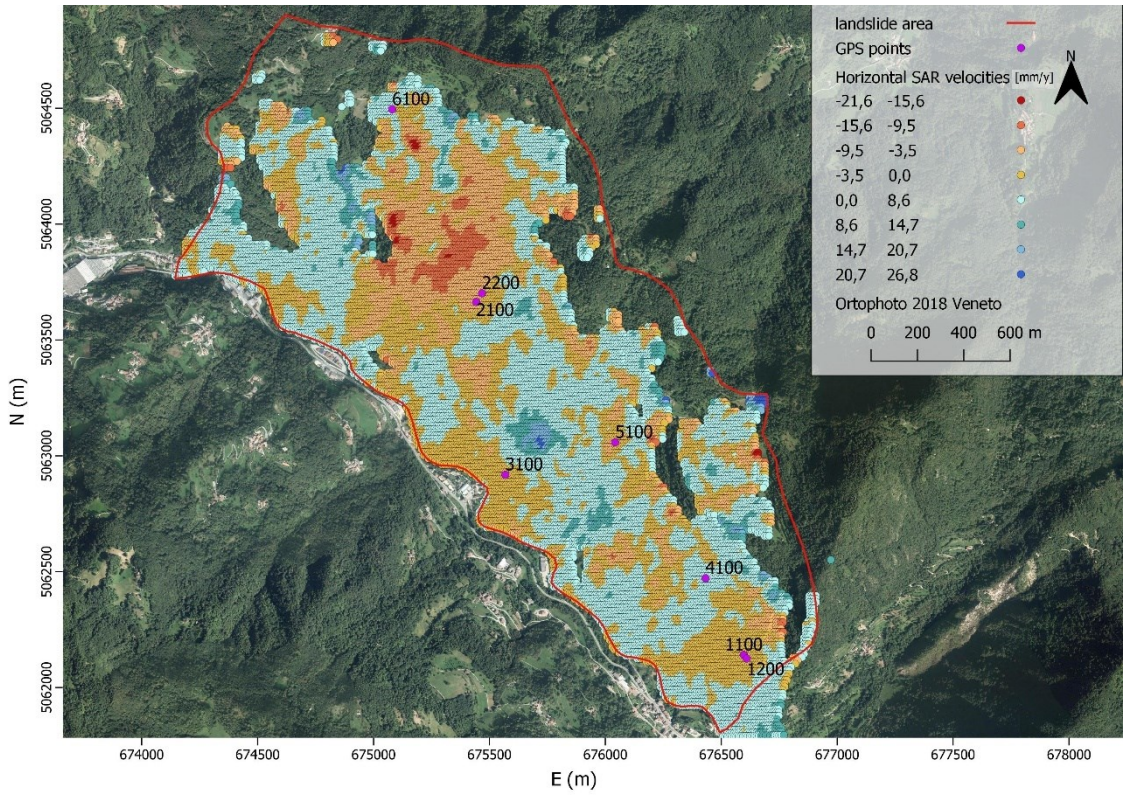

Figure 55: horizontal SAR velocities [author]

In the figure 56 are shown vertical velocities. Due to the fact that a landslide can only move downwards, all the points should be colored in blue (from light to dark blue).
Almost all of them have negative movements (as expected). The reason for which we have some red spots, is not because of an upward movement of the soil, but is because we have some errors in the measurement, for example due to the vegetation. Or another hypothesis could be an accumulation of the soil at the base of the landslide. We have to remind that the SAR technique requires target with good reflectivity for its signal to reflect, and the presence of trees is therefore a problem.
What I did next was to cut out the SAR points present inside the different polygons I created before (see figure 46). To do that I used the command *vettore – strumenti di geoprocessing – ritaglia;* as imput layer I put the SAR data and as output layer I put the desired polygon.
I repeated the same operation with all the ten polygons, using both horizontal and vertical points. What I obtained is shown is figure 57. The result is the same for vertical and horizontal SAR data.
This step was done in order to determine the mean and standard deviation of the velocities of the points in each polygon.
To obtain this information I used the command *visualizza – statistiche di sintesi* and then select the polygon I am interested in.
I extracted all means and standard deviations of all polygon using horizontal and vertical data, and I put all results in tables 9.

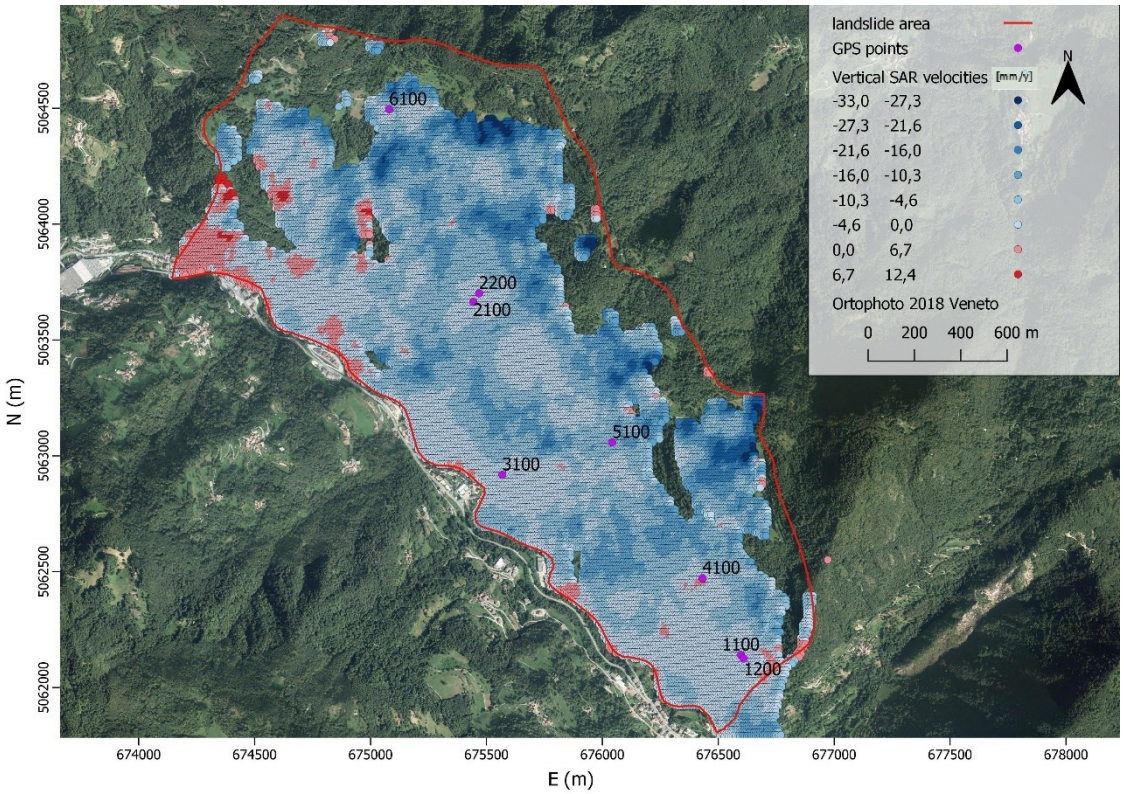

Figure 56: vertical SAR velocities [author]

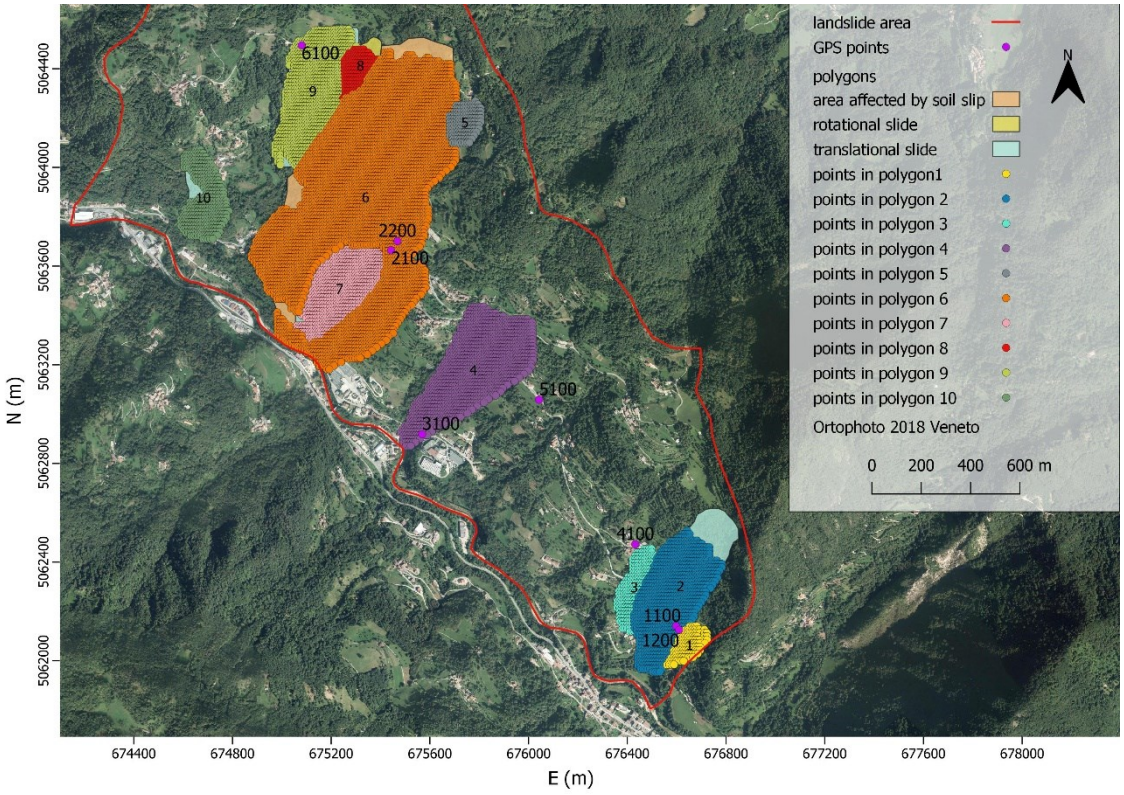

Figure 57: SAR points inside each polygon [author]

HORIZONTAL SAR DATA		
Polygon	Mean [mm/y]	Standard deviation
1	0,052	1,685
2	-0,307	3,835
3	0,633	1,511
4	4,232	5,506
5	0,383	3,000
6	-3,477	4,958
7	-1,903	3,065
8	5,413	5,292
9	-1,760	4,670
10	1,541	3,858

VERTICAL SAR DATA		
Polygon	Mean [mm/y]	Standard deviation
1	-1,183	0,883
2	-4,861	4,022
3	-2,291	1,141
4	-6,853	3,836
5	-9,478	3,177
6	-8,689	5,540
7	-7,772	3,859
8	-13,225	4,741
9	-9,693	6,333
10	-2,317	2,931

Table n.9: in the left, horizontal SAR data of the polygons. In the right, vertical SAR data of the polygons [author]

From the table in the left we can say that, for example, the area of soil present inside polygon 4 moves on average from west to east, while area in polygon 6 moves on average from east to west.
Actually, the landslide should move from east to west: this direction is given by the contour lines (figure 48), that always tell us the true direction.
I can observe from the table in the right that mean values are all negative, as expected (landslide moves downwards).
The following step was to create circular areas of different radius around each GNSS point and then cut out the SAR points inside each circle, like I did with polygons. The reason for this is compare the velocity of the GNSS point with the mean velocity of the SAR data inside each circle around the point, with the aim of the integration of the two datasets. Is important to keep in mind that the Satellites don't allow us to know the displacement along north-south, so we have to take into account only the x-component of the velocity of the GNSS points, in order to make a comparison.
A comparison between the vertical velocities was also carried out.
To create the circles, I used the command *vettore - strumenti di geoprocessing – buffer*, then as input I put the GNSS points and I created 5 different circles with radius 10, 20, 30, 40 and 50 meters around each point.

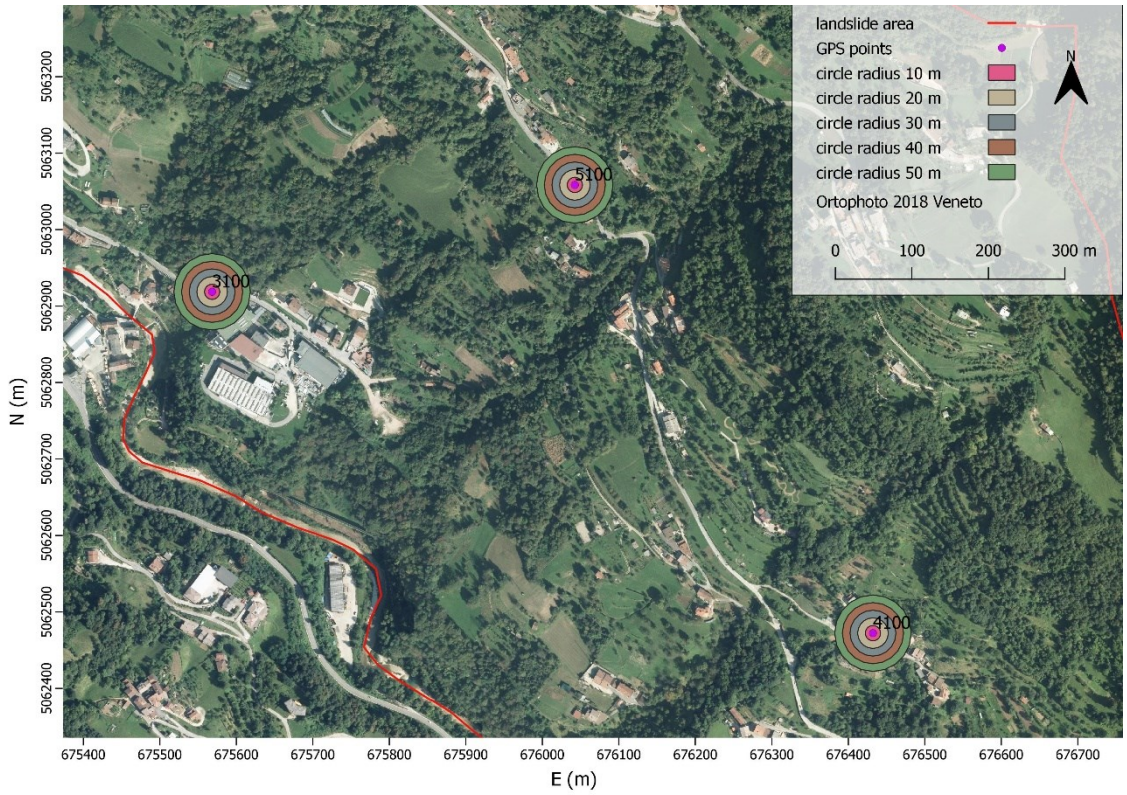

Figure 58: circles of different radius around some points [author]

To cut out the SAR points inside each circle of each point, I did the same procedure explained with the polygons. The procedure was carried out twice, using both vertical and horizontal data.
Using the command *visualizza – statistiche di sintesi* I obtained the number of SAR points inside each circle, the mean velocity and the standard deviation.
In table 11 are present data regarding horizontal mean velocities of the SAR, that are compared with the X-coordinate of the velocity vectors in the GNSS points (see table n.8, E5-E1) to obtain the difference between the two.
In table 10 we are comparing the vertical mean velocities of SAR with the vertical coordinate of the velocity vectors (see table n.8, H5-H1).
In the last thing done, I made use of the SAR data to verify that two buildings affected by mass movements and by significant cracks, where moving rigidly with the landslide.
The two masonry structures I am referring to are those mentioned in chapter 3.3: Rovegliana Church and a building located in Cappellazzi district (see Figure 37 and 38).
To do that, I considered those points above or near them and checked if the horizontal/vertical velocities were similar or not.
Figure 59 represents the house in Cappellazzi district while figure 60 shows the Church.

ID POINT	RADIUS [m]	INSIDE POINTS	MEAN SAR VELOCITY [mm/y]	STANDARD DEVIATION	GNSS Z-VELOCITY [mm/y]	DIFFERENCE Between two velocities
1100	10	2	-1,836	0,060	-4,727	2,891
1100	20	9	-1,787	0,328	-4,727	2,940
1100	30	21	-1,834	0,497	-4,727	2,893
1100	40	37	-1,689	0,622	-4,727	3,038
1100	50	57	-1,584	0,779	-4,727	3,143
1200	10	2	-1,250	0,065	-1,455	0,205
1200	20	10	-1,369	0,389	-1,455	0,086
1200	30	22	-1,255	0,566	-1,455	0,200
1200	40	36	-1,255	0,577	-1,455	0,200
1200	50	58	-1,292	0,735	-1,455	0,163
2100	10	2	-1,476	0,001	-5,455	3,979
2100	20	9	-1,553	0,151	-5,455	3,902
2100	30	19	-1,726	0,361	-5,455	3,729
2100	40	36	-2,002	0,623	-5,455	3,453
2100	50	58	-2,256	0,783	-5,455	3,199
2200	10	2	-2,065	0,134	-1,455	-0,610
2200	20	9	-2,117	0,322	-1,455	-0,662
2200	30	19	-2,152	0,493	-1,455	-0,697
2200	40	35	-2,326	0,696	-1,455	-0,871
2200	50	58	-2,578	0,849	-1,455	-1,123
3100	10	2	-2,879	0,443	2,909	-5,788
3100	20	9	-2,706	0,776	2,909	-5,615
3100	30	20	-2,687	0,929	2,909	-5,596
3100	40	38	-2,758	0,950	2,909	-5,667
3100	50	57	-2,764	0,979	2,909	-5,673
4100	10	3	-0,386	0,495	-3,636	3,250
4100	20	8	-0,732	0,653	-3,636	2,904
4100	30	21	-1,024	1,237	-3,636	2,612
4100	40	37	-1,315	1,479	-3,636	2,321
4100	50	55	-1,486	1,593	-3,636	2,150
5100	10	2	-5,184	0,230	2,545	-7,729
5100	20	8	-5,718	0,634	2,545	-8,263
5100	30	20	-6,013	0,763	2,545	-8,558
5100	40	38	-6,522	1,002	2,545	-9,067
5100	50	56	-6,998	1,515	2,545	-9,543
6100	10	2	-5,591	0,124	2,182	-7,773
6100	20	10	-5,113	1,241	2,182	-7,295
6100	30	21	-4,770	1,498	2,182	-6,952
6100	40	36	-5,395	2,507	2,182	-7,577
6100	50	57	-6,303	3,746	2,182	-8,485

Table n.10: vertical SAR and GNNS data (GNSS from 5th campaign) [author]

ID POINT	RADIUS [m]	INSIDE POINTS	MEAN SAR VELOCITY [mm/y]	STANDARD DEVIATION	GNSS X-VELOCITY [mm/y]	DIFFERENCE Between two velocities
1100	10	2	-2,004	0,038	-5,091	3,087
1100	20	9	-1,990	0,170	-5,091	3,101
1100	30	21	-1,993	0,271	-5,091	3,098
1100	40	37	-2,011	0,336	-5,091	3,080
1100	50	57	-2,016	0,378	-5,091	3,075
1200	10	2	-1,716	0,102	-2,545	0,830
1200	20	10	-1,657	0,310	-2,545	0,890
1200	30	22	-1,692	0,353	-2,545	0,850
1200	40	36	-1,745	0,420	-2,545	0,800
1200	50	58	-1,817	0,497	-2,545	0,730
2100	10	2	-4,232	0,104	-7,273	3,041
2100	20	9	-4,416	0,436	-7,273	2,857
2100	30	19	-4,629	0,744	-7,273	2,644
2100	40	36	-4,703	1,060	-7,273	2,570
2100	50	58	-4,670	1,258	-7,273	2,603
2200	10	2	-3,949	0,121	-9,455	5,506
2200	20	9	-3,931	0,311	-9,455	5,524
2200	30	19	-3,898	0,448	-9,455	5,557
2200	40	35	-4,056	0,700	-9,455	5,399
2200	50	58	-4,221	1,071	-9,455	5,234
3100	10	2	-2,558	0,148	-2,182	-0,376
3100	20	9	-2,282	0,497	-2,182	-0,100
3100	30	20	-1,995	0,648	-2,182	0,187
3100	40	38	-1,784	0,799	-2,182	0,398
3100	50	57	-1,675	0,872	-2,182	0,507
4100	10	3	0,741	0,303	-2,182	2,923
4100	20	8	0,874	0,288	-2,182	3,056
4100	30	21	0,909	0,587	-2,182	3,091
4100	40	37	0,992	0,727	-2,182	3,174
4100	50	55	0,961	0,734	-2,182	3,143
5100	10	2	-2,371	0,508	-4,727	2,356
5100	20	8	-2,972	1,429	-4,727	1,755
5100	30	20	-2,585	1,780	-4,727	2,142
5100	40	38	-2,448	1,717	-4,727	2,279
5100	50	56	-2,391	1,704	-4,727	2,336
6100	10	2	3,761	0,727	-4,727	8,488
6100	20	10	3,297	1,352	-4,727	8,024
6100	30	21	2,918	1,868	-4,727	7,645
6100	40	36	2,701	1,974	-4,727	7,428
6100	50	57	2,721	2,041	-4,727	7,448

Table n.11: horizontal SAR and GNNS data (GNSS from 5th campaign) [author]

Figure 59: building in Cappellazzi district [author]

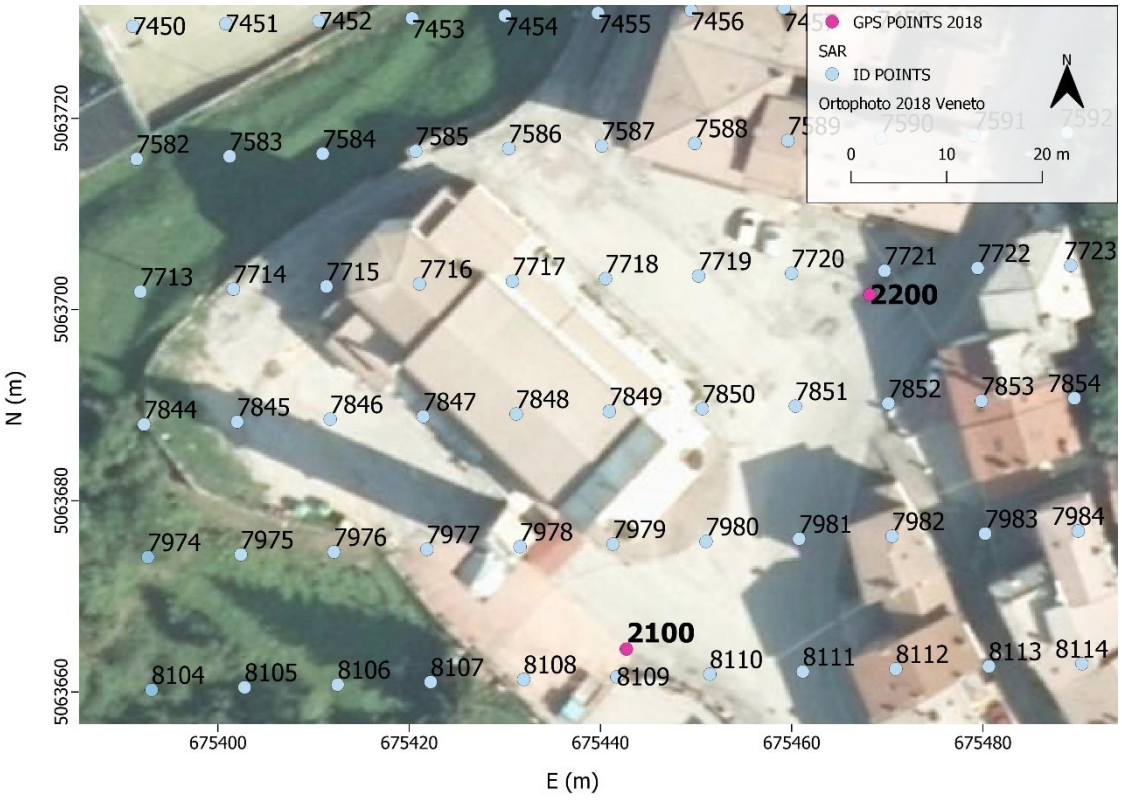

Figure 60: Rovegliana church [author]

In both images are represented the SAR points with their ID, and for each one is associated a vertical and a horizontal velocity.
In figure 59 I chose the points 20646 and 20647 that have the following values:

ID POINT	HORIZONTAL VELOCITY [mm/y]	VERTICAL VELOCITY [mm/y]
20646	-2,11694	-1,33987
20647	-2,09390	-1,57867

Table n.12: horizontal and vertical SAR velocities [author]

In figure 60 I chose the points 7848, 7849, 7716 and 7717. The values are given below.

ID POINT	HORIZONTAL VELOCITY [mm/y]	VERTICAL VELOCITY [mm/y]
7848	-5,4721	-1,7600
7849	-4,6687	-1,4493
7716	-6,3021	-2,7170
7717	-5,5771	-2,1517

Table n.13: horizontal and vertical SAR velocities [author]

A previous case study conducted by Xue Chem et al. [6] and summarized in chapter 3.3 already stated that the two buildings move in block, and I can come to the same conclusion. This is due to the fact that the SAR data have a precision in the order of 1-2 mm, so if the difference among the horizontal (or vertical) velocities, for the same point, is less than 2 mm/y, then the buildings move in the same direction.
In mid-July 2022, I obtained the GNSS data from the new campaign held in June 2022. The total comparisons can be found in the table below.

	JUN/22 - OCT/18 [m]		
ID	N6-N1	E6-E1	H6-H1
1100	-0,026	-0,018	-0,007
1200	-0,008	-0,006	-0,006
2100	-0,019	-0,016	-0,004
2200	-0,015	-0,022	-0,009
3100	-0,013	-0,005	0,003
4100	-0,020	0,008	0,006
5100	-0,013	-0,009	0,006
6100	-0,018	-0,013	0,003

Table n.14: differences in coordinates from October 18 to June 22 [author]

As done above, to obtain the displacement vectors, one must divide these differences by the intervening years, i.e., 3.67 y.

	VELOCITY JUNE22 - OCT18		
ID	N6-N1 [mm/y]	E6-E1[mm/y]	H6-H1 [mm/y]
1100	-7,084	-4,905	-1,907
1200	-2,180	-1,635	-1,635
2100	-5,177	-4,360	-1,090
2200	-4,087	-5,995	-2,452
3100	-3,542	-1,362	0,817
4100	-5,450	2,180	1,635
5100	-3,542	-2,452	1,635
6100	-4,905	-3,542	0,817

Table 15: differences in mm/year from October 2018 to June 2022 [author]

These vectors only represent the velocity considering the first and last displacement (for the same point), without taking into account all the individual displacements that occurred over 3.67 years.
I have therefore calculated the average of the velocities of the 5 total comparisons that occurred over these 6 measurement campaigns (table 16) and compared them with the table above (table 15).

	MEAN OF THE 5 VELOCITIES		
ID	NORTH [mm/y]	EAST [mm/y]	H [mm/y]
1100	-5,535	-4,622	-6,830
1200	-2,905	-2,148	-1,422
2100	-4,329	-6,959	-10,816
2200	-9,121	-11,221	-12,554
3100	-1,987	-2,516	-9,385
4100	-5,237	1,076	-6,977
5100	-2,278	-2,764	2,847
6100	-8,011	-5,377	4,308

Table n.16: mean of the 5 velocities [author]

In some cells the velocities are similar, in others they differ too much. For example, in point 3100, the mean elevation is -9,385 mm/y in table 11 and +0,817 mm/y in table 10. For this reason, I cannot use the velocities of the last campaign, and is more correct to use the mean of all the five velocities.
I then analyzed the velocities referring to JUN19 – OCT18, present in table 17. Here I can see that the values of velocities are very high (especially along Z) because the differences in coordinates, expressed in meters, have to be divided by 0,67 y <1 y and then multiplied by 1000 mm/m, so the values increase.
These velocities then influence too much the means present in table 11, and for this reason I decided to exclude them and I calculated the mean of the velocities considering only the last 4 campaigns, from October 2019 to June 2022 (velocities that are always calculated compared to the first campaign in 2018). The result is shown in table 18.

	JUN/19 - OCT/18					
ID	N2-N1 [m]	E2-E1 [m]	H2-H1 [m]	N VEL. [mm/y]	E VEL. [mm/y]	H VEL [mm/y]
1100	-0,003	-0,005	-0,017	-4,478	-7,463	-25,373
1200	-0,003	-0,002	-0,003	-4,478	-2,985	-4,478
2100	-0,003	-0,007	-0,017	-4,478	-10,448	-25,373
2200	-0,013	-0,013	-0,024	-19,403	-19,403	-35,821
3100	0,003	-0,004	-0,035	4,478	-5,970	-52,239
4100	0,000	0,007	-0,030	0,000	10,448	-44,776
5100	-0,003	0,000	0,003	-4,478	0,000	4,478
6100	-0,012	-0,004	-0,006	-17,910	-5,970	-8,955

Table n.17: values referring to the 2nd and 1st campaign [author]

	MEAN OF THE 4 VELOCITIES		
ID	NORTH [mm/y]	EAST [mm/y]	H [mm/y]
1100	-5,800	-3,912	-2,194
1200	-2,513	-1,939	-0,658
2100	-4,292	-6,088	-7,177
2200	-6,551	-9,183	-6,738
3100	-3,603	-1,652	1,328
4100	-6,547	-1,267	2,472
5100	-1,728	-3,455	2,439
6100	-5,537	-5,228	7,623

Table n.18: mean of the 4 velocities [author]

I therefore used these velocities to create the new vectors (using a plugin already present in Qgis) shown in figure 61.
I can notice that the new vectors (in green) are in line with the old ones (in dark red).
There's no need to check again if the vectors are perpendicular to the contour lines.

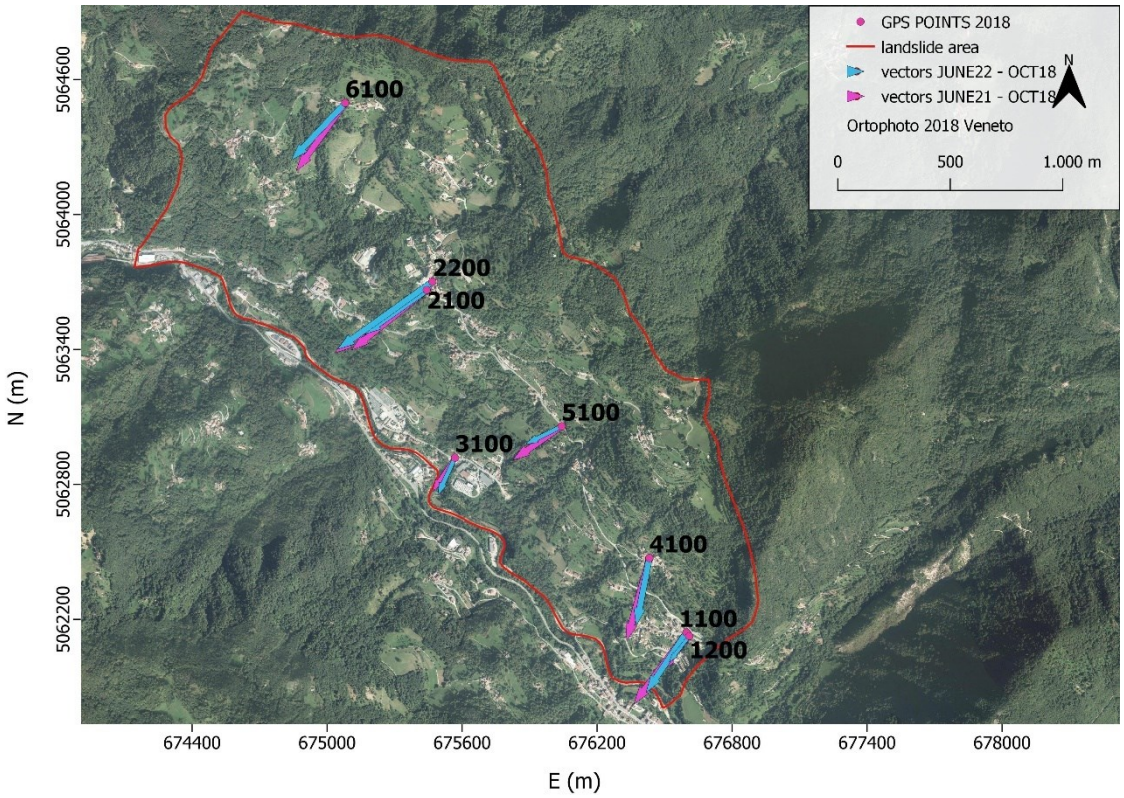

Figure 61: comparison of velocity vectors old and new [author]

One consideration must be made about point 6100, which was moved in this last measurement campaign due to the presence of a tree limiting the visibility of the GNSS signal which, as seen in chapter 2.2, can reduce the precision, especially along the vertical.
The point was moved to the other side of the road and a nail was placed there. A geometric levelling from the middle was done and the elevation of point 6100 was linked with the delta to the elevation of the new position. This connection was not made in planimetry, which is why the east and north values remained the same as last year. From the next campaign, the shift in planimetry will also be made.
The problem with this tree was already present in previous campaigns, and can be seen from the fact that the average of the four velocities along H (see table 18) is +7,263 mm/y, while the value calculated considering June '22 - October '18 is +0,817 (see table 15).
+7,623 mm/y calculated with the GNSS corresponds, over these 3,67 years, to a displacement of +2,798 cm, which is greater than the accuracy of the GNSS in elevation (which is around 1,5 cm). +0,817 mm/y corresponds instead to 0,3 cm in 3,67 years (<1,5 cm) and therefore, although the value is positive, it is within the accuracy of the method.
That said, the value calculated in the last campaign (+0,817) is certainly more correct since, as already mentioned, the landslide cannot move upwards.
The problem of the visibility is another of the limitations of GNSS.
As done previously (in tables 10 and 11), I created two more tables to compare mean velocities of SAR data (which are always the same) with the X and Z coordinates of the new velocity vectors (see table 18).

Table n.19: vertical SAR and GNNS data, comparison between the two [author]

ID POINT	RADIUS [m]	INSIDE POINTS	MEAN SAR VELOCITY [mm/y] (1)	STANDARD DEVIATION	GNSS Z-VELOCITY [mm/y] (2)	DIFFERENCE Between two velocities: 1-2 [mm/y]	DIFFERENCE Between two velocities: 1-2 [mm]
1100	10	2	-1,836	0,06	-2,194	0,358	1,314
1100	20	9	-1,787	0,328	-2,194	0,407	1,494
1100	30	21	-1,834	0,497	-2,194	0,360	1,322
1100	40	37	-1,689	0,622	-2,194	0,505	1,854
1100	50	57	-1,584	0,779	-2,194	0,610	2,238
1200	10	2	-1,25	0,065	-0,658	-0,592	-2,171
1200	20	10	-1,369	0,389	-0,658	-0,711	-2,608
1200	30	22	-1,255	0,566	-0,658	-0,597	-2,190
1200	40	36	-1,255	0,577	-0,658	-0,597	-2,190
1200	50	58	-1,292	0,735	-0,658	-0,634	-2,325
2100	10	2	-1,476	0,001	-7,177	5,701	20,922
2100	20	9	-1,553	0,151	-7,177	5,624	20,639
2100	30	19	-1,726	0,361	-7,177	5,451	20,005
2100	40	36	-2,002	0,623	-7,177	5,175	18,992
2100	50	58	-2,256	0,783	-7,177	4,921	18,060
2200	10	2	-2,065	0,134	-6,738	4,673	17,148
2200	20	9	-2,117	0,322	-6,738	4,621	16,957
2200	30	19	-2,152	0,493	-6,738	4,586	16,829
2200	40	35	-2,326	0,696	-6,738	4,412	16,190
2200	50	58	-2,578	0,849	-6,738	4,160	15,265
3100	10	2	-2,879	0,443	1,328	-4,207	-15,441
3100	20	9	-2,706	0,776	1,328	-4,034	-14,806
3100	30	20	-2,687	0,929	1,328	-4,015	-14,736
3100	40	38	-2,758	0,95	1,328	-4,086	-14,997
3100	50	57	-2,764	0,979	1,328	-4,092	-15,019
4100	10	3	-0,386	0,495	2,472	-2,858	-10,490
4100	20	8	-0,732	0,653	2,472	-3,204	-11,760
4100	30	21	-1,024	1,237	2,472	-3,496	-12,831
4100	40	37	-1,315	1,479	2,472	-3,787	-13,899
4100	50	55	-1,486	1,593	2,472	-3,958	-14,527
5100	10	2	-5,184	0,23	2,439	-7,623	-27,977
5100	20	8	-5,718	0,634	2,439	-8,157	-29,936
5100	30	20	-6,013	0,763	2,439	-8,452	-31,019
5100	40	38	-6,522	1,002	2,439	-8,961	-32,734
5100	50	56	-6,998	1,515	2,439	-9,437	-34,634
6100	10	2	-5,591	0,124	7,623	-13,214	-48,497
6100	20	10	-5,113	1,241	7,623	-12,736	-46,742
6100	30	21	-4,770	1,498	7,623	-12,393	-45,484
6100	40	36	-5,395	2,507	7,623	-13,018	-47,777
6100	50	57	-6,303	3,746	7,623	-13,926	-51,110

Table n.20: horizontal SAR and GNNS data, comparison between the two [author]

ID POINT	RADIUS [m]	INSIDE POINTS	MEAN SAR VELOCITY [mm/y]	STANDARD DEVIATION	GNSS X-VELOCITY [mm/y]	DIFFERENCE between two velocities [mm/y]	DIFFERENCE between two velocities [mm]
1100	10	2	-2,004	0,038	-3,912	1,908	7,002
1100	20	9	-1,990	0,170	-3,912	1,922	7,053
1100	30	21	-1,993	0,271	-3,912	1,919	7,042
1100	40	37	-2,011	0,336	-3,912	1,901	6,976
1100	50	57	-2,016	0,379	-3,912	1,896	6,958
1200	10	2	-1,716	0,102	-1,939	0,223	0,818
1200	20	10	-1,657	0,310	-1,939	0,282	1,035
1200	30	22	-1,692	0,353	-1,939	0,247	0,907
1200	40	36	-1,745	0,420	-1,939	0,194	0,712
1200	50	58	-1,817	0,497	-1,939	0,122	0,448
2100	10	2	-4,232	0,104	-6,088	1,856	6,809
2100	20	9	-4,416	0,436	-6,088	1,672	6,134
2100	30	19	-4,629	0,744	-6,088	1,459	5,352
2100	40	36	-4,703	1,060	-6,088	1,385	5,081
2100	50	58	-4,670	1,258	-6,088	1,418	5,202
2200	10	2	-3,949	0,121	-9,183	5,234	19,209
2200	20	9	-3,931	0,311	-9,183	5,252	19,275
2200	30	19	-3,898	0,448	-9,183	5,285	19,396
2200	40	35	-4,056	0,700	-9,183	5,127	18,816
2200	50	58	-4,221	1,071	-9,183	4,962	18,210
3100	10	2	-2,558	0,148	-1,652	-0,906	-3,323
3100	20	9	-2,282	0,497	-1,652	-0,630	-2,310
3100	30	20	-1,995	0,648	-1,652	-0,343	-1,257
3100	40	38	-1,784	0,799	-1,652	-0,132	-0,482
3100	50	57	-1,675	0,872	-1,652	-0,023	-0,082
4100	10	3	0,741	0,303	-1,267	2,008	7,3687
4100	20	8	0,874	0,288	-1,267	2,141	7,8568
4100	30	21	0,909	0,587	-1,267	2,176	7,9853
4100	40	37	0,992	0,727	-1,267	2,259	8,2899
4100	50	55	0,961	0,734	-1,267	2,228	8,1761
5100	10	2	-2,371	0,508	-3,455	1,084	3,9794
5100	20	8	-2,972	1,429	-3,455	0,483	1,7737
5100	30	20	-2,585	1,780	-3,455	0,870	3,1940
5100	40	38	-2,448	1,717	-3,455	1,007	3,6968
5100	50	56	-2,391	1,704	-3,455	1,064	3,9060
6100	10	2	3,761	0,727	-5,228	8,989	32,988
6100	20	10	3,297	1,352	-5,228	8,525	31,285
6100	30	21	2,918	1,868	-5,228	8,146	29,895
6100	40	36	2,701	1,974	-5,228	7,929	29,098
6100	50	57	2,721	2,041	-5,228	7,949	29,172

5 DISCUSSION

In this chapter I am going to discuss the results obtained with Qgis, highlighting the problems related to GNSS and SAR methodology.

5.1 DISCUSSION ON SAR DATA

I want to check whether areas that have the same type of landslide (such as translational landslides), i.e. areas with the same colour (see fig. 46), have similar average velocities or not.

From the table 9 I notice that there is no pattern.

For example, area 1 has a vertical (horizontal) velocity of -1,183 mm/y (0,052 mm/y), area 5 has an average velocity of -9,478 mm/y (0,383 mm/y), and area 8 has -13,225 mm/y (5,413 mm/y). The same can be verified with the other areas.

I can therefore conclude that areas characterised by the same type of landslide do not show similar velocities.

One thing that I can see, however, from the table 9, is that neighboring areas have similar velocities. Areas 1, 2 and 3 in fact have small vertical and horizontal velocities, from -1,183 to -4,861 mm/y along Z, and from -0,307 to 0,633 mm/y along X. In contrast, areas 5, 6, 7 and 9 have large vertical velocities, ranging from -7,772 to -9,693 mm/y.

Area 8 has the largest values of all, of -13,225 mm/y vertically and 5,413 mm/y horizontally.

Another thing I can see is that all the vectors in the GNSS points point to the left, so the displacement is from east to west, but the average horizontal movement of the SAR points on the polygons are not all negative. For example, polygons 1, 3, 4, 5, 8 and 10 have positive average velocities, so the displacement is from west to east.

It is therefore necessary to check how the contour lines are positioned at these polygons to see if the landslide in those areas is actually moving eastwards or if there is an error in the SAR data.

In figure 62 for polygon 4, we can clearly see from the contour lines that the landslide is moving westwards. The SAR point average is + 4,232 mm/y. We can therefore conclude that the error lies in the SAR, and the reason for this is that there is a large area of trees in that zone, which, as already mentioned, creates reflectivity problems.

The same observation can be made for polygon 8, where the horizontal average is + 5,413 mm/y. In figure 63 it is possible to see the wooded area.

For polygon 10, in figure 64 it can be seen that in the upper part of the polygon, the contour lines lead the landslide to move eastwards, while in the lower part, the contour lines go in the opposite direction. An average velocity of + 1,541 mm/y could therefore be realistic. However, if we look at the SAR points, we notice first of all that they do not cover the entire area, that they have both positive and negative values, and above all that they have positive values in the lower part of the polygon, where, however, the contour lines indicate the opposite direction. It's also true that the contour lines may not be correct, due to the fact that they are constructed starting from DSM, that takes into account the top of the trees and not the soil below.

In any case, the average velocity is less than 2 mm/y.

As for polygons 1, 3 and 5 I can neglect this analysis since the average values are positive, but borderline, and are 0,052 mm/y, 0,633 mm/y and 0,383 mm/y respectively.

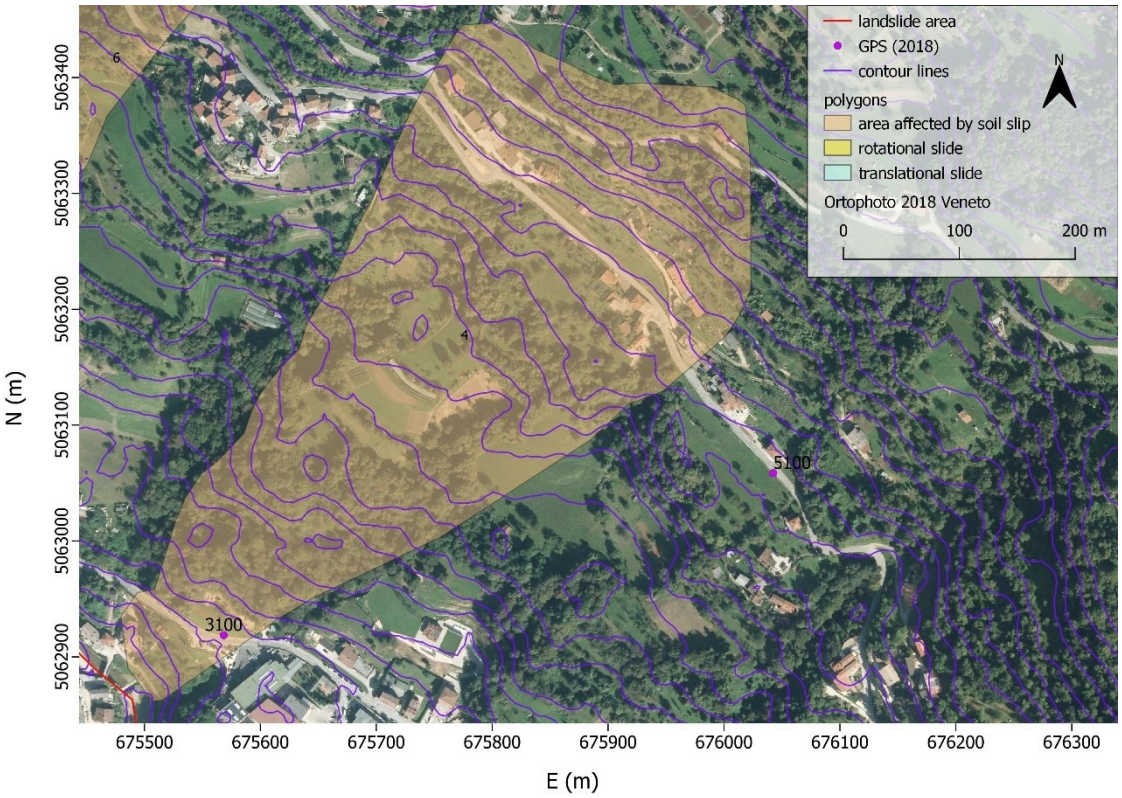

Figure 62: Polygon area n. 4 [author]

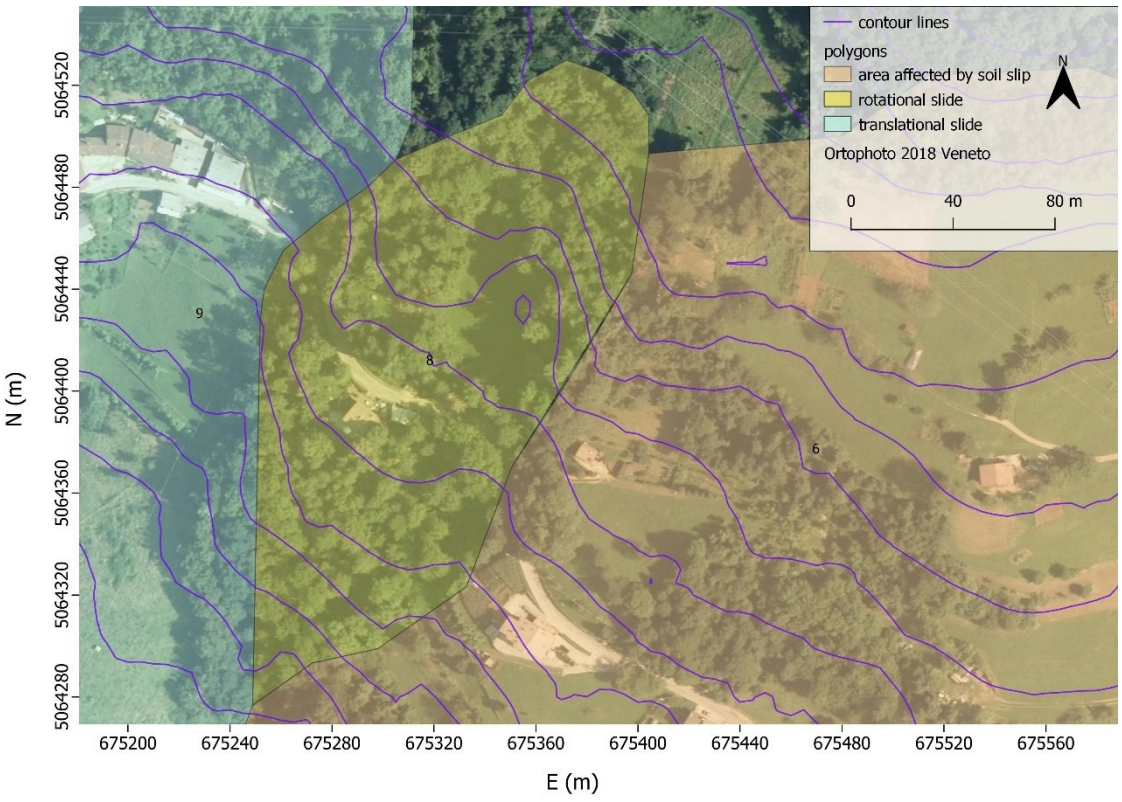

Figure 63: Polygon area n.8 [author]

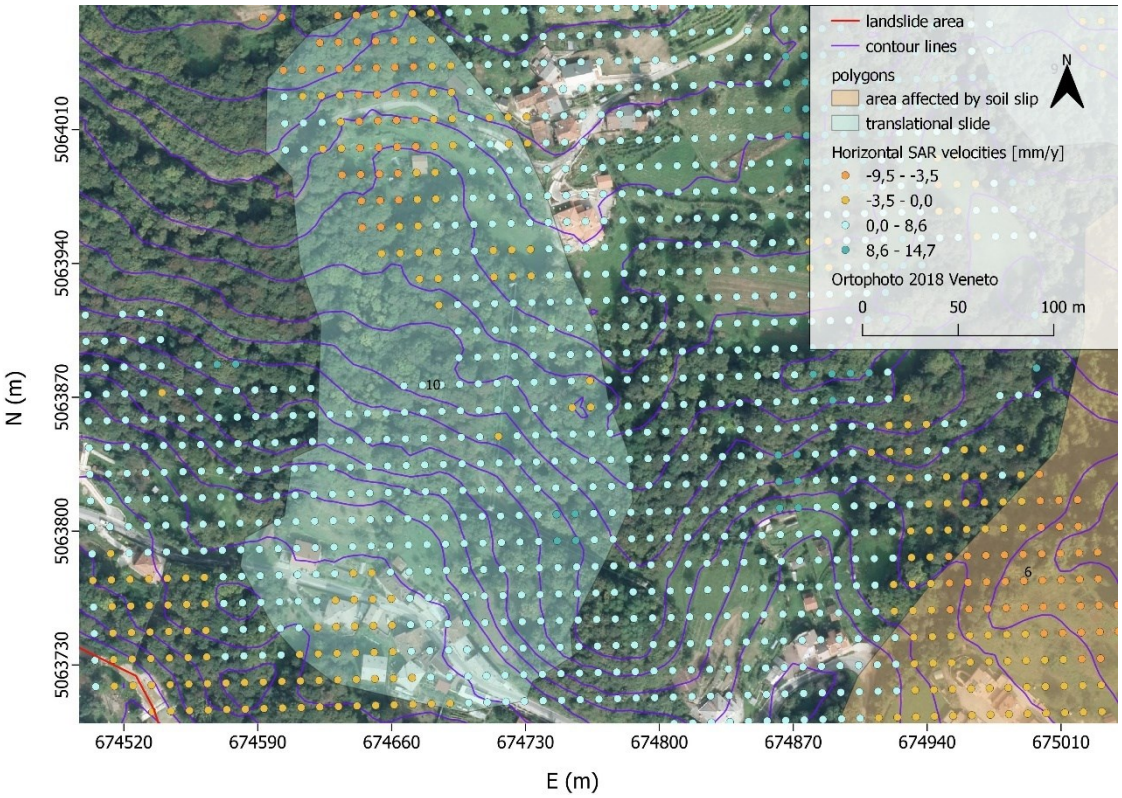

Figure 64: Polygon area n.10 [author]

To correctly describe a variable, it is not sufficient to use a statistical average such as the arithmetic mean or median. These indices, although very important for summarizing data, provide only a partial view of the variable you are analysing. For this reason, it is always important to combine the indices of position with an index of variability, such as the standard deviation. The standard deviation of a variable is a summary index of the differences of the values of each observation from the mean of the variable, and it gives us an idea of the error.

Each observation has a deviation from the mean. This deviation is 0 if the observation has exactly the same value as the mean.

In our case, is important that the SAR velocities are greater that the precision of the method, otherwise we cannot know if the displacement really occurred.

Therefore, we have to check if the modulus of the velocities is greater than the standard deviation.

In tables 10 and 11 we see that all the vertical and horizontal velocities are bigger that the deviation, except for some vertical values of point 4100, where the situation is borderline.

We can see in figure 65 that vertical SAR velocities around that point have both negative and positive values, but since the modulus of the velocities of those points are less than 2 mm/y (so less than the precision of the SAR), this means that actually the point 4100 and the surrounding area is not moving vertically (or at least the displacement is very small, not detectable with the SAR). That's why for point 4100 the vertical velocity and the standard deviation are of the same order.

Figure 65: vertical SAR points around point 4100 [author]

5.2 DISCUSSION ON GNSS DATA AND COMPARISON GNSS-SAR DATA

In chapter 3.1 the GNSS satellite analysis is carried out, which allowed the identification of the most unstable zones in the analysed area, where it was found that the regions with the greatest acceleration are located in the Piazza and Sigismondi districts. In particular, it can be seen that point 2200 (located in Contrada Piazza) is the one with the maximum planimetric deformation vector from 2018 to 2020, amounting to 2,2 cm, followed by 2100 with 1,6 cm. The same intensity is found at point 6100 (at Sigismondi).

With the 2021 data, I can always see that point 2200 is the one with the greatest displacement, amounting to 3,2 cm, followed by point 2100. This time, it is succeeded by 1100, 4100 and then 6100 (see table 21).

Point 2200 has therefore moved from 2,2 cm to 3,2 cm from October 2020 to June 2021. As can be seen from the table below, its vector has a velocity of 11,7 mm/y.

Analysing the new data for 2022, we can see in table 23 that 1100 is the point with maximum displacement, equal to 3,16 cm, followed by point 2200 with 2,66 cm, and then 2100, 6100 and 4100.

JUN ‘21 - OCT ‘18	
ID	DISPLACEMENT VECTOR [m]
1100	0,024
1200	0,011
2100	0,026
2200	0,032
3100	0,011
4100	0,023
5100	0,016
6100	0,022

Table n.21: displacement vector in meters, JUN21-OCT18 [author]

	VELOCITY JUN/21 - OCT/18 [mm/year]			
ID	N5-N1	E5-E1	H5-H1	2-D VECTOR
1100	-6,909	-5,091	-4,727	8,582
1200	-3,273	-2,545	-1,455	4,146
2100	-5,818	-7,273	-5,455	9,313
2200	-6,909	-9,455	-1,455	11,710
3100	-3,273	-2,182	2,909	3,933
4100	-8,000	-2,182	-3,636	8,292
5100	-3,273	-4,727	2,545	5,749
6100	-6,545	-4,727	2,182	8,073

Table n.22: velocities and displacement vector in mm/y [author]

JUN ‘22 - OCT ‘18	
ID	2-D VECTOR [m]
1100	0,0316
1200	0,0100
2100	0,0248
2200	0,0266
3100	0,0139
4100	0,0215
5100	0,0158
6100	0,0222

Table n.23: displacement vector in meters, JUN22-OCT18 [author]

The reason why I created the circles of various radius and cut out the SAR points within them is to check how accurate the GNSS points are compared to the SAR. The latter is in fact precise to about 2 mm while the GNSS has maximum precision in the order of a centimetre in planimetry and a centimetre and a half in elevation.
With regard to the vertical data, I see from table 19 that GNSS points 3100, 4100, 5100 and 6100 have positive values, i.e. upwards vertical displacement. The SAR data, on the other hand, which is much more accurate than GNSS, is negative.

I can also see that SAR velocities around the same point are more or less the same whether it takes a 10m or 50m radius, so areas of land close together (in this case <50m) have 'equal' velocities.
It is important to point out that points 3100, 4100 and 5100 have positive altitude, but with a value less than 15mm / 3,67 y i.e., less than 4mm/y, which is within the precision of the method and is therefore not considered true displacement, so we do not have a problem with this.
Point 6100, on the other hand, has a displacement along Z of + 7,623mm/y > 4mm/y: this error, however, has already been explained above and is due to the poor visibility of the satellites caused by the presence of a tree (in fact, I recall that these values were found by averaging the velocities of previous campaigns).
Checking table 14, which only contains data for 2022 where point 6100 was moved, the delta H value is +3mm, so even if positive, it is acceptable (<10 mm).
Looking at the SAR, the points that are shifted (i.e. those with a value greater than the method's precision, in this case 2 mm/y) are 3100, 5100 and 6100; 2200 is borderline.
According to the GNSS, on the other hand, the ones that move are the 2100 and 2200, with a value greater than 4 mm/y.
What are these discrepancies due to? There are several reasons.
One reason may be due to the fact that the SAR and GNSS data are in any case taken at different times, although we have considered a linear deformation there is still this aspect to be taken into account. Then another thing to remember is that the points are in highly vegetated areas and SAR has difficulty in these areas, so the accuracy may not be 2 mm/y but a little more. Or else the error lies in the GNSS, as was the case with the 6100 or as was the case with the point 5100, which should be kept under observation because it always gave positive values along the vertical during the last measurement campaigns.
I will now look at the horizontal values in table 20. I see that all the GNSS values are negative, so in the correct direction (given to us by the contour lines). For the SAR data, on the other hand, the values are positive for 6100 and 4100. The latter point, however, has a value of about 0.8 mm/y < 2 mm/y, while point 6100 > 2 mm/y. There is therefore an error here due to the technological limit of this method. To understand better, I look at figure 66.
Then I note that, according to SAR, points 2100, 2200, 3100 and 5100 move because they have a value > 2 mm/y; point 1100 is borderline.
According to GNSS, the points that move, i.e., have |x-velocity| > 2,72 mm/y (10 mm/3,67y) are 1100, 2100, 2200, 5100 and 6100. SAR and GNSS therefore agree with the exception of 6100, where the GNSS data comes to the aid of SAR, since the SAR data was wrong (as mentioned earlier).
In order to be able to make a comparison between GNSS and SAR data and to understand whether the two methods are congruent with each other and can be used together, it is important that the difference between the velocities, measured in these 3.67 years, with these two methods is less than the accuracy of the two methods.
It is good to remember that SAR has accuracy in velocities and GNSS has accuracy in positioning. One measures from satellites and the other from the ground. I am therefore making comparisons between two different things! The comparison can be made by reasoning in mm or in mm/y.

In the first case the accuracy is equal to about 10-15 mm for the GNSS + 2 mm/y*3,67 y for the SAR, which equals 17,34- 22,34 mm.
In the second case instead, I add 2 mm/y with (10-15 mm)/3,67 y and get 4,72-6,08 mm/y. Clearly these values have not to be considered in a very precise way.
In table 19, last column, all values are in modulus < 22,34 mm with the exception of points 5100 and 6100. For the latter point, the reason is the same as that mentioned above (i.e. the tree). For point 5100, the reason is that SAR has a negative value and GNSS a positive value, so the difference is even greater. Looking at table 24, I see that along Z the difference from 2018 is less than the accuracy of the method, so this is not a problem.
However, it is also good to keep an eye on this point in future measurements to see if the point continues to have positive elevation and very different from the SAR data.

ID	Difference along Z [mm]
1100	-8,052
1200	-2,416
2100	-26,339
2200	-24,727
3100	4,875
4100	9,074
5100	8,952
6100	27,978

Table n.24: difference along Z in mm related to the mean of the 4 measurements [author]

Looking at table 20, last column, I see that all the values are < 17,34 mm except for point 2200 and 6100.
For point 6100, we said earlier that there was an error in the SAR because it gave me a positive value greater than the accuracy of the method.
For point 2200, I can actually consider the situation borderline: if I consider that the GNSS has an error between 10 and 15 mm, then I have to consider values between 17,34 and 22,34 mm.

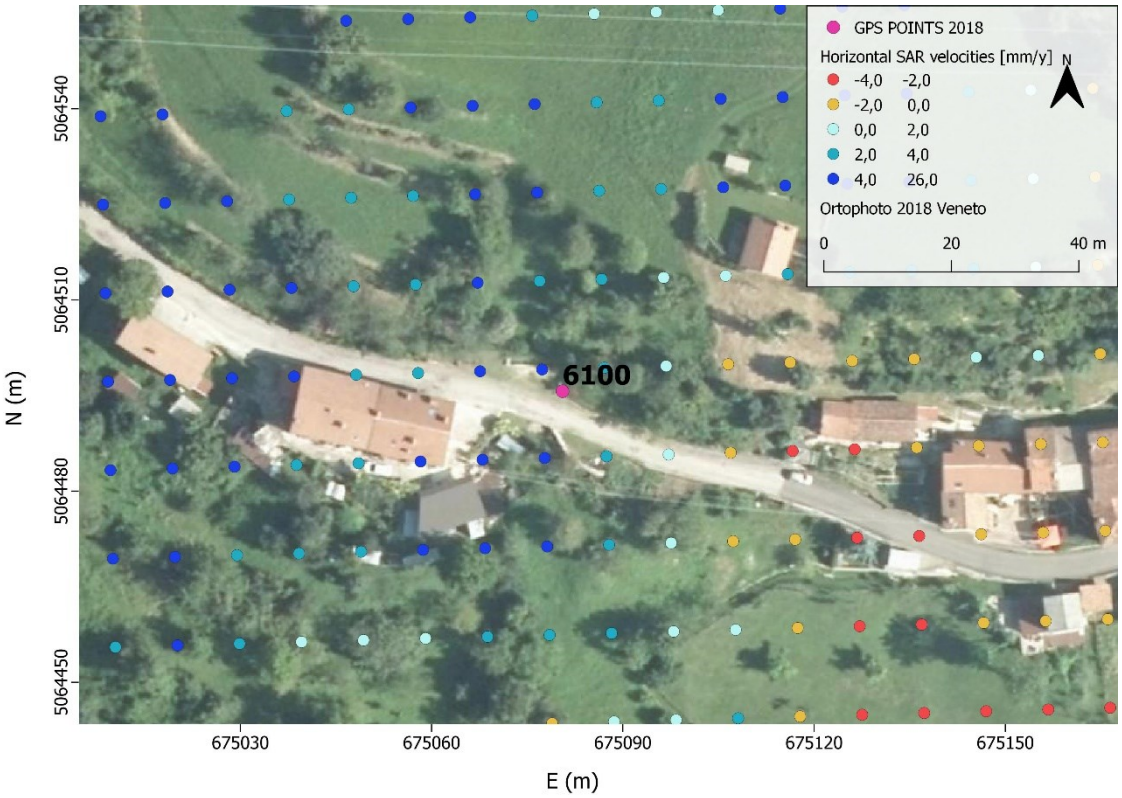

Figure 66: Horizontal SAR velocities around point 6100 [author]

6 CONCLUSION

The analyses carried out on the behaviour of the Rovegliana slope by means of GNSS satellite analysis and SAR technique made it possible to locate the most unstable zones in the area analysed. It was possible to identify the areas characterised by stable deformation dynamics over time and those that have undergone acceleration. In particular, in the past years it emerged, with the use of GNSS, that the areas that underwent the greatest acceleration were those located in the northern portion of the slope, in contrada Piazza (where points 2100 and 2200 are located) and Sigismondi (where there's point 6100). But with the data of 2021 and 2022, it came out that also point 1100 (contrada Cappellazzi) has a significant movement, with a displacement of 3,16 cm in 3,67 years.

In general, deformations were observed in all the sampled points of the GNSS network inside the landslide perimeter, with displacements of the order of some millimeters: from -4,65 mm to -33,70 mm in planimetry along East, and from -2,42 mm to -26,33 mm along the vertical (considering 3,67 years).

In conclusion, it is possible to state that the Rovegliana area is affected by widespread instability in the entire domain.

One of the first thing that I did was to extract the different landslide areas (fig. 46) in order to check whether the areas characterized by the same type of movements have similar velocities or not, and I came to the conclusion that areas denoted by the same type of landslide do not show similar velocities, but neighboring areas do. In particular areas in the upper part of the landslide move more than those in the lower part.

Using the SAR data, I also established that areas close to the GNSS points move with the same velocities.

I also saw that the mean values of the horizontal SAR data inside the polygons are not representative of the real direction of the movement of the landslide, that is given by the contour lines: this is due to the fact that Rovegliana area is mainly vegetated. This condition is not very favorable for the SAR and the GNSS either (e.g., the trees limit the visibility of the satellites, like for point 6100).

Comparing SAR and GNSS data is very useful because it helps us to understand both if the two methodologies can be used together, but also to better understand how individual points move.

For example, in some points, like 6100, the error was due to the GNSS (visibility problem), while the SAR showed adequate values, so in this case I can get the information from the SAR. Or for some points, especially due to the presence of trees and grass, the SAR is not adequate and so in this case the GNSS could help us.

One problem with SAR is that it does not give us information along the North-South direction, so I have to use GNSS.

Another consideration is that SAR is more accurate than GNSS, so SAR can help in some situations such as with points 3100, 4100 and 5100 which turn out to be positive with GNSS and negative with SAR: I rely on SAR which is more accurate as the landslide cannot move upwards.

In my work, since the differences between the velocities measured in these 3.67 years with these two methods are smaller than the accuracy of the two methods (~22 mm), then GNSS and SAR are congruent with each other.

In spite of this, it is still worth remembering that the two datasets were taken at different times and that the accuracy of the methods is approximate: SAR has an accuracy of 2 mm/y if I consider points with good reflectivity, but I do not know its accuracy in vegetated areas.
However, I believe that the combined use of the two methods is very effective.
In the next campaigns, a connection in planimetry will be made between the point 6100 and the nail positioned in the opposite side of the road.
As already said, another point to be kept under observation is 5100, to see if it gives again positive values along the vertical.

7 BIBLIOGRAPHY AND SITOGRAPHY

[1] Laboratorio di Rilevamento e Geomatica, *Studio generale delle condizioni geostatiche dell'abitato di Rovegliana in comune di Recoaro Terme (VI*), 2015.

[2] Thomas Baschiera, *Geomatic methodologies for deformations analysis: application to the Rovegliana landslide (Recoaro Terme, Vicenza), 2020.*

[3] Andrea Zanibellato, *Identificazione e caratterizzazione dei fenomeni franosi nell'area di Rovegliana (Recoaro Terme, VI), 2012.*

[4] M. Fabris, V. Achilli, X. Chen, M. Floris, A. Menin, M. Monego, G. Tessari, *Monitoraggio di edifici in aree instabili: utilizzo di dati terrestri e satellitari applicati al versante franoso di Rovegliana (Recoaro Terme, Vicenza), 2021.*

[5] M. Toaldo, M. Monego, G. Tessari, A. Menin, M. Fabris, V. Achilli, M. Floris, *Studio preliminare sulle condizioni predisponenti le dinamiche di versante nell'area di Rovegliana (Prealpi Venete – Italia nord-orientale)*, 2016.

[6] X. Chen, V. Achilli, M. Fabris, A. Menin, M. Monego, G. Tessari, M. Floris, *Combining Sentinel-1 Interferometry and Ground-Based Geomatics Techniques for Monitoring Buildings Affected by Mass Movements*. Remote sensing 2021, 13, 452.

[7] Massimo Fabris, *slides of the course LAND SURVEYING AND GEOGRAPHICAL INFORMATION SYSTEM (GIS),* 2020-2021.

[8] https://pro.arcgis.com/en/pro-app/latest/help/data/imagery/overview-of-georeferencing.htm [Consulted online May]

[9]https://mapasyst.extension.org/what-is-an-orthophoto/ [Consulted online May]

[10]https://en.wikipedia.org/wiki/QGIS 11.5 [Consulted online May]

[11]https://engineering.purdue.edu/~abe325/contours.html [Consulted online May]

[12]https://mapasyst.extension.org/what-is-an-orthophoto/ [Consulted online June]

[13]https://en.wikipedia.org/wiki/Structure_from_motion-cite_note-1 [Consulted online June]

[14]https://blog.bliley.com/the-differences-between-the-5-gnss-satellite-network constellations [Consulted online July]

[15] https://www.isprambiente.gov.it/it/pubblicazioni/rapporti/Rapporto-sulle-frane-in-Italia [Consulted online August)

[16] https://www.researchgate.net/figure/Structure-from-Motion_fig1_234044400 [Consulted online August]